University of Cincinnati

Date: 11/3/2011

I, Nicholas M Bedford , hereby submit this original work as part of the requirements for the degree of Doctor of Philosophy in Materials Science.

It is entitled:

Electrospun Fibers for Energy, Electronic, & Environmental Applications

Student's name: **Nicholas M Bedford**

This work and its defense approved by:

Committee chair: Donglu Shi, PhD

1975

Electrospun Fibers for Energy, Electronic, & Environmental Applications

A Dissertation Submitted To

The Division of Research and Advanced Studies

UNIVERSTIY OF CINCINNATI

In partial fulfillment of the Requirements for the degree of

DOCTOR OF PHILOSOPHY

In the Materials Science and Engineering Program, School of Energy, Environmental, Biological
and Medical Engineering of the College of Engineering and Applied Science

By

Nicholas M. Bedford

Committee Chairs: Dr. Donglu Shi and Dr. Andrew Steckl

November 3rd, 2011

Members of the Dissertation Committee

Dr. Donglu Shi (Co-Chair)
Materials Science and Engineering Program
School of Energy, Environmental, Biological and Medical Engineering
University of Cincinnati
Dr. Andrew J. Steckl (Co-Chair)
Electrical Engineering Program
School of Electronic and Computing Systems
University of Cincinnati
Dr. Rajesh R. Naik
Biological and Nanostructured Materials Branch
Materials and Manufacturing Directorate
Air Force Research Laboratory
Dr. F. James Boerio
Materials Science and Engineering Program
School of Engineering Education
University of Cincinnati
Dr. Gregory Beaucage
Materials Science and Engineering Program
School of Energy, Environmental, Biological and Medical Engineering
University of Cincinnati

Abstract

Electrospinning is an established method for creating polymer and bio-polymer fibers of dimensions ranging from ~10 nanometers to microns. The process typically involves applying a high voltage between a solution source (usually at the end of a capillary or syringe) and a substrate on which the nanofibers are deposited. The high electric field distorts the shape of the liquid droplet, creating a Taylor cone. Additional applied voltage ejects a liquid jet of the polymer solution in the Taylor cone toward the counter electrode. The formation of fibers is generated by the rapid electrostatic elongation and solvent evaporation of this viscoelastic jet, which typically generates an entangled non-woven mesh of fibers with a high surface area to volume ratio. Electrospinning is an attractive alternative to other processes for creating nano-scale fibers and high surface area to volume ratio surfaces due to its low start up cost, overall simplicity, wide range of processable materials, and the ability to generate a moderate amount of fibers in one step. It has also been demonstrated that coaxial electrospinning is possible, wherein the nanofiber has two distinct phases, one being the core and another being the sheath. This method is advantageous because properties of two materials can be combined into one fiber, while maintaining two distinct material phases. Materials that are inherently electrospinable could be made into fibers using this technique as well. The most common applications areas for electrospun fibers are in filtration and biomedical areas, with a comparatively small amount of work done in energy, environmental, and sensor applications. Furthermore, the use of biologically materials in electrospun fibers is an avenue of research that needs more exploration, given the unique properties these materials can exhibit.

The research aim of this thesis is to explore the use of electrospun fibers for energy, electrical and environmental applications. For energy applications, fibers consisting of the commonly used organic photovoltaic electron donor/acceptor pair P3HT:PCBM were made by coaxial electrospinning. The inclusion of P3HT:PCBM fibers into an active layer of a organic photovoltaic device led to a ~ 50% increase in power conversion efficiency over a thin film device of identical chemical composition and thickness. The inclusion of biological photosynthetic moieties into electrically relevant conjugated polymers was also explored for electrical applications. Polymeric fibers consisting largely of PEDOT:PSS were doped with thylakoid vesicles from spinach, and were found to act as photo-detectors. Native PEDOT:PSS does not exhibit such properties. For environmental applications, photocatalytic degradation membranes were also created by electrospinning cellulosic fibers which could be used as platforms to efficiently bind the photocatalyst TiO_2. Employing different fiber-titania binding strategies, titania nanoparticles of various sizes and band gap configurations were successfully incorporated into mats of non-woven cellulosic nanofibers. These mats were found to successfully degrade dyes and relevant fresh water toxins such as microcystin-LR.

CONTENTS

List of Figures

List of Tables

Chapter 1: Introduction to Electrospinning

Increasing amounts of research efforts have been focused on the creation of one-dimensional (1-D) micro/nanostructured materials for their advantageous use in various applications.[1,2,3,4,5,6] Asymmetric materials in this size domain exhibit preferential and/or enhanced properties when compared to parent bulk material. While many methods exist to create 1-D micro/nanostructures,[7,8,9,10,11,12,13] electrospinning, an electrostatic fluidic extraction method to create 1-D structures from a solution or melt phase, is becoming increasing popular. This is due to its overall simplicity, low start-up cost, wide variety of processable materials, relative ease to produce an appreciable amount of material, and the ability to form non-woven highly porous mats or meshes with an increased surface area to volume ratio (SVR). The process involves the ejection of a charged liquid jet from a biased droplet of solution. This liquid jet becomes unstable, causing it to whip and elongate in a semi-chaotic nature, while subsequent solvent evaporation creates the electrospun fibers. Since electrospinning can be a continuous process akin to many fiber drawing or spinning techniques, fibers of extremely long length can be produced. The main difference between electrospinning and other fiber drawing or spinning methods is the electrostatic contactless scheme employed generated by the large electric field, which allows for the spinning of fibers with smaller diameters.[14] The combination of all the aforementioned factors has led to the use of electrospun fibers in a wide spectrum of applications.

1.1 Historical Context

Electrospinning can be considered an extension of the well-established electrohydrofluidic method for creating micro/nanoparticles known as electrospraying. Particles are formed instead of fibers largely due to a material's inability to form entanglements in solution, which can normally be associated with a low solution viscosity. In 1934, the first patent describing the electrospinning process was filed by Formhals.[15] It was not until 1971 that a report on an electrostatic based method to make acrylic fibers (then called "electrostatic spinning") was first published in the literature by Baumgarten.[16] A decade later Larrondo and St. John Manley published a series of reports on the electrostatic spinning of polymer melts.[17,18,19] In the mid-nineties Professor Reneker's group first coined the term electrospinning to describe this electrostatic fiber forming process for a large array of polymer solutions.[20,21,22,23] These papers would serve as a catalyst for an explosion of electrospinning research seen in the scholarly and patent literature (Figure 1.1).

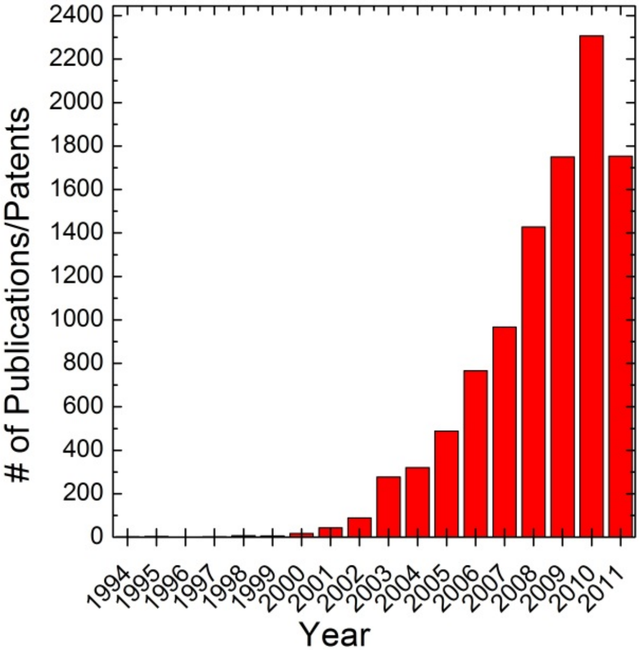

Figure 1.1. Number of publications and patents per year as determined using SciFinder Scholar. Data taken on 10/02/2011.

1.2 How Does Electrospinning Work?

A schematic of a conventional electrospinning apparatus is shown in Figure 1.2.[14] The apparatus consists of a high-voltage power supply, a spinneret, and a collector. The bias is applied between the spinneret and collector and is typically between 1-30 kV. The solution is fed to the spinneret (commonly a metal needle) by a syringe pump at a controlled flow rate. Once a droplet is formed at the end of the spinneret and a high voltage is applied, the droplet becomes highly electrified. This droplet converts to a conical shape (known as a Taylor cone) due to electrostatic repulsion of charges in the solution and the Coulombic force from the external electric field. At sufficient applied field strength, the electrostatic force overcomes the surface tension in the polymer solution and causes a liquid jet to emerge from the droplet. The liquid jet undergoes a stretching and whipping process while solvent evaporates, leading to a decrease in jet diameter (from millimeters down to the micron & nanometer range). After the solvent evaporates fibers are formed and collected in a random orientation by the oppositely biased collector. As shown in Figure 1.2, the fibers are deposited on the collector in a vertical manner but the setup is not limited to this orientation. Horizontal set-ups are commonly used to prevent solvent droplets from damaging the previously deposited electrospun fibers. Various processing parameters affect the overall morphology of the electrospun fibers and are discussed in the following section.

Three main forces are present during the electrospinning process. After a liquid jet emerges from the Taylor cone, the surface tension in the liquid is a driving force to reduce surface area and thus droplet formation would normally be preferred. Due to the application of an electric field, these liquid jets are highly charged, and therefore experience an electrostatic repulsion force along the surface of the liquid jet. The electrostatic repulsion is the driving force for maintaining the elongated jet morphology which further increases the surface area. Solutions for electrospinning are typically dissolved polymers and, as such, exhibit viscoelastic properties that resist rapid changes in shape. If the electrostatic and viscoelastic forces overcome the surface tension in the liquid jet then fiber formation occurs as opposed to droplet formation. To induced fiber formation certain modifications to the electrospinning solution can be made, such as surfactant addition (decreased surface tension) and salt addition (increased number of charges). Fiber morphology is dependent on are large set of interconnected solution properties a processing variables, which will be discussed in the next section.

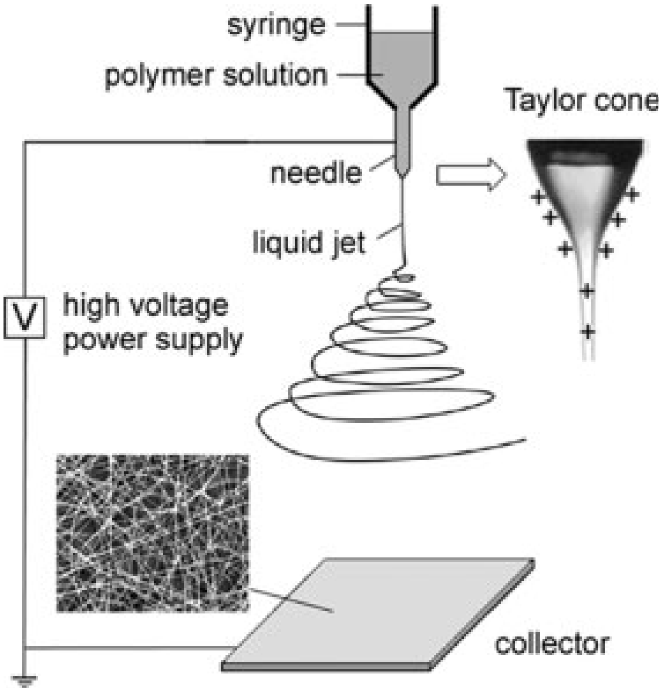

Figure 1.2. Schematic of a basic electrospinning set-up. Reproduced with permission[14]. Copyright Wiley-VCH, 2004.

1.2.1 Processing Parameters

The overall morphology of electrospun fibers depends on three general classes of parameters: processing variables (such as electric field strength, spinneret to substrate distance, and solution flow rate), polymer/solvent variables (such as concentration, which also affects solution viscosity), polymer molecular weight, electrical conductivity of the solution, solvent volatility, and surface tension), and environmental variables (such as temperature and humidity). The first two classes of parameters have the largest effect on fiber morphology, unless solution properties are significantly altered by temperature and/or the polymeric material strongly interacts with ambient moisture. The following sections will provide a brief overview on each parameter type and how it affects the morphology of electrospun fibers. Changes in temperature will be excluded from this discussion as electrospinning is rarely performed above or below room temperature.

1.2.1.1 Polymer Concentration, Molecular Weight, and Solution Viscosity

The most important parameters in obtaining electrospun fibers (vs. electrosprayed droplets or beads) are the polymer concentration and polymer molecular weight because fiber formation requires the presence of polymer chain entanglements in solution. At a set molecular weight, an increase in concentration will yield an increase in the number entanglements per polymer chain. Alternatively, if the polymer concentration is held constant an increase in the polymer molecular weight would give rise to an increase in chain entanglements due to the decreasing concentration of solvent. The decrease or increase in polymer chain entanglements can be determined by viscosity measurements. While chain entanglements have long been recognized as vital for polymer fiber formation, rarely is the onset of fiber formation determined or understood from chain entanglement/viscosity measurement relationships. Instead, often a trial and error methodology is employed in the literature. The remainder of this section will highlight studies wherein empirical relationships are developed to pre-determine the onset and morphology of electrospun polymer solutions, which will emphasize the importance of chain entanglements (and consequently polymer concentration and molecular weight) to electrospun fiber formation.

Using concepts developed for conventional fiber spinning (i.e mechanically driven), Shenoy and co-workers[24] developed an empirical relationship that was accurate at determining whether electrosprayed beads, beaded fibers, or uniform fibers would arise for a polymer solution at a given concentration. This relationship was only tested against linear polymers, but was found to be accurate regardless of the nature of the polymer, solvent, and to a lesser extent the polymer/solvent interactions. Shenoy and co-workers found that if the number of entanglements in solution per polymer chain, $n(e)_{soln}$, was below 2, then only electrospun beads were produced. At $n(e)_{soln}$ between 2 and 3.5, the outcome of the electrospinning process would be beaded fibers, while if the number of entanglements per polymer chain was above 3.5 beadless fibers would be present. If the weight average molecular weight (M_w) and the entanglement molecular weight (M_e, the molecular weight of entangled portion of the polymer chain) are known, than $n(e)_{soln}$ can be plotted against the concentration of polymer using the relationship:

$$(n_e)_{soln} = \frac{(\phi_p M_w)}{M_e}$$

where ϕ_p is the volume fraction of the polymer. Shenoy and co-workers were able to determine the onset of fiber formation for various polymer solutions using this equation. The model for poly(styrene) (PS) in THF (data taken from Megelski et al[25]) is shown in Figure 1.3, and accurately predicts the electrospun polymer morphology at a given concentration. The model also accurately predicted morphologies from electrospun poly(ethylene oxide) (PEO)/H_2O, poly(D,L-lactic acid) (PDLA)/DMF, poly(L-lactic acid) (PLLA)/CH_2Cl_2, PLLA/$CHCl_3$ and poly(vinyl pyrrolidone) (PVP)/ethanol. This study exemplifies the importance of entanglements and polymer concentration on the onset and morphology (pure fibers vs. beaded fibers) of electrospun fibers.

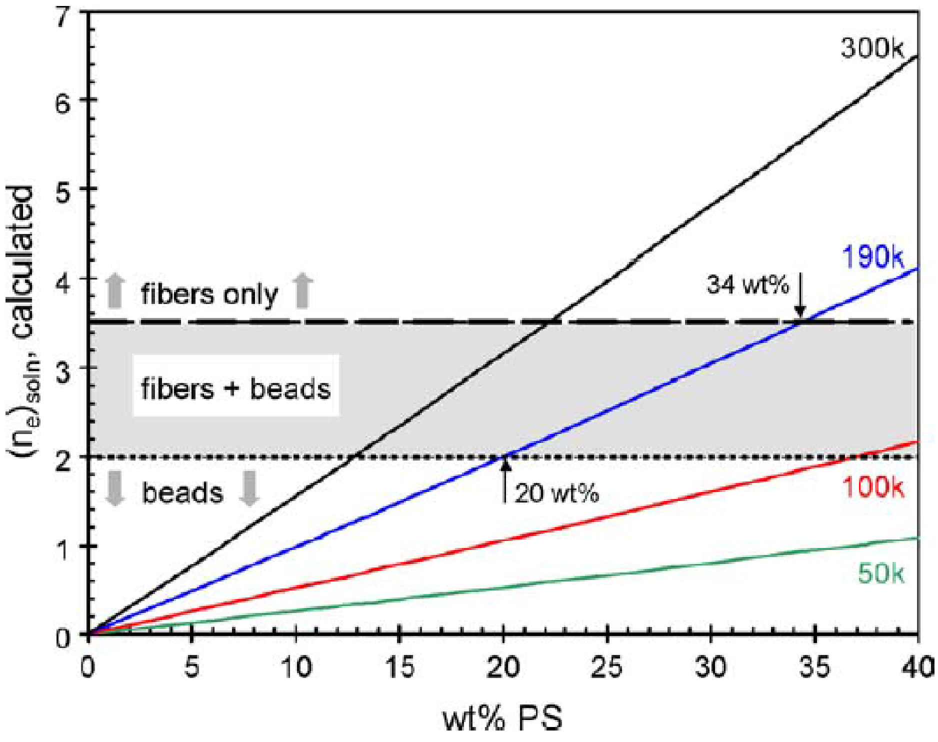

Figure 1.3. Plot of the calculated number of chain entanglements (based of M_w and M_e) as a function of polymer concentration for PS in THF. The dashed lines corresponded to transitions in the resulting polymer morphology, with each line representing a different M_w. Arrows along the 190k g/mol line indicate the onset of beaded fiber formation at 20 wt% and fibers formation at 34%, which is in good agreement with experimental data taken from reference 25. Reproduced with permission[24]. Copyright Elsevier, 2005.

The onset of fiber formation of poly(methyl methacrylate) (PMMA) of varying molecular weights was analyzed in terms of concentration by Wilkes and co-workers.[26] Three concentration regimes were studied: (1) the dilute regime, where the polymer concentration (c) is less than the critical chain overlap concentration (c^*, where the concentration inside a single polymer chain is that of the solution); (2) the semidilute unentangled regime, where c is greater than c^* but smaller than the entanglement concentration (c_e, the concentration where significant chain entanglements are observed in solution); (3) the semidilute entangled regime, where c is larger than c^*. A schematic of these three solution concentration regimes is shown in Figure 1.4 and the change in zero shear rate viscosity (η_0) as a function of c/c^* is given in Figure 1.5 for varying molecular weight PMMA. As can been seen in Figure 1.5, the crossover from the dilute to semidilute unentangled regime occurs when c equals c^* while the crossover from the semidilute unentangled to the semidilute entangled regimes occur when c/c^* equals 3. Note that the exponent of the relationship in each regime is different, indicative of an increase in polymer entanglements in solution. Wilkes and co-workers found that PMMA of any molecular weight would not form fibers in the dilute concentration regime. Similarly, only PMMA of M_w higher than 200k g/mol could form fibers in the semidilute unentangled regime, although these fibers are heavily beaded. Only in the semidilute entangled regime were fibers obtained from PMMA at most molecular weights tested, with beads becoming less prevalent in higher M_w PMMA samples. From these results, Wilkes and co-workers determined that the fiber diameter scaled with zero-shear rate viscosity to the 0.72 power. This relationship is misleading however, as low concentrations of PMMA (and thus lower viscosities) produced beads in the fibers, and the bead diameter was not accounted for in the average fiber diameter. Regardless, this study shows how concentration and molecular weight affect the morphology and onset of electrospun fibers.

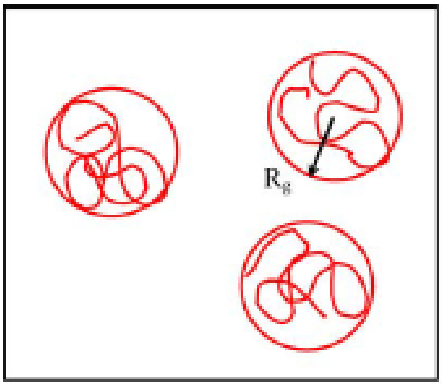

a) Dilute, $c < c^*$

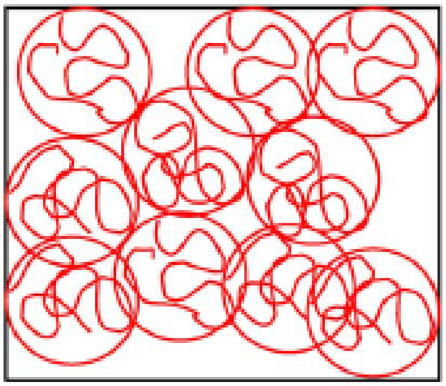

b) Semidilute unentangled, $c^*<c<c_e$

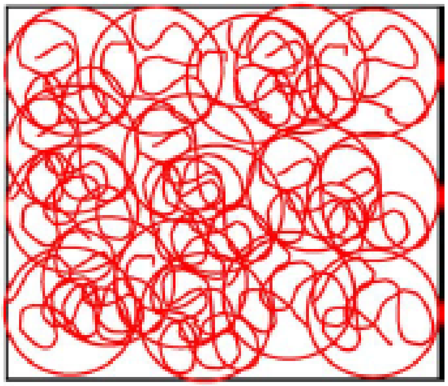

c) Semidilute entangled, $c>c_e$

Figure 1.4. Schematic diagram depicting the physical nature of polymer coils in the (a) dilute regime, (b) semidilute unentangled regime, and (c) semidilute entangled regime. Reproduced with permission[26]. Copyright Elsevier, 2005.

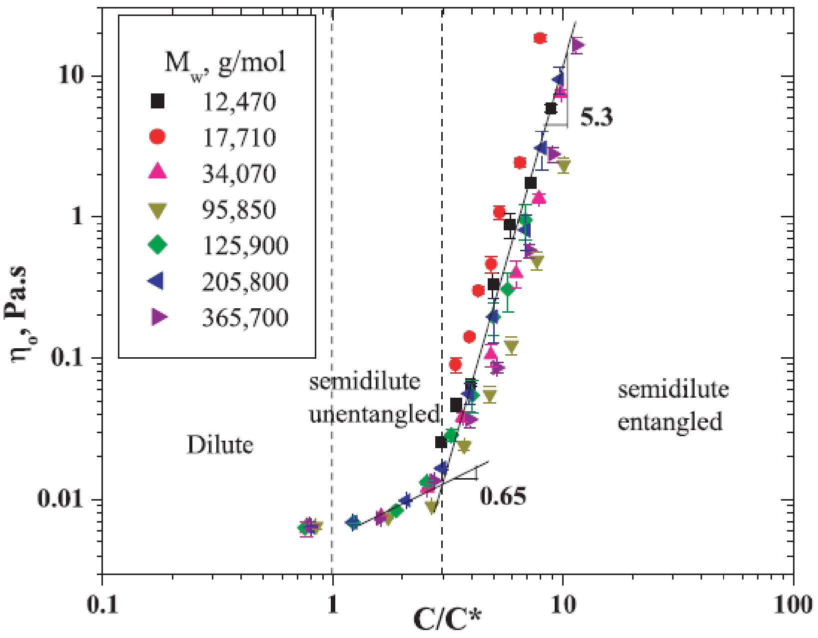

Figure 1.5. Plot of the zero shear rate viscosity vs. concentration for different molecular weight PMMA. Reproduced with permission[26]. Copyright Elsevier, 2005.

While the previous two studies both highlight the importance of entanglements, the exact role of molecular weight is not truly elucidated. That is, if a particular number of entanglements is required to form fibers, what is the difference between smaller and larger molecular weights? Shenoy and co-workers[24] hypothesize that for lower molecular weight polymers, electrospinning may be problematic when compared to high molecular weight polymers with identical number of chain entanglements per polymer chain. These authors point out that the disentanglement time (τ_D) scales with $M_w^{3.4}$, as such, shorter molecular weight chains disentangle faster than longer. As the elongation of the liquid jet and whipping of the instability region occurs on a short time scale, the disentanglement time may be an important parameter in fiber formation. This would hypothetically lead to beads in smaller molecular weight polymers compared to higher molecular weight polymers with identical number of chain entanglements. The referenced paper by Shenoy and co-workers does not show any experimental evidence to prove this, and no such follow up studies were reported. However, Shivkumar and co-workers have investigated this hypothesis. By electrospinning poly(vinyl alcohol) (PVA)/H_2O solutions of different molecular weights of the same Berry number ($[\eta]c$, which can be related to the number of chain entanglements per polymer chain), it was determined that bead formation was not seen for PVA/H_2O solutions at $[\eta]c \sim 7.5$ for molecular weights ranging from 9k g/mol to 186k g/mol.[27] Fiber thickness did increase as molecular weight increased, however. In a similar study,[28] PVA-calcium phosphate sol precursors were electrospun with the end goal of obtaining hydroxyapatite fibers. With a Berry number of 12, the morphology of the precursor fiber was studied for different concentrations of sol in the initially solution. While PVA fibers without precursor did not exhibit any beads at lower molecular weight (similar to the previous study[27]), an increase in sol concentration led to bead formation at for lower molecular weight samples (M_w = 40.5k g/mol) but not in higher molecular weight samples (M_w = 155k g/mol, 67.5 g/mol) until the sol volume percentage exceeded 50%. It was concluded that the sol precursor must be preventing polymer chain entanglements from occurring. PS/THF solutions were also studied by Shivkumar and co-workers[29], where it was found that bead formation was more prevalent in smaller molecular weight polymers than in higher molecular weight polymers with a Berry number of 9. While some of these results confirm the initial hypothesis from Shenoy and co-workers, a systematic study of various degrees of chain entanglement (*i.e.* Berry number) has yet to be performed in order to determine a threshold number of chain entanglements at which bead formation in lower molecular weight polymers would hypothetically occur.

1.2.1.2 Electrical Energy vs. Surface Energy

While chain entanglements can dictate the formation of electrospun fibers, the process of fiber formation is driven by opposing electrical and surface energy forces. As stated in Section 1.2, the electrospinning process initiates when the electrical energy exceeds the surface tension in a Taylor cone. As the liquid jet is accelerating toward the collector, an electrical energy acts as a driving force for fiber formation, while the surface tension counteracts this force. The dimensionless electrospinning number, $Vq/\Upsilon R^2$, proposed by Shenoy and co-workers[24], is a good metric for examining the onset of fiber formation from a force balance standpoint. The numerator of the electrospinning number represents the electrical energy (applied voltage and amount of charge) while the denominator represents surface free energy (surface tension and liquid jet cross-sectional area). Liquid jet ejection from the Taylor cone occurs when the electrospinning number is greater than 1. That is, once the applied voltage (or more accurately, the applied field strength) is sufficient enough to overcome the surface energy of the Taylor cone, a liquid jet ejects from the cone. As the applied voltage increases, the morphology is known to change from beads, to bead and fibers and finally to fibers; often with a decrease in fiber diameter with increasing electrospinning number once the fiber regime is obtained. However, if the electrical energy is increased further this could negatively impact bead-free fiber formation Taylor cone and liquid jet stability can be affected.

An increase in the electrical energy term can have varying effects on the morphology and diameter of electrospun fibers. It is generally accepted that bead formation can be reduced with the increased electrical field strength. For example, Zou et al.[30] were able to remove beads from a 4 wt% poly(hydroxybutyrate-*co*-valerate) (PHBV) in $CHCl_3$ by increasing the applied voltage from 10 kV to 30 kV at a spinneret to substrate distance of 30 cm. However, higher voltages may affect the stability of the liquid jet and induce bead formation in the fibers. Tan and co-workers[31] demonstrated this by electrospinning PEO/H_2O (7 wt%) at voltages of 5.5, 7.0 and 9.0 kV. At the latter two voltages, bead formation occurred. Increases in applied voltage can also lead to reduced fiber diameter[32] and increased fiber diameter distribution.[33]

Increasing the electrospinning number can also be accomplished by other techniques. These include using a more conductive solvent, adding salts (both of which increase the value of q), and adding surfactants (decreasing the value of Υ). The effect of solvent conductivity on the electrospinning of PS solutions was reported by Shivkumar and co-workers[34] and Uyar and co-workers.[35] Shivkumar's group found that when PS (M_w = 393.4k g/mol) was electrospun from 7 wt% solutions of low conductivity solvents (THF, $CHCl_3$, and CS_2), 30 μm size beads were obtained, while 7 wt% solutions of DMF (much more polar than other tested solvents) produced fibers with only a small amount of beads that were much smaller (~5 μm) in size. Using 20wt% solutions of PS (M_w = 280k g/mol), Uyar and co-workers were able to obtain bead free PS fibers from DMF, but not from THF or $CHCl_3$. The addition of salts can increase the amount of charge carriers in the liquid jet without affecting the surface tension. Li and Xia demonstrated this using PVP in a water/ethanol solution (Figure 1.6).[14] At 7 wt% bead free fibers were obtained, while at 5 and 3 wt% beads were present in the fibers. The beads were larger and more numerous fibers electrospun from the 3 wt% solution. With the addition of 0.35 mg/mL of tetramethylammonium chloride to the 5 wt% solution, beads were no longer present in the fiber mat while fiber diameter was significantly reduced. Bead removal and fiber thinning has also been accomplished using NaCl for PEO fibers[36] and LiCl for PS fibers.[37] Using the non-ionic surfactant Triton X-405, Lin and co-workers[38] were able to reduce the number of beads in a 10 wt% PS solution in THF/DMF at a 1% (w/v), while the cationic surfactants dodecyltrimethylammonium bromide (DTAB) and tetrabutylammonium chloride (TBAC) reduced beads in 10 wt% PS while simultaneously reducing the fiber diameter. The use of ionic surfactants not only reduces the surface tension in the polymer solution, but also increase the amount of charge; thus increasing the electrospinning number even further.

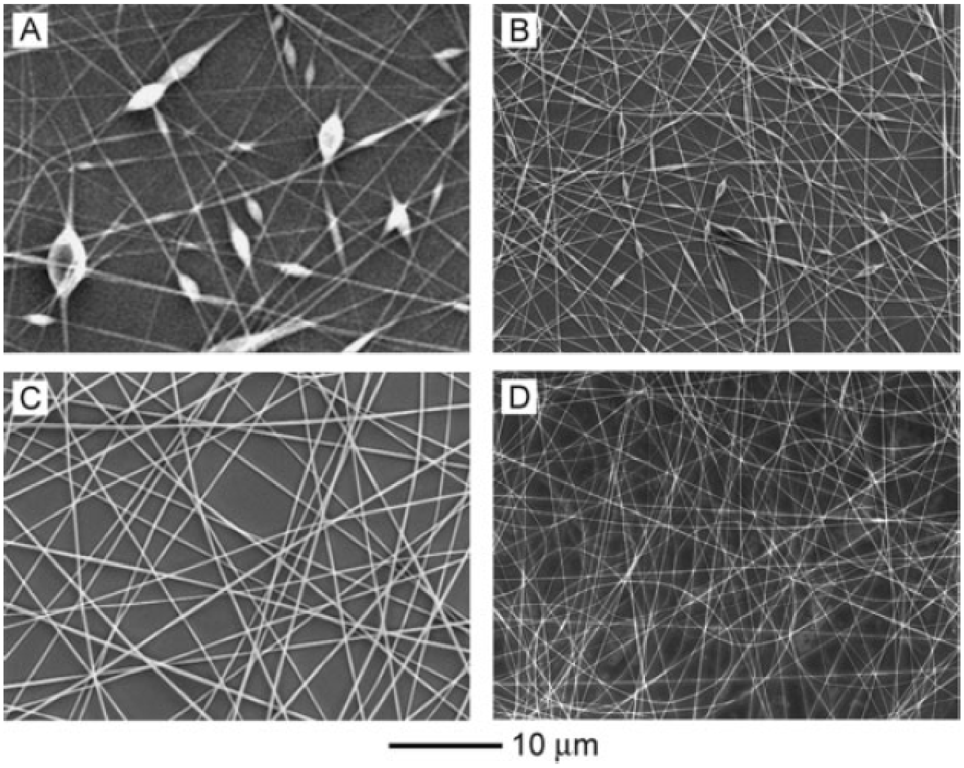

Figure 1.6. SEM images of PVP fibers electrospun from a 16:3 ethanol : water solution at a) 3 wt%, b) 5 wt%, c) 7 wt% and d) 5 wt% with 0.35 mg/mL of tetramethylammonium chloride. Reproduced with permission[14]. Copyright Wiley-VCH, 2004.

1.2.1.3 Spinneret to Substrate Distance

The distance between the spinneret and substrate can play a critical role in the morphology of electrospun fibers as this distance can influence the phenomenon discussed in Sections 1.2.1.1 and 1.2.1.2. Sufficient distance is needed for the solvent to fully evaporate, otherwise very large fibers may be obtained and fibers may "melt" into one another due to the comparatively large percentage of residual solvent. The spinneret to substrate distance also affects the electrical field strength, which in turn has been shown to influence the morphology of electrospun fibers (see section 1.2.1.2). The larger the distance needed for complete solvent evaporation, the larger the applied voltage needs to become in order to maintain a particular electric field strength. Furthermore, the conductivity of the solvent can affect the minimum spinneret to substrate distance. The more conductive the solvent, the smaller the liquid jet becomes (due to electrostatic repulsion) which increases the surface area of the liquid jet and allows for faster evaporation. Therefore, an ideal solvent for electrospinning (outside of the obvious requirement of complete dissolution of the polymer in question) should have a low boiling point and high conductivity. For this reason, popular solvent systems for electrospinning are DMF/$CHCl_3$ or DMF/THF. DMF has a high conductivity for an organic solvent, but a high boiling point (153 °C), while $CHCl_3$ and THF are not as conductive but have low boiling points (61.2 and 66 °C respectively). While the spinneret to substrate distance in itself does not directly affect the morphology of electrospun fibers, it does affect other parameters that play a role in the morphology of electrospun fibers.

1.2.1.4 Humidity

Humidity can affect the morphology of electrospun fiber and should at the very least be monitored if not completely controlled. Depending on the nature of the electrospinning solution, humidity can either induce a particular surface morphology and/or influence fiber diameter. Reneker and co-workers[39] studies the influence of relative humidity (RH) on the morphology of PEO fibers electrospun from aqueous solutions. The authors observed a transition from uniform fibers to bead fibers at 52.6 % RH. As PEO is readily soluble in water, the influence of water vapor in the air effectively dilutes the PEO concentration in the liquid jet which likely reduces the number of entanglements in solution. Hardick et al[40] also examined the morphology of electrospun cellulose acetate (CA) fibers spun from an acetone/DMF/ethanol solution. The observation from these authors is different than those from Reneker's group. At increasing RH, Hardick et al observed an increase in fiber diameter with increasing RH. This was attributed to a change in the evaporation rate in the fibers, as CA is known to absorb water moderately well due to the high degree of hydrogen bonding. Rabolt and co-workers[41] studied the effect of RH on electrospun PS fibers (a material that does not dissolve or form hydrogen bonds with water). These authors found that with RH above 30%, pores would form on the surface of the electrospun PS fibers, with increasing RH leading to a larger number of pores (Figure 1.7). The increased number of pores was attributed to water condensation on the liquid jet as solvent (THF) evaporated to form PS fibers. The pores represented areas where water droplets were present.

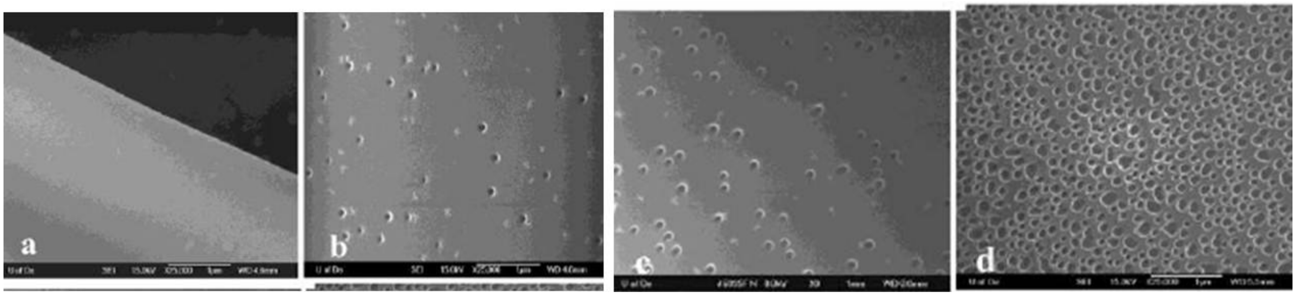

Figure 1.7. SEM images of PS fibers electrospun under a) <25% RH, b) 31-38% RH, c) 40-45% RH, and d) 50-59% RH. Reproduced with permission[41]. Copyright the American Chemical Society, 2004.

1.3 Modifications to Conventional Electrospinning

1.3.1 Coaxial Electrospinning

To enhance the properties of electrospun fibers, a concentric dual nozzle method known as coaxial electrospinning is used to produce fibers with various two-phase architectures.[42] Distinctive properties from both the core phase and sheath phase can be combined to obtain a fiber mesh exhibiting a set of properties that may not be obtained from one single material or blended materials. By using the added versatility from coaxial electrospinning, fiber meshes can be made with superior and more precise functionality. The processing parameters that govern the onset and morphology of fibers made by coaxial electrospinning are similar to that of conventional electrospinning. However, as the two liquid jets are in constant contact, the differences in rheological and conductive properties can influence the composition of the two-phase fibers. Flow rate ratio between the core and sheath solutions can be used to tune the thicknesses of the core and sheath phases. Polymer solubility in both core and sheath solvent systems are require to prevent precipitation of the polymeric material. As there is a fair amount of material available of the use of coaxial electrospinning (Figure 1.8), the remainder of this section with highlight the more novel uses of coaxial electrospinning (*i.e.* the creation of hollow nanotubes or the coaxial electrospinning of solution systems where one solution is not electrospinable alone, such as those highlighted in this thesis).

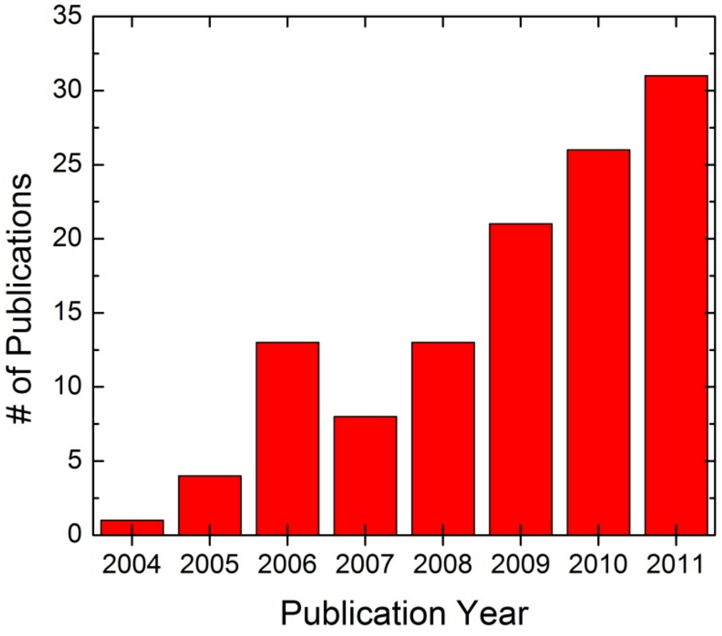

Figure 1.8. Number of publications on coaxial electrospinning per year as determined using SciFinder Scholar. Data taken on 10/02/2011.

Inorganic nanotubes can be made via coaxial electrospinning. This is typically accomplished using a sheath material containing a sol precursor, which after subsequent thermal processing yields the inorganic nanotubes. Using this methodology, Li and Xia were able to make TiO_2 nanotubes.[43] This was accomplished by electrospinning a PVP/TiO_2 precursor as a sheath solution and a mineral oil as the core solution. The TiO_2 precursor was allowed to hydrolyze in air for one hour, followed by extraction of the mineral oil with octane and calcination at 500 °C for one hour. The resulting hollow fibers had an inner diameter of ~200 nm and a polycrystalline structure with an average grain size of approximately 10 nm. Using a similar technique, Kameoka and co-workers used a similar technique to create silica nanotubes.[44] The inner diameter of the silica nanotubes was ~60 nm. The authors were able to achieve singe molecule detection of 5-iodoacetamidofluorescein (IAF) using an 800 nm pulsed laser, as shown in Figure 1.9.

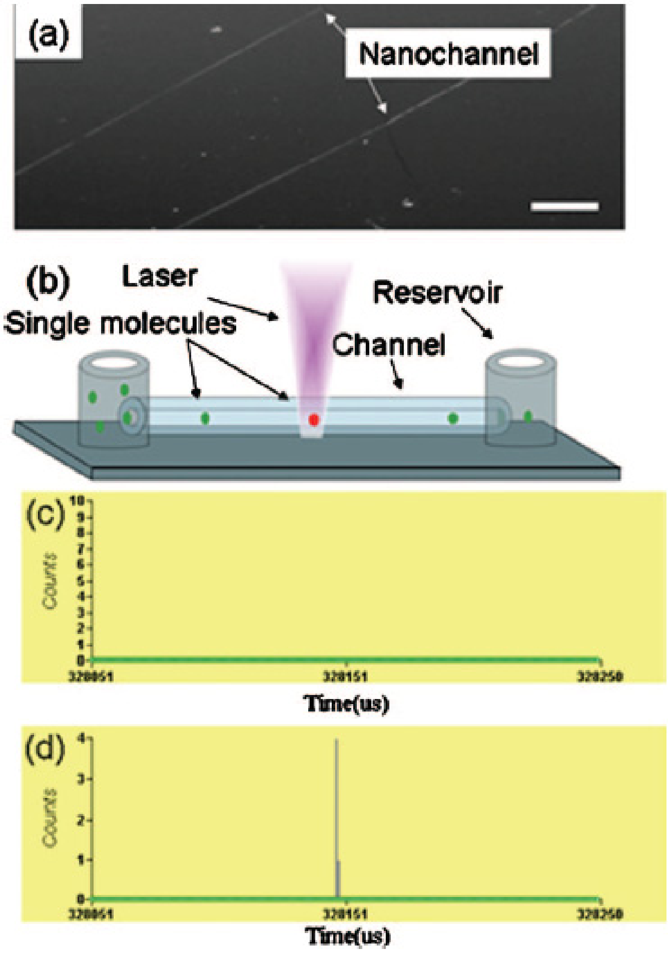

Figure 1.9. Single molecule detection of IAF using silica nanotubes created by coaxial electrospinning: a) fluorescent micrograph of nanotube filled with IAF, b) schematic of the single molecule detection set-up, and single molecular detection c) without the presence of IAF and d) with the presence of IAF. Reproduced with permission[44]. Copyright the American Institute of Physics, 2006.

Coaxial electrospinning can also be used to incorporate materials that cannot be electrospun or are difficult to electrospinning as stand-alone fibers. This can be accomplished by electrospinning such a material within the core of an electrospinable material or along the periphery of an electrospinable material. Work presented in this thesis[45] and work performed by co-workers[46] at the University of Cincinnati demonstrates this idea by creating fibers consisting of a non-electrospinable sheath materials. In this thesis, a dispersion of titania was used as a sheath material to create photocatalytic fiber meshes for decontamination purposes. The details for this study are presented in Chapter 4.[45] Han and Steckl[46] created hydrophobic and oleophobic fibers by using a low concentration solution of Teflon as the sheath solution and PCL as a core solution. As the Teflon solution exhibits low conductivity, it was "guided" along the periphery of the PCL liquid jet during fiber formation, successfully creating a PCL/Teflon core/sheath fiber mesh. Similar work was also reported by Sigmund and co-workers.[47] Encapsulation and controlled spatial localization of functional nanoparticles is also possible using coaxial electrospinning by placing the nanoparticles within the core of the polymer. This has been demonstrated by Shah and co-workers[48] and Song and coworkers[49] using magnetic nanoparticles. Obtaining fibers that have proven to be difficult to electrospin can be accomplished using coaxial electrospinning. This is accomplished by stripping the sacrificial outer sheath material to obtain the single phase fiber if an orthogonal solvent can be found between the two systems. This technique is used to create P3HT:PCBM fibers from coaxial fibers containing PCL as a sheath in Chapter 2.[50]

1.3.2 Fiber Alignment

The deposition of nanofibers is a random process under normal electrospinning conditions. However, fiber alignment can be achieved if an appropriate electrode set-up is used. A spinning disk/cylinder collecting electrode is often used to align fibers when the rotation speed is sufficiently high enough.[51] Fiber alignment is not perfect, however, and is predominately found on the edges when a rotating disk collector is used. A more elaborate way to align electrospun fibers is by using a multi electrode system, such as those by Li et al.[52,53] Using these electrode configurations, fibers fall in the gap between collectors in an aligned fashion (Figure

1.10). This alignment is vastly improved compared to using a rotating collecting electrode. Fiber alignment can be beneficial in many applications, including neural and skeletal tissue scaffolds (see section 1.4.1) and electronics (see section 1.4.5).

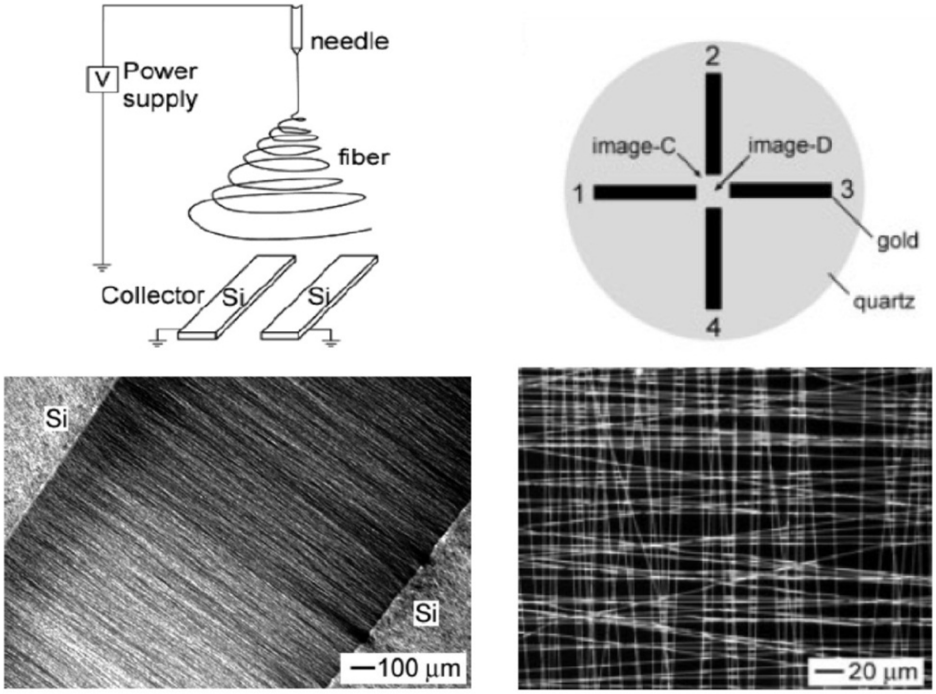

Figure 1.10. Schematic diagrams of electrode for fiber alignment, along with optical microscope images of the aligned fibers. Reproduced with permission[52,53]. Copyright Wiley-VCH, 2004 and the American Chemical Society, 2003.

1.3.3 Near-Field Electrospinning

For near perfect alignment and patterning of electrospun nanofibers, a technique known as near field electrospinning[54] (NFES) can be utilized. NFES can be thought of as an electrostatic analog to dip pen nanolithography (DPN). In NFES, the tip-to-collector distance is usually around 500 μm with voltages between 1-2 kV. Fiber collection is on an x-y stage, allowing for programmable control over the deposition of fibers. One consequence of this short distance is that the solvent does not fully evaporate, causing larger diameter fibers than those typically seen in conventional electrospinning. Changes in fiber morphology after deposition also occur due to the remaining solvent. One way to get around these shortcomings is to reduce the initial diameter of the liquid jet at the droplet. Chang and co-workers[55] accomplished this by initially drawing a very fine viscoelastic jet using a sharp tungsten probe, followed immediately by an application of an external electric field. Using this method, Chang and co-workers could make precise patterns and logos with poly(ethylene oxide) (PEO) fibers of ~150 nm diameters (Figure 1.11). More recently, Chang and co-workers generated a piezoelectric nanogenerator with poly(vinylidene fluoride) (PVDF) nanofibers using NFES.[56] While NFES offers unprecedented control over fiber patterning and alignment, experimentally it is much more difficult to perform when compared to conventional electrospinning methods. DPN, which can be performed on atomic force microscopes (AFM), is much more practical as AFMs are ubiquitous in most research facilities.

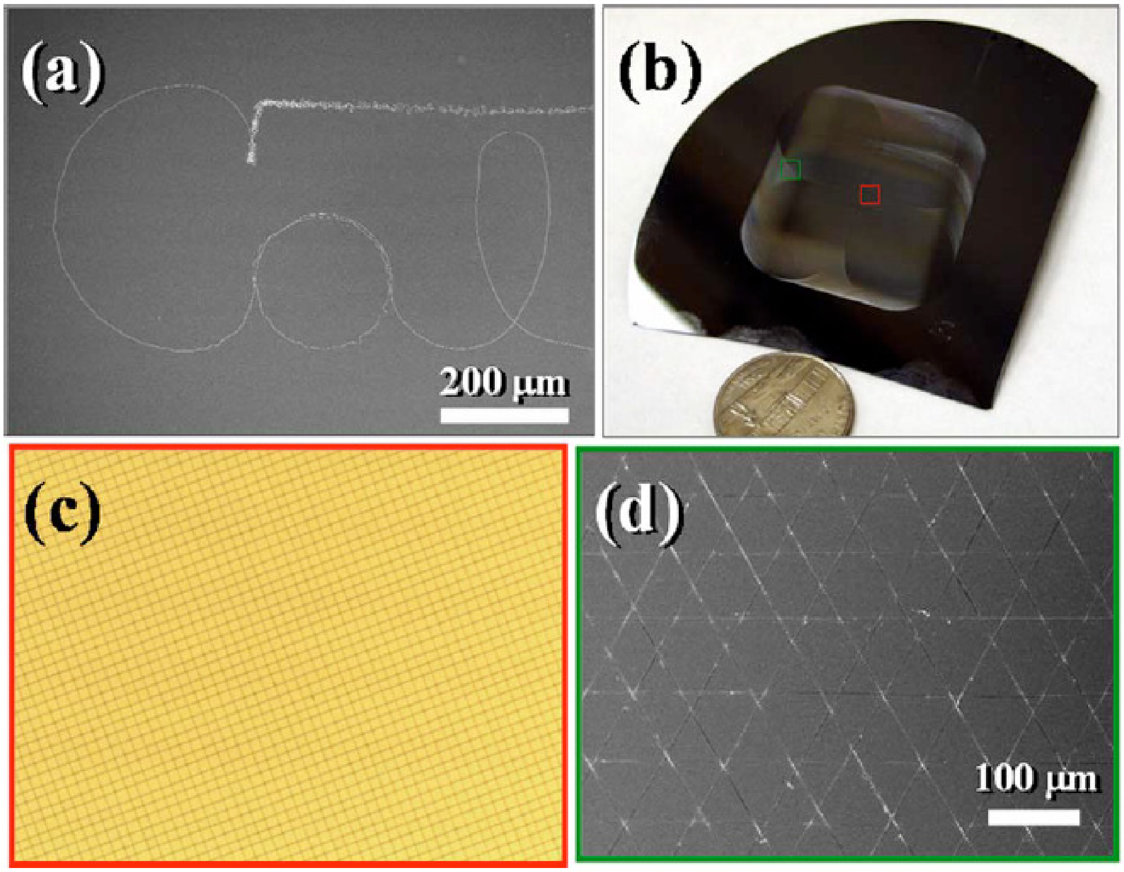

Figure 1.11. PEO nanofiber patterns created by NFES: (a) University of California-Berkeley logo, (b) single PEO nanofiber electrospun on a 4 × 4 cm^2 silicon chip, (c) patterned PEO nanofiber squares shown from the red square in (b), and (d) patterned PEO nanofiber triangles shown in the green square in (b). Reproduced with permission[55]. Copyright the American Institute of Physics, 2008.

1.4 Application Areas

This next section will highlight previous research in application areas discussed in the latter chapters of the thesis (environmental, electrical, and energy applications) as well as more common application areas (such as biomedical, filtration and sensors). The number of publications and patents per application area is given in Figure 1.12.

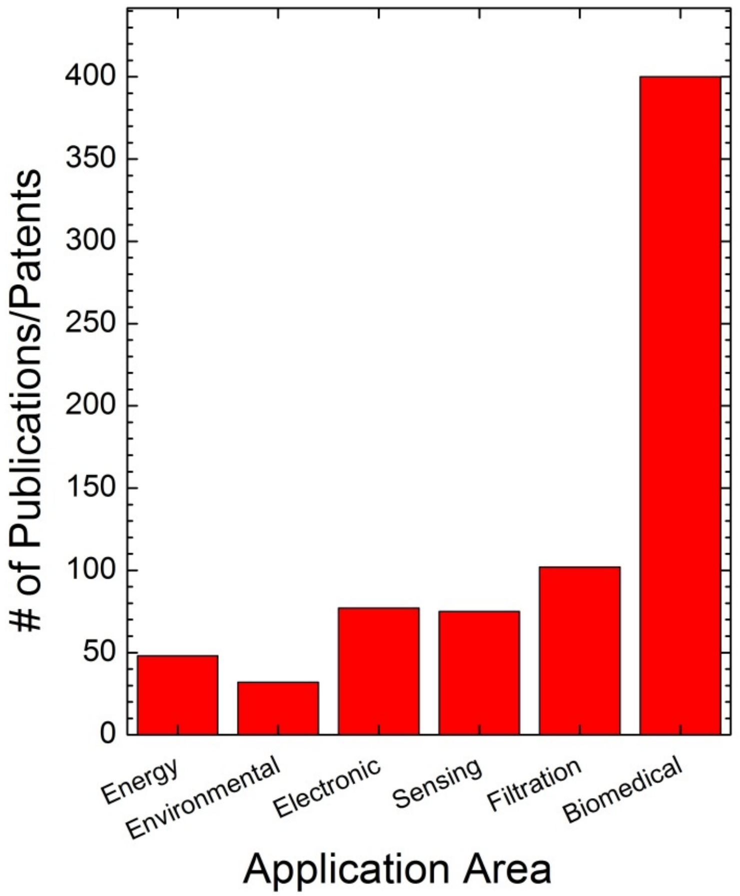

Figure 1.12. Number of publications and patents per application area. Data obtained using SciFinder Scholar and taken on 10/02/2011.

1.4.1 Biomedical

As can be seen in Figure 1.12, biomedical applications are the most studied area of electrospun fibers. The large majority of these studies focus on using electrospun fibers for tissue engineering purposes. Non-woven electrospun fiber mats are ideal three-dimensional mimics of the extracellular matrix (ECM, consisting mainly of nano-scale collagen fibers) for cell attachment and growth.[57] Electrospun fibers can also be doped and/or functionalized with appropriate growth factors to increase the growth and proliferation of cells. Furthermore, therapeutic agents can be encapsulated into electrospun fibers to allow for controlled release. This section will give a brief review on some of the more relevant papers in this field.

The concept of using electrospun fibers consisting of biodegradable/biocompatible materials for tissue engineering was first discussed by Bowlin and co-workers.[58,59,60] Although cell culture studies were not presented in their initially papers, their publications the first to show the electrospinning of biomaterials such as poly(glycolic acid) (PGA),[58] collagen,[59] and fibrinogen.[60] Li et al.[61] and Bhattarai et al.[62] were the first to report on cell growth and proliferation on electrospun fibers. Using poly(lactide-*co*-glycolide) (PLGA) fibers (500-800 nm in diameter), Li et al. created fibrous non-woven scaffolds seeded with human bone-marrow-derived mesenchymal stem cells (hMSCs). After one week, the amount of hMSCs more than tripled. Similar experiments were also reported by Li et al. on BALB/c C7 mouse fibroblast cell. The amount of cells seen within the electrospun fiber mesh after three and seven days of cell culture can be seen in Figure 1.13. Bhattarai et al. used poly(*p*-dioxanone-*co*-lactide)-block—poly(ethylene glycol) (PPDO/PLLA-b-PEG) electrospun fibers (average diameter of 300 nm) to culture NIH 3T3 fibroblast cells. Nearly seven-fold enhancements in number of cells were achieved using these materials. These papers would help serve as a catalyst for a large surge of publications using electrospun fibers for tissue engineering. A large number of possibilities exist for the use of electrospun scaffolds in tissue engineering, but the majority of research is found in engineering epidermal tissue, bone tissue, and neural tissue.

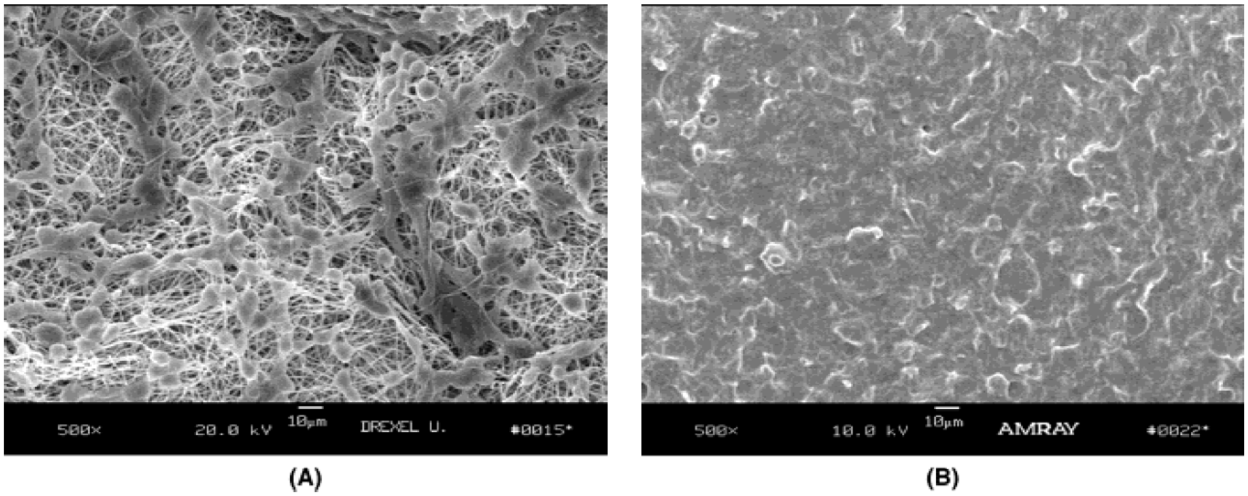

Figure 1.13. Growth of BALB/c C7 mouse fibroblast cells on PLGA electrospun fibers meshes. SEM images are taken after (A) three days of cell culture and (B) seven days of cell culture. Reproduce with permission[61]. Copyright Wiley-VCH, 2002.

For epidermal scaffolds made by electrospinning, the majority of materials used are the connective proteins collagen and gelatin. Both collagen and gelatin show the cell growth and proliferation needed successful tissue replacement. A major issue with these materials is that they exhibit poor mechanical properties, particularly when hydrated. To improve the mechanical properties, Zhao et al.[63] used coaxial electrospinning to produce a gelatin (sheath material)/poly(caprolactone) (PCL, core material) scaffold. Using a core-shell fiber architecture, the gelatin shell could still be in contact with seed cells while the core PCL material would provide mechanical stability. The core-shell fiber scaffold was found to have improved mechanical properties, which improved with an increasing core diameter radius. The gelatin coated fibers were found to grow a larger amount of M.DUNNI (clone III8C) mouse dermal fibroblasts CRL-2017 cells than non-coated PCL fibers.

Aligned electrospun nanofibers have been used to grow neurons, as they both have highly anisotropic structures. Ramakrishna and co-workers[64] found that aligned nanofibrous poly(L-lactic acid) (PLLA) scaffolds increased the growth rate of neural stem cells (NSC) compared to randomly aligned PLLA scaffolds in vitro. The alignment helped neurites of the NSC to growth parallel with one another which contributed to the higher growth rate. Nanofibers with smaller diameters were also found to grow longer neurites on average. Leong and co-workers,[65] used poly[(ε-caprolactone)-co-(ethyl ethylene phosphate)] (PCLEEP) electrospun fibers loaded with human glial cell-derived neurotrophic factor (GDNF) for nerve cell growth. PCLEEP fibers, loaded with and without GDNF, were electrospun in an aligned fashion onto PCLEEP films. These fiber/film composite were then rolled up into tubes for guided nerve guide generation. Fibers were aligned either parallel or perpendicular to the tube axis. An initial burst release of GDNF from electrospun PCLEEP fibers was observed, followed by a slow release over a 100 day period. These electrospun fiber based nerve guides were then surgically placed in rats with severed nerves. Nerve guides containing electrospun fibers were found to successfully regenerated nerves in nearly all the rats tested (9-10 per sample). The control group (PCLEEP films only) exhibited 33% success rate in nerve regeneration. Cross sections of regenerated nerve cells are shown in Figure 1.14.

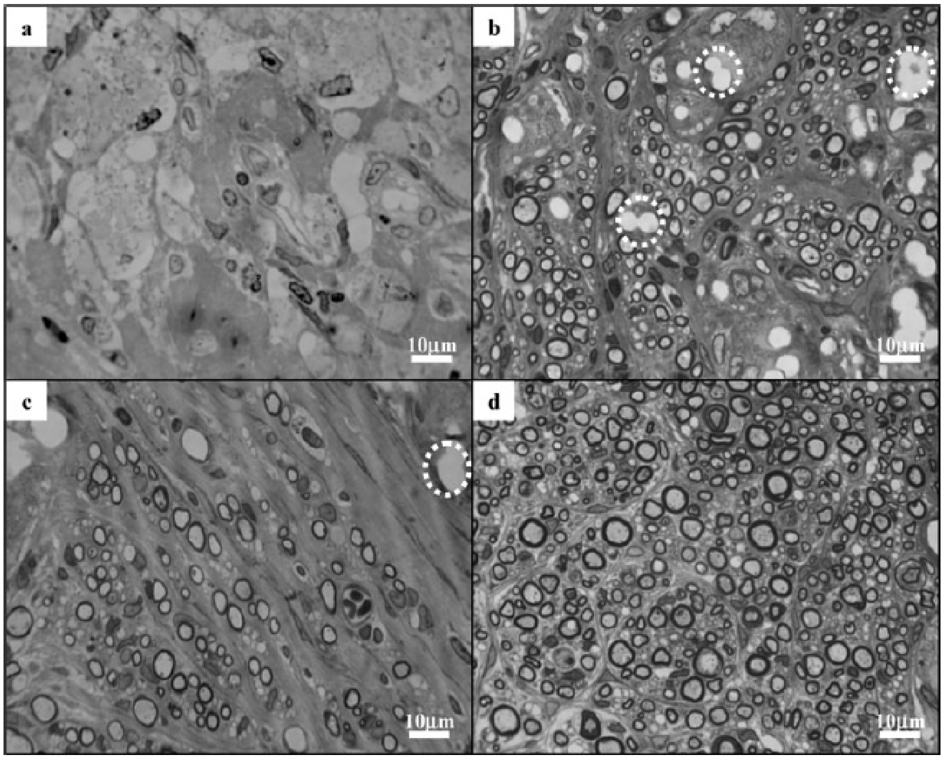

Figure 1.14. Light microscopy cross sections of nerve cells grown on (a) PCLEEP film nerve guides, (b) fiber/film nerve guide with fibers aligned along the tube axis, (c) fiber/film nerve guide with fibers aligned perpendicular to the tube axis, and (d) fiber(GNDP)/film nerve guide with fibers aligned along the tube axis. Dashed regions highlight voids left over from electrospun PCLEEP fibers. Reproduced with permission[65]. Copyright Wiley-VCH, 2007.

Nanofiber alignment also plays a similar role in the growth skeletal tissues. Lee and coworkers[66] have found that aligned PCL/gelatin blended fiber scaffolds had enhanced growth of human skeletal muscle cells (hSkMCs) than those made from randomly orientated fibers (Figure 1.15). Wang and coworkers[67] electrospun poly(lactic-co-glycolic acid) (PLGA)/ hydroxyapatite (HA) nanoparticle composite nanofibers with and without bone morphogenic protein 2 (BMP-2) and tested the ability to heel bones in mice. The results (Figure 1.16) show the benefit of BMP-2 inclusion, as the broken bone is fully healed after one week.

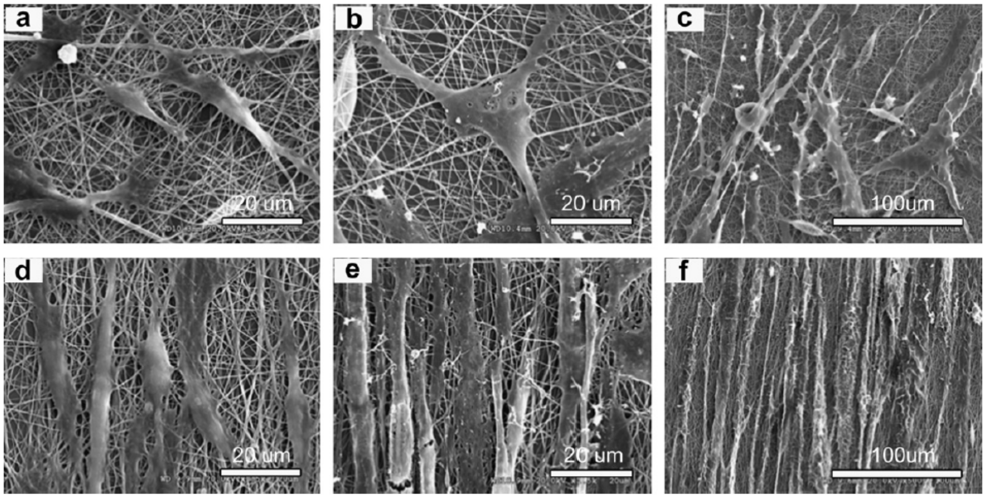

Figure 1.15. SEM images of hSkMCs grown on randomly oriented PCL/collagen nanofibers (panels a-c) and oriented PCL/collagen nanofibers (panel d-f) after one day (panels a and d), three days (panels b and e) and seven days (panels c and f). Reproduced with permission[66]. Copyright Elsevier, 2008.

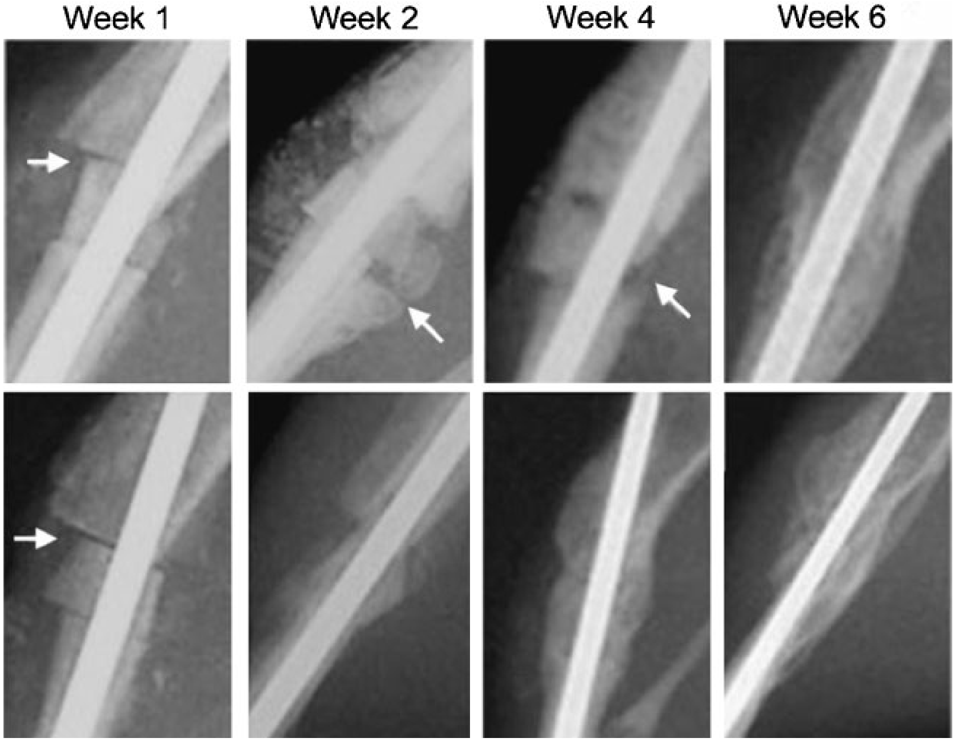

Figure 1.16. Effect of electrospun PLGA/HA scaffolds with and without BMG-2. The top panel is without BMG-2 and the bottom is with BMG-2. White arrows indicate bone fracture. Reproduced with permission[67]. Copyright Wiley-VCH, 2008.

As shown in the above tissue engineering examples, electrospun nanofiber scaffolds can be used as drug delivery/controlled release agents. Wnek and coworkers[68] were the first to explore the use of electrospun fibers for the sustained release of drugs. They tested the release of tetracycline hydrochloride, an anti-infective agent, in poly(lactic acid) (PLA), poly(ethylene-co-vinyl acetate) (PEVA), and blended (50:50) electrospun fiber scaffolds. It was found the PEVA and the blended fiber mats had the best controlled release properties, and that the controlled release properties were better than those of cast films of identical chemical composition and to Actisite®, a commercially available drug delivery system. Hadjiargyrou and coworkers[69] presented a polymer scaffolds for therapeutic application in gene delivery. Plasmid DNA could be released (70-80% of initially loaded amount) from scaffolds of PLGA and poly(D,L-lactide)-poly(ethylene glycol) (PLA-PEG) block copolymers over a 20 day period. It was found that the release DNA plasmid was fully intact, capable of cellular transfection, and could be used to encode proteins.

1.4.2 Filtration

Filtration is major application area for electrospun fibers as the process of filtration is necessary in nearly-all engineering fields. Fibrous filtration media have are traditionally predominate in filters due to the combined low air resistance and high filtration efficiency.[70] Electrospun fibers are currently being used in filters due to the smaller size scales compared to traditional fibers. This is important as the structural components of the filter must be on the size scale of the particles or droplets to be captured in the filter.[70] However, the smaller size of electrospun fibers can lead to lower mechanical properties which could lead to filter failure in many filtration applications. Therefore, electrospun fibers are typically deposited onto a non-woven macro-fibrous filter media. The filtration efficiency and pressure drop are the two most important properties of a filter. The filtration efficiency (η) is defined as:

$$\eta = 1 - \frac{N_2}{N_1}$$

where N_1 and N_2 are the concentration of particles at the inlet and outlet of the filter respectively (usually in mg/m^3). The pressure drop (ΔP) across the filter is given as:

$$\Delta P = \frac{2C'v^2 H\rho_a}{\pi d_f^2}$$

where C' is the resistance coefficient, v is the filtration velocity, H is the thickness of filtration layer, ρ_a is the gas density, and d_f. In general terms, the filtration efficiency increases for filters with smaller fibers diameters, but the pressure drop across the filter will increase. As such, the balance between filtration efficiency and pressure drop is often investigated.

Work by Qin and Wang show the interplay between filtration efficiency and pressure drop nicely.[70] Poly(vinyl alcohol) (PVA) solutions were electrospun onto poly(propylene) filtration membranes and tested against 0.6 µm diameter NaCl aerosol particles at a penetration velocity of 5 m/min. Unsurprisingly, Qin and Wang found that filtration efficiency increased with increased amount of electrospun fibers (nearly 100% efficiency at a 1.0 g/m^2), which also increased the pressure drop across the filter. With 1.0 g/m^2 electrospun fibers the pressure drop was ~300 Pa, while 3.0 g/m^2 electrospun fiber coverage lead to a drastic increase in pressure drop to ~2800 Pa. However, in the range between 1.0 to 3.0 g/m^2 of electrospun fibers, the filtration efficiency was maintained at ~100%. Therefore, the authors concluded that 1.0 g/m^2 was the optimal amount of electrospun fibers to achieve high filtration efficiency while maintaining a modestly low pressure drop. Various similar studies exist in the literature,[71,72] where pressure drop and filtration efficiency relationships are explored. It worth noting that none of these aforementioned papers investigate the use of functionalized filtration, wherein active materials can help eliminate harmful contaminates.

1.4.3 Sensors

The ever growing need for highly sensitive and selectivity chemical sensors for use in biomedical, environmental, and military defense applications remains a major challenge in materials engineering. Increasing the SVR of the sensor material can solve the sensitivity issue due to the increased surfaces available for analyte-sensor interactions. As such, electrospun fibers have been explored as potential sensor candidates. While electrospinning can be used to create materials with a high SVR, the selectivity of these sensors is rather poor due to the choice of materials used for electrospinning. Unless the material has a binding site for a specific analyte, any change in signal (be it optical or electric) could potentially arise from a class of different substrate/analyte interactions (ionic, π-π stacking, hydrophilic/hydrophobic, size, chemical reactions, etc.). This section of the thesis will highlight the important works in this area.

Single nanofiber ammonia (NH_3) gas sensors were developed by Craighead and co-workers,[73] wherein the resistance across a single nanofiber was measured to detect NH_3. The conductive fibers were electrospun across gold electrodes (made by photolithography methods) using a microfabricated scanned tip set-up developed by the group.[51] Fibers were electrospun across the gold electrodes at a potential of 8.5 kV and a tip to collector distance of 1.5 cm from a 2 wt% PANI/0.25 wt% PEO solution in chloroform, with fibers ranging from 100-500 nm .

Current/voltage measurements were taken from the gold electrodes to measure the nanofiber's response to NH_3.

In these experiments, it was shown that PANI/PEO electrospun nanofibers could sense NH_3 concentrations as low as 0.5 ppm measured by both constant current and constant voltage experiments (Figure 1.17). It was also shown that the response time of the single fiber device was dependent on the fiber diameter, with smaller diameter fibers having a quicker response time due to radius-dependent diffusion of the NH_3 through the PANI fiber. The response to NH_3 was demonstrated to be reversible by cycling pulse of NH_3 and N_2 with time. The single nanofiber NH_3 sensors fabricated here outperform those made from films in terms of sensitivity. It is difficult to make a comparison between response times since the references given in the Craighead and co-workers study do not show conductance vs. time measurements at the same NH_3 concentration, but it was shown by Matsuguchi and co-workers[74] that a film of PANI/poly(styrene) had a response time of ~ 40 seconds to 500 ppm of NH_3. In this study there was no mention of film thicknesses or spin coating parameters to make a comparison to the nanofiber sensors. From a purely geometrically standpoint, the ability to form single uniform fibers is also beneficial as it allows for easier electrical characterization/calculations compared to a mat of randomly aligned fibers.

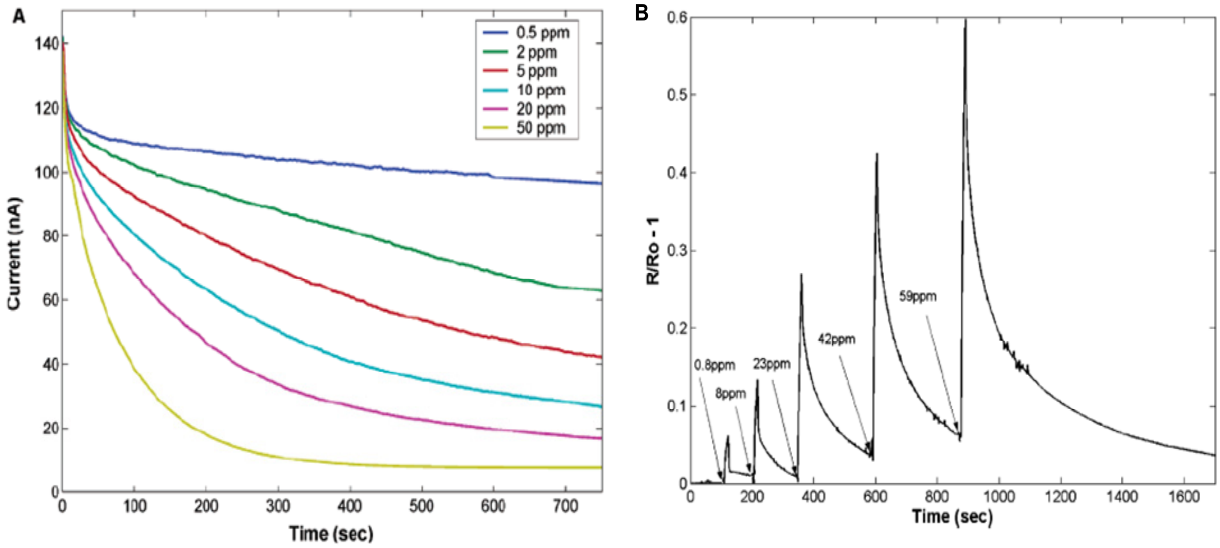

Figure 1.17. (a) Current vs. time measurements for 335 nm PANI/PEO nanofiber with exposure to different amounts of NH_3. (b) Real-time response of a 300 nm PANI/PEO nanofiber to NH_3/N_2 cycles. Reproduced with permission[73]. Copyright the American Chemical Society, 2008.

Wang et al.[75] developed a quenching based sensor by electrospinning a blend of dye derivatized PAA and cross-linkable polyurethane (PU) latex for the detection of cationic species and nitro-containing aromatic compounds. The dye used in this experiment is pyrene methanol (PM) and was chosen because of its optical properties and non-toxicity. The covalent bonding between PAA and PM is shown in Figure 1.18. Fibers were electrospun from an 18.6 wt% PAA-PM/36.5 wt% PU solution in DMF with an applied voltage of 15-20 kV at a working distance of 15-20 cm. The fiber membranes were then heat treated under vacuum at 70 °C for 24 hours to cross-link the PU. The fiber diameters ranged from 100 to 400 nm.

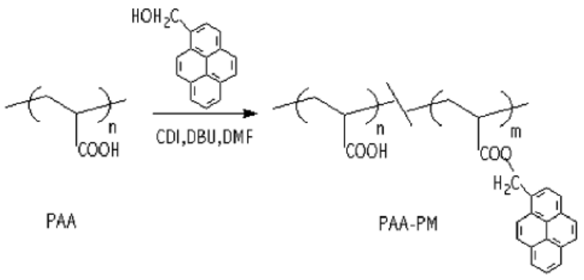

Figure 1.18. Synthetic scheme for PAA-PM. CDI is needed to perform the esterification reaction and DBU is used as a catalyst. Reproduced with permission[75]. Copyright the American Chemical Society, 2002.

Using this material, the electron-poor analytes Fe^{3+}, Hg^{2+}, and DNT were detected via the static quenching of the electron-rich PM moiety in water. By covalently linking the dye to the PAA self-quenching effects are reduced, according to the authors. The fluorescence quenching Stern-Volmer coefficients obtained from the electrospun fiber membranes are roughly 2 to 3 orders of magnitude higher for each analyte tested compared to films of similar polymer/dye composition.[76] The spatial resolution in K_{sv} between analytes is also slightly improved in the electrospun fibers.

These PAA-PM fibers exhibit higher sensitivity and slightly improved selectivity over film based sensors; but the selectivity may not be high enough for certain applications. Other untested electron rich analytes may have similar values for K_{sv} thus reducing the overall selectivity for use in a practical field, as aqueous environments may have a wide variety of cationic analytes that could be present. While other cationic species were tested in the authors study from reference 12, the polymer/dye composition is slightly different than that presented in this study and may not be a good direct comparison. Furthermore, response times were not measured for these sensors. This is an important aspect for this sensor as the sensing mechanism is based static quenching.

Kim and co-workers[77,78,79] have recently developed an organic solvent sensor from PDA embedded PEO or PMMA electrospun fibers. DA monomers were blended into either PEO or PMMA solutions with tetraethyl orthosilicate (TEOS, which was used to stabilize the fibers via cross-linking) and electrospun into fibers. Upon exposure to UV light, domains of self-assembled DA monomers photo-polymerize into PDAs as evident by the blue color change seen in the fiber mats (Figure 1.19).

After heating PDAs made from monomers of 10,12-pentacosadiynoic acid-aminobutyric acid (PCDA-ABA) and 10,12-pentacosadiynoic acid-aniline (PCDA-AN) to 100 °C the fiber mats changed color from blue to red. After cooling the mats back down to room temperature the PCDA-ABA embedded fibers reverted back to the original blue color while the PCDA-AN embedded fibers stayed a red color (Figure 7d). It was also shown that fibers made with purely PCDA-ABA had no response to solvents, while PCDA-AN containing fibers turned from blue to red in the presents of most of the solvents (Figure 7c). These observations lead the authors to believe that a mixture of the two monomers could potential lead to different colorimetric responses to different solvents. The results from mixing PCDA-ABA and PCDA-AN together are shown in Figure 1.20.

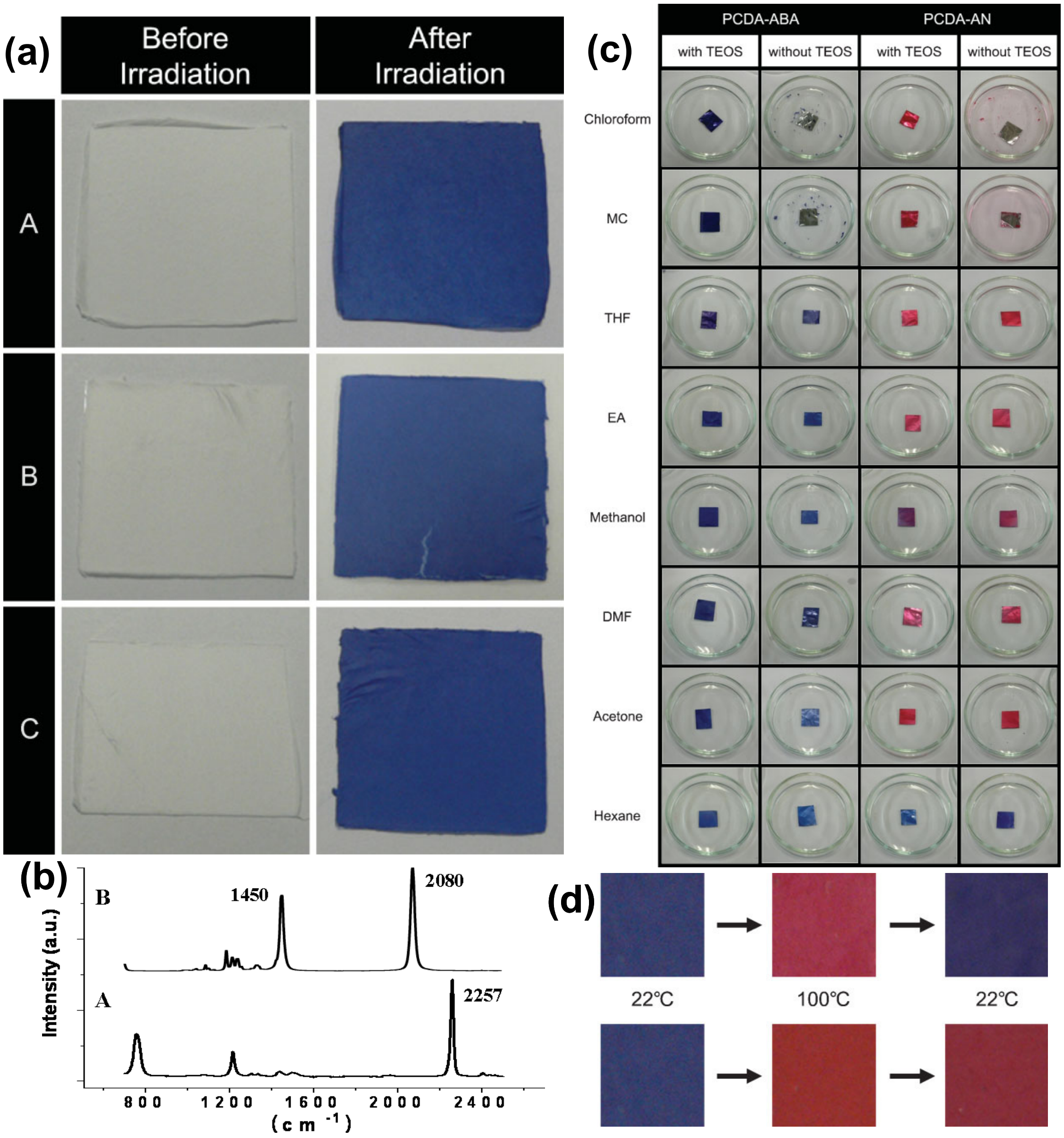

Figure 1.19**.** (a) Electrospun fiber mats with A) PCDA-ABA, B) PCDA-AN, and C) 1:1 ratio of the two PDA monomers before and after UV irradiation, (b) Raman spectra of (A) PCDA in chloroform and (B) PCDA embedded fibers after exposure to UV light for 3 minutes, (c) colorimetric response to solvents for fibers with either PCDA-ABA or PCDA-AN polymerized monomers both without and with the addition of TEOS, and (d) colorimetric response to heat for PCDA-ABA (top) and PCDA-AN (bottom) polymerized fibers mats. Reproduced with permission[77,79]. Copyright Wiley-VCH, 2007 and 2009.

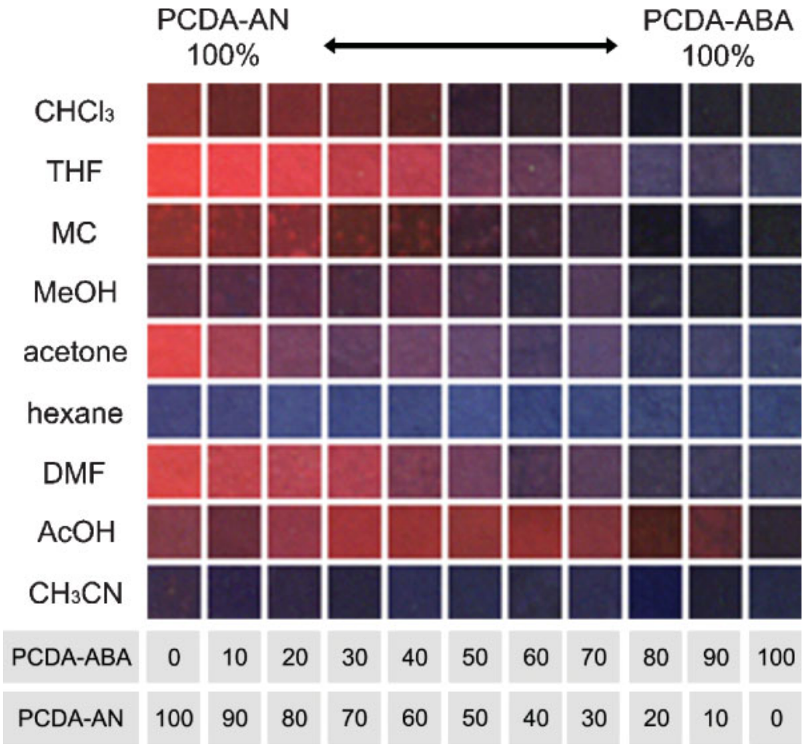

Figure 1.20**.** Colorimetric responds to solvent at room temperature to photo-polymerized mixtures of the PCDA-ABA and PCDA-AN embedded fiber mats. All fibers mats are exposed to the solvent for 30 seconds and the initial color of each fiber mat is blue. Reproduced with permission[77]. Copyright Wiley-VCH, 2009.

The idea of photo-polymerizing multiple DA monomers within an electrospun fiber membrane for use as a colorimetric based sensors is an intriguing idea. However, there are still issues that need to be addresses for this type of sensor. While there seems to be some trends in response to certain types of solvents (for example, the chlorinated solvents in Figure 1.20), it is very difficult to differentiate between the different shades of blue and red by eye for each solvent throughout the range of monomer content, if not impossible. For these fibers to be incorporated into a device platform either the selectivity needs to be increased or the fibers would need to be analyzed by a computer. The sensitivity may also be an issue with this sensor, as only pure solvent was tested to activate color changes. Diluted solvents were also not tested.

1.4.4 Energy

The following sections (1.4.4, 1.4.5, and 1.4.6) will overview the use of electrospun fibers in energy, electronic, and environmental applications. These applications areas for electrospun fibers are less developed than the previously mentioned sections (see Figure 1.12). The lack of depth in these areas is one motivating factor for the work in this thesis. In terms of energy applications, the bulk of the electrospinning literature deals with battery electrodes or electrodes for dye-sensitized solar cells. As such, selected studies on these topics will be review in this section. Work in bulk heterojunction organic photovoltaics has been performed for this thesis and is reported in Chapter 2.[50]

There is a growing needed for miniaturized energy storage systems for state of the art microelectronics and microdevices.[80] Metal oxide nanofibers have thus been receiving attention for use in microbatteries. Using electrospinning, Chen and co-workers[81] obtained $LiCoO_2$ fibers by electrospinning a viscous sol containing lithium acetate and cobalt acetate which were subsequently fired to form the inorganic fibers. $LiCoO_2$ fibers exhibited higher capacity than $LiCoO_2$ powders of similar size over 20 charge/discharge cycles (180 mA·h/g compared to 130 mA·h/g), after which both fibers and powders converged to a capacity of ~ mA·h/g. Both the initially higher capacity and the subsequent faster decay for the fibers were attributed to the increased surface area and anisotropic morphology. This would allow for shorter Li^+ diffusion lengths, but would also increase the likelihood of impurity formation with the electrolyte. In a follow-up publication, Chen and co-workers[80] used coaxial electrospinning to create a thin MgO shell around the $LiCoO_2$ using a magnesium acetate sheath solution. The core-shell electrodes were found only a 10% decrease in capacity over 40 cycles, while the $LiCoO_2$ decrease by ~50% (Figure 1.21).

Inorganic nanofibers made by electrospinning have been investigated for use as electrodes and photo-activated materials in dye-sensitized solar cells (DSSCs). A DSSC consist of an anode (typically a transparent and conductive metal oxide), a cathode (typically platinum), a photo-activated material (typically Ru-dye adsorbed metal oxide nanoparticles) and an electrolyte (typically the I^-/I_3^- redox couple). As light is absorbed by the photo-activated material a photoelectron is generated and injected into the anode. The oxidized photo-activated material takes an electron from the electrolyte which is replenished cathode, completing the circuit.

Electrospun metal oxide based fibers have been used as photo-activated materials in DSSCs in hopes to improve charge transport. Charge transport in a network of nanoparticles requires charge hopping across neighboring nanoparticles. Ideally this could be negated in crystalline anisotropic fibers. However, device efficiencies using TiO_2 and ZnO nanofibers from electrospinning are rather low.[82,83] Mukherjee and co-workers[82] determined that low device efficiency using titania nanofibers was due to a large number of surface electron traps in the fibers. TEM analysis shown that the titania fibers were polycrystalline and were comprised of ~10 nm crystallites. Thus electron transport would idealistically not be any better than nanoparticle based DSSC. Qiao and co-workers[84] constructed a DSSC with an electrospun carbon fiber cathode as a low-cost alternative to Pt. Carbon nanofibers were obtained by pyrolyzing electrospun poly(actrylonitrile) (PAN) fibers at 1200 °C in argon. The carbon nanofiber based DSSC had a similar open-circuit voltage (V_{oc}) and short-circuit current density (J_{sc}) than DSSC with a Pt electrode, but had a reduced fill factor and thus a reduced efficiency

(5.5% vs. 6.97%). The reduced fill factor was attributed to a higher series resistance in the carbon nanofibers compared to the Pt thin film. The authors state that with further optimization of thickness and porosity of the electrospun carbon nanofibers layer that a smaller series resistance could be obtainable. Nevertheless, decrease in efficiency may economically passable given the comparative cost in platinum.

1.4.5 Electronic

Electrospun fibers have found many uses in electronic applications. The most popular reports in the literature are on electrospun fiber based field-effect transistors (FET). Different reports by Pinto and co-workers have shown the feasibility of a nanofiber based FET from both polyaniline/polyethylene oxide (PANi/PEO) fiber blends[85] and poly(3-hexylthiophene) (P3HT) fibers.[86] Both FETs were made by passing patterned Si/SiO_2 wafers between the tip and collector. In the case of the PANi/PEO based system, saturation currents of the FET were seen at low $V_{S\text{-}D}$ (~ -1 V). FET behavior was also seen in the P3HT based system, but very low saturation currents (1-2 nA) were seen at much high $V_{S\text{-}D}$ values, typically around -80 V. The authors contribute the poor FET characteristics to P3HT degradation by O_2, amongst other things. More recently, a P3HT based FET was made on flexible plastic substrates using ion gel-gated configuration.[87] The ionic liquid based gel facilitated high on-current and low voltage operation and also protected the environmentally sensitive P3HT fibers. At 2 V and current of ~600 μA could be obtained. Bio-driven photo-detector work will be reported on in Chapter 3.[88]

1.4.6 Environmental

The demand for safe, reusable drinking water is ever-increasing given the significant reduction of such water sources. Complete water purification has proven to be difficult via traditional techniques largely due to a wide variety of organic and inorganic contaminants. Catalytic degradation of contaminates using nanoparticle or molecular species is one potential route for water remediation. However, given the associated small size scales, these materials are difficult to efficiently collect for water purification systems. As such, immobilization of denomination materials onto a non-reactive substrate is required. Simple immobilization onto conventional low surface area substrates, however, effectively reduce the available surface area of the catalyst, limiting the rate at which pollutants can be removed. Immobilization of catalytic species onto electrospun fibers is one method that could potentially be used to effectively treat contaminated water, as high surface area of the catalysis is maintained. There are only a handful of papers investigating the use of electrospun fiber based catalysis for water decontamination outside of the studies presented in Chapter 4 and 5 of this thesis.[45,89]

Rutledge and co-workers created photocatalytic electrospun fibers using electrostatic layer-by-layer (LBL) depositions of titania nanoparticles (negative charge in solution) and amine-functionalized polyhedral oligosilsesquioxane (POSS) molecules (positive charge in solution) on negatively charged electrospun fiber meshes. Fibers were plasma treated to induce a negative surface charge. Using this technique, the group was able to degrade allyl alcohol under UV light[90] and bisphenol A under solar light.[91] The same group also created electrospun fibers with a LBL depositions of the polyanion poly(hydroxamic acid) (PHA) and polycation poly(*N*-vinylguanidine) (PVG) in a similar fashion.[92] PHA is a reactive polymer and was used to as a nucleophile to degrade diisopropyl fluorophosphate (DFP), a simulant for many chemical warfare agents. PVG exhibits bactericidal properties and was used to kill *E. coli* and *S. epidermidis*. It was found that the multifunctional LBL fibers were capable of degrading DFP as well as exhibit excellent bactericidal properties.

---

[1] Xia, Y.; Yang, P.; Sun, Y.; Wu, Y.; Mayers, B.; Gates, B.; Yin, Y.; Kim, F.; Yan, H. *Adv. Mater.* **2003**, *15*, 353.
[2] Shi, L.; Yu, C.; Zhou, J. *J. Phys. Chem. B*, **2005**, *109*, 22102.
[3] Chen, J.; Wiley, B. J.; Xia, Y. *Langmuir* **2007**, *23*, 4120.
[4] Shen, G.; Chen, D. *Nanoscale Res. Lett.* **2009**, *4*, 779.
[5] Gonzalez-Valls, I.; Lira-Cantu, M. *Energy Environ. Sci.* **2009**, *2*, 19.
[6] Wang, D.; Xie, T.; Li, Y. *Nano Res.* **2009**, *2*, 30.
[7] Meyyappan, M. *Prog. Cryst. Growth Charact. Mater.* **2009**, *55*, 1.
[8] Ando, Y.; Zhao, X.; Sugai, T.; Kumar, M. *Mater. Today* **2004**, *7*, 22.
[9] Palmer, L. C.; Stupp, S. I. *Acc. Chem. Res.* **2008**, *41*, 1674.
[10] Murphy, C. J.; Sau, T. K.; Gole, A.; Orendorff, C. J. *Mater. Res. Soc. Bull.* **2005**, *30*, 349.
[11] Zhou, Y.; Shimizu, T. *Chem. Mater.* **2008**, *20*, 625.
[12] Limmer S. J.; Cao, G. *Adv. Mater.* **2003**, *15*, 427.
[13] Ghicov, A.; Schmuki, P. *Chem. Commun.* **2009**, *2009*, 2791.
[14] Li, D.; Xia, Y. *Adv. Mater.* **2004**, *16*, 1151.
[15] A. Formalas, *US patent 1 975 504,* 1934.
[16] Baumgarten, P. K. *J Colloid. Interface Sci*. **1971**, *36*, 71.
[17] Larrondo, L.; St. John Manley, R. *J. Polym. Sci Polym. Phys. Ed.* **1981**, *19*, 909.
[18] Larrondo, L.; St. John Manley, R. *J. Polym. Sci Polym. Phys. Ed.* **1981**, *19*, 921.
[19] Larrondo, L.; St. John Manley, R *J. Polym. Sci Polym. Phys. Ed.* **1981**, *19*, 933.
[20] Doshi, J.; Reneker, D. H. *J. Electrostat.* **1995**, *35*, 151.
[21] Srinivasan, G.; Reneker, D. H. *Polym. Int.* **1995**, *36*, 195.
[22] Reneker, D. H.; Chun I. *Nanotechnol.* **1996**, *7*, 216.
[23] Fang, X.; Reneker, D. H. *J. Macromol Sci* **1997**, *B36*, 169.
[24] Shenoy, S. L.; Bates, W. D.; Frisch, H. L.; Wnek, G. E. *Polymer* **2005**, *46*, 3372.
[25] Megelsko, S.; Stephens, J. S.; Chase, D. B.; Rabolt, J. F. *Macromolecules* **2002**, *35*, 8456.
[26] P. Gupta, C. Elkins, T. E. Long, G. L. Wilkes, *Polymer* **2005**, *46*, 4799.
[27] Koshi, A.; Yim, K.; Shivkumar, S. *Mater. Lett.* **2004**, *58*, 493.
[28] Dai, X.; Shivkumar, S. *J. Am. Ceram. Soc.* **2007**, *90*, 1412.
[29] Eda, G.; Liu, J.; Shivkumar, S. *Mater. Lett.* **2007**, *61*, 1451.
[30] Zuo, W.; Zhu, M.; Yang, W.; Yu, H.; Chen, Y.; Zhang, Y. *Polym. Eng. Sci.* **2005**, *45*, 704.
[31] Deitzel, J. M.; Kleinmeyer, J.; Harris, D.; Tan, N. C. B. *Polymer* **2001**, *42*, 261.
[32] Mo, X. M.; Xu, C. Y.; Kotaki, M.; Ramakrishna, S. *Biomaterials* **2004**, *25*, 1883.
[33] Zhang, C.; Yuan, X.; Wu, L.; Han, Y.; Sheng, J. *Eur. Polym. J.* **2005**, *41*, 423.
[34] Eda, Goki; Liu, J.; Shivkumar, S. *Eur. Polym. J.* **2007**, *43*, 1154.
[35] Uyar, T.; Besenbacher, F. *Polymer* **2008**, *48*, 5336.
[36] Arayanarakul, K.; Choktaweesap, N.; Aht-ong, Duangdao; Meechaisue, C.; Supaphol, P. *Macrmol. Mater. Eng.* **2006**, *291*, 581.
[37] Fallahi, D.; Rafizadeh, M.; Mohammadi, N.; Vahidi, B. *e-Polymers* **2008** 056.
[38] Lin, T.; Wang, H.; Wang, H.; Wang, X. *Nanotechnology*, **2004**, *15*, 1375.
[39] Tripatanasuwan, S.; Zhong, Z.; Reneker, D. H. *Polymer* , **2007**, *48*, 5742.
[40] Hardick, O.; Stevens, B.; Bracewell, D. G. *J. Mater. Sci.* **2011**, *46*, 3890.
[41] Casper, C. L.; Stephens, J. S.; Tassil, N. G.; Chase, D. B. Rabolt, J. F. *Macromolecules* **2004**, *37*, 573.
[42] Gupta, B. S.; Moghe, A. K. *Polym. Rev.* **2008**, *48*, 353.
[43] Li, D.; Xia, Y. *Nano Lett.* **2004**, *4*, 933.
[44] Wang, M.; Jing, N.; Su, C. B.; Kameoka, J.; Chou, C.-K.; Hung, M.-C.; Chang, K.-A. *Appl. Phys. Lett.***2006**, *88*, 033106.
[45] Bedford, N. M.; Steckl, A. J. *ACS Appl. Mater. Interfaces* **2010**, *2*, 2448.
[46] Han, D.; Steckl, A. J. *Langmuir* **2009**, *25*, 9454.

---

[47] Muthiah, P.; Hsu, S.-H.; Sigmund, W. *Langmuir*, **2010**, *26*, 12483.

[48] Sharma, N.; Jaffari, G. H.; Shah, S. I.; Pochan, D. J. *Nanotechnology* **2010**, *21*, 085707.

[49] Song, T.; Zhang, Y.; Zhou, T.; Lim, C. T.; Ramakrishna, S.; Liu, B. *Chem. Phys. Lett.* **2005**, *415*, 317.

[50] Bedford, N. M.; Dickerson, M. B.; Drummy, L. F.; Koerner, H.; Singh, K. M. Durstock, M. F.; Naik, R. R.; Steckl, A. J. *Small* **2011**, submitted.

[51] Kameoka, J.; Craighead, H. G. *App. Phys. Lett.*, **2003**, *83*, 371.

[52] Li, D.; Wang, Y.; Xia, Y. *Adv. Mater.*, **2004**, *16(4)*, 361.

[53] Li, D.; Wang, Y.; Xia, Y. *Nano Lett.*, **2003**, *3(8)*, 1167.

[54] Sun, D.; Chang, C.; Li, S.; Lin, L. *Nano Lett.*, **2006**, *6(4)*, 839.

[55] Chang, C.; Limkrailassiri, K.; Lin, L. *App. Phys. Lett.*, **2008**, *93*, 123111.

[56] Chang, C.; Tran, V. H.; Wang, J.; Fuh, Y.-K.; Lin, L. *NanoLett*. **2010**, *10*, 726.

[57] Xie, J.; Li, X.; Xia, Y. *Macromol. Rapid Comm.* **2008**, *29*, 1775.

[58] Boland, E. D.; Wnek, G. E.; Simpson, D. G.; Pawlowski, K. J.; Bowlin, G. L. *J. Macrmol. Sci. Pure Appl. Chem.* **2001**, *A38*, 1231.

[59] Matthews, J. A.; Wnek, G. E.; Simpson, D. G.; Bowlin, G. L. *Biomacromolecules* **2002**, *3*, 232.

[60] Wnek, G. E.; Carr, M. E.; Simpson, D. G.; *Nano Lett.* **2003**, *3*, 213.

[61] Li, W.J.; Laurencin, C. T.; Caterson, E. J.; Tua, R. S.; Ko, F. K.; *J. Biomed. Mater. Res.* **2002**, *60*, 613.

[62] Bhattarai, S. R.; Bhattarai, N.; Yi, H. K.; Hwang, P. H.; Cha, D. I.; Kim, H. Y. *Biomaterials* **2004**, *25*, 2595.

[63] Zhao, P.; Jiang, H.; Pan, H.; Zhu, K.; Chen, W. *J. Biomed. Mater. Res. Part A*, **2007**, *83*, 372.

[64] Yang, F.; Murugan, R.; Wang, S.; Ramakrishna, S. *Biomaterials*, **2005**, *26*, 2603.

[65] Chew, S. Y.; Mi, R.; Hoke, A.; Leong, K. W. *Adv. Funct. Mater.*, **2007**, *17*, 1288.

[66] Choi, J. S.; Lee, S. J.; Christ, G. J.; Atala, A.; Yoo, J. Y. *Biomaterials*, **2008**, *29*, 2899.

[67] Fu, Y.-C.; Nie, H.; Ho, M.-L.; Wang, C.-K. Wang, C.-H. *Biotech. Bioeng.*, **2008**, *99*, 96.

[68] Kenawy, E.-R.; Bowlin, G. L.; Mansfield, K.; Layman, J.; Simpson, D. G.; Sanders, E. H.; Wnek, G. E. *J. Controlled Release*, **2002**, *81*, 57.

[69] Luu, Y. K.; Kim, K.; Hsiao, B. S.; Chu, B.; Hadjiargyrou, M. *J. Controlled Release*, **2003**, *89*, 341.

[70] Qin, X-H.; Wang, S.-Y. *J. Appl. Polym. Sci*. **2006**, *102*, 1285

[71] Park, H.-S.; Park, Y. O. *Korean J. Chem. Eng.***2005**, *22*, 165.

[72] Heikkilä, P.; Taipale, A.; Lehtimäki, Harlin, A. *Polym. Eng. Sci.* **2008**, *48*, 1168.

[73] Liu, H.; Kameoka, J.; Czaplewski, D. A.; Craighead, H. G. *Nano Lett.* **2004**, *4*, 671.

[74] Matsuguchi, M.; Io, J.; Sugiyama, G.; Sakai, Y. *Synth. Met.*

[75] Wang, X.; Drew, C.; Lee, S.-H.; Senecal, K. J.; Kumar, J.; Samuelson, L. A. *Nano Lett.* **2002**, *2*, 1273.

[76] Lee, S.-H.; Kumar, J.; Tripathy, S. K. *Langmuir* **2000**, *16*, 10482.

[77] Yoon, J.; Jung, Y.-S.; Kim, J.-M. *Adv. Funct. Mater.* **2009**, *19*, 209

[78] Yoon, J.; Chae, S. K.; and Kim, J.-M. *J. Amer. Chem. Soc.* **2007**, *129*, 3038.

[79] Chae, S.-K.; Park, H.; Yoon, J.; Lee, C. H.; Ahn, D. J.; Kim, J.-M. *Adv. Mater.* **2007**, *19*, 521.

[80] Gu, Y.; Chen, D.; Jiao, X.; Liu, F. *J. Mater. Chem.* **2007**, *17*, 1769.

[81] Gu, Y.; Chen, D.; Jiao, X. *J. Phys. Chem. B* **2005**, *109*, 17901.

[82] Mukherjee, K.; Teng, T.-H.; Jose, R.; Ramakrishna, S. *Appl. Phys. Lett.* **2009**, *95*, 012101.

[83] Kim, I-D.; Hong, J.-M.; Lee, B. H.; Kim, D. Y.; Jeon, E.-K.; Choi, D.-K.; Yang, D.-J. *Appl. Phys. Lett.* **2007**, *91*, 163109

[84] Joshi, P.; Zhang, L.; Chen, Q.; Galipeau, D.; Fong, H.; Qiao, Q. *ACS Appl. Mater. Interfaces* **2010**, *2*, 3577.

[85] Pinto, N. J.; Johnson Jr., A. T.; MacDiarmid, A. G.; Mueller, C. H.; Theofylaktos, N.; Robinson, D. C.; Miranda, F. A. *App. Phys. Lett.*, **2003**, *83(20)*, 4224.

[86] Gonzalez, R.; Pinto, N. J. *Synthetic Metals*, **2005**, *151*, 275.

[87] Lee, S. W.; Lee, H. J.; Choi, J. H.; Koh, W. G.; Myoung, J. M.; Hur, J. H.; Park, J. J.; Cho, J. H.; Jeong, U. *Nano Lett.* **2010**, *10*, 347.

---

[88] Bedford, N. M.; Winget, G. D.; Punnamaraju, S.; Steckl, A. J. *Biomacromolecules* **2011**, *12*, 778.

[89] Bedford, N. M.; Pelaez, M.; Han, C.; Dionysiou, D. D.; Steckl, A. J. *Ener. Environ. Sci.* **2011**, submitted.

[90] Lee, J. A.; Krogman, K. C.; Ma, M.; Hill, R. M.; Hammond, P. T.; Rutledge, G. C. *Adv. Mater.* **2009**, *21*, 1252.

[91] Lee, J. A.; Nam, Y. S.; Rutledge, G. C.; Hammond, P. T. *Adv. Funct. Mater.* **2010**, *20*, 2424.

[92] Chen. L.; Bromberg, L.; Lee, J. A.; Zhang, H.; Schreuder-Gibson, H.; Gibson, P.; Walker, J.; Hammond, P. T.; Hatton, T. A.; Rutledge, G. C. *Chem. Mater.* **2010**, *22*, 1429.

Chapter 2:
Nanofiber-Based Bulk-Heterojunction Organic Solar Cells Using Coaxial Electrospinning[1]

2.1 Introduction

Bulk heterojunction organic photovoltaic (BHJ-OPV) devices have been the topic of ever increasing research due to their potential to result in printable, inexpensive solar cells which can be processed onto flexible substrates.[2,3,4] Typically, the active layer of the BHJ consists of an interpenetrating network of electron-donating conjugated polymers and electron-accepting fullerenes. One of the most studied BHJ-OPV systems consists of a mixture of poly(3-hexylthiophene) (P3HT) and [6,6]-phenyl-C_{61}-butyric acid methyl ester (PCBM).[2,5] It is widely accepted that for BHJ-OPV devices to be economically viable power conversion efficiencies (PCE) need to reach 10%.[4,6] The highest PCE values obtained for P3HT:PCBM devices have been in the 4-5% range,[7,8,9] lower than the value needed to become competitive with silicon-based solar cells for commercial applications.

In order to increase the PCEs of BHJ-OPV devices many different routes are currently being explored in the scientific community. One option is to use a different materials system wherein the donor/acceptor pair exhibits improved transport properties, absorbs a larger portion of the solar spectrum, and/or has a band gap arrangement which improves device efficiency compared to the P3HT:PCBM system.[10,11,12,13,14,15,16,17] Another route is to use a tandem cell architecture, in which two different and separate active layers absorb different portions of the solar spectrum.[18,19,20,21] Fine-tuning the morphology of the BHJ is also important. A high efficiency device requires a balance between a high interfacial area of donor and acceptor moieties while maintaining large enough domain sizes for charge transport to the appropriate electrodes with minimum charge recombination. Typically, this is accomplished by thermal annealing[7,22,23,24] or solvent annealing.[8,25,26,27] More recently other techniques, such as the use of processing additives and preformed nanofibers, have been developed to control the electron donor/electron acceptor morphology and molecular ordering.[4] Processing additives are used to more strongly solubilize one component of the mixture and generally have a higher boiling point than the bulk solvent, resulting in increased phase separation and thus improved device performance.[28,29,30,31,32] Preformed polymer nanofibers, made by using thermally-driven solution processing techniques, have been shown to have increased crystallinity, increased hole mobility, and absorption at longer wavelengths when compared to films made via spin coating.[33,34,35,36] The inclusion of preformed nanofibers into the active layer of the BHJ increases device efficiency and can be used to better control active layer morphology and is thus an attractive methodology for improving BHJ-OPV devices.

Electrospinning is a well-established and straightforward technique to create polymer fibers from a wide variety of materials with diameters ranging from tens of nanometers to several microns.[37,38,39] This continuous process can allow for the production of an entangled, three-dimensional non-woven fiber network exhibiting a high density of fully interconnected pores throughout the material which yields a very high surface area to volume ratio. This coupled with the ability to generate fibers from a large variety of materials, control fiber morphology, and create multi-component fibers with relative ease have contributed to the increased application of electrospinning over solution processing techniques for creating nanofibers in recent years. High throughput industrial scale electrospinning is now achievable,[40,41,42,43,44] further extending the use of electrospun fibers in real-world applications. Application areas for electrospinning are widely varied and include (but are not limited to) biomedical,[45,46] photonics,[47,48] catalyst,[49,50] energy storage,[51,52] energy harvesting,[53,54] and filtration.[55,56]

In this study the use and incorporation of preformed P3HT:PCBM nanofibers produced by coaxial electrospinning,[57,58] is examined for BHJ-OPV devices. Previously P3HT fibers have been made using various electrospinning techniques for field-effect transistor,[59,60,61] sensor,[62] and nanoelectronic[63,64] applications. However, these previous methods are inappropriate for implementation in the production of OPVs. The P3HT either needs to be mixed with a high molecular weight coil-like insulating polymer that can be electrospun into uniform fibers or electrospun at fairly high concentration to obtain fibers. The resulting fibers are often too large (larger than 1 μm) to be useful in OPV devices. Furthermore, adding PCBM to these optimized electrospinning protocols leads to poor fiber formation (based on our observations). Recently, Sundarrajan et al.[65] used coaxial electrospinning to entrap a core phase of P3HT:PCBM in poly(vinyl pyrrolidone) (PVP). After the removal of PVP, micron sized fibers of P3HT:PCBM were obtained. While a novel process, the resulting non-woven matrix of P3HT:PCBM fibers yielded a power conversion efficiency (PCE) of 8.7×10^{-8}, a value severely lower than needed to be useful in PV applications. In the current study, poly(caprolactone) (PCL) is used as the sacrificial sheath and the driving force for fiber formation. P3HT:PCBM fibers are obtained by inserting a relatively low concentration solution of P3HT:PCBM into the core of a charged PCL liquid jet via a concentric nozzle. The coaxial fibers were then selectively stripped of the PCL sheath, yielding pure P3HT:PCBM fibers. The resulting structurally ordered fibers of P3HT:PCBM are then incorporated into a typical active layer of a BHJ-OPV by depositing a fully solubilized P3HT:PCBM layer on top. While partial dissolution of the fibers does occur, the remaining electrospun material maintains structural coherence and acts as a template for the fully solubilized P3HT. As the mechanism of electrospun fiber formation is largely independent of the core solution, this method can potentially be used to create nanofibers from other electron donor/electron acceptor pairs and lead to improved device characteristics for those systems.

2.2 Experimental

2.2.1 Electrospinning

Coaxial electrospinning was performed using a concentric stainless steel nozzle (Nisco Engineering) with an outer diameter of 0.8 mm and an inner diameter of 0.35 mm. Sheath solutions of poly(caprolactone) (PCL, M_w = 80 kDa, Sigma) were made in 60/40 (v/v) chloroform/dimethylformamide (DMF) at a concentration of 14 wt%, while core solutions of poly(3-hexylthiophene) (P3HT, M_w = 45 kDa, American Dye Source)-phenyl-C_{61}-butyric acid methyl ester (PCBM, American Dye Source) were made in chloroform at 1 wt% and 0.6 wt%, respectively. A voltage of 20 kV was applied from the coaxial nozzle to the collecting electrode using a Gamma High Voltage ES-30 power supply. The spinneret tip to substrate distance was set to 25 cm and flow rates for the core and sheath solutions were 1.25 mL/h and 6.5 mL/h, respectively. All electrospinning experiments were performed in ambient conditions.

2.2.2 Fiber Processing

The as-electrospun core-sheath fibers were placed in cyclopentanone (99+%, Acros) in order to selectively dissolve away the PCL component from the fibers. The resulting dispersion was centrifuged (13,000 × g, 10 min) to pellet the P3HT:PCBM fibers and to remove the dissolved PCL. This process was repeated six additional times in order to fully wash the PCL from the P3HT:PCBM fibers. The fully washed fibers were re-dispersed in cyclopentanone to form a stable suspension for spin coating onto device substrates.

2.2.3 Device Fabrication

Indium tin oxide (ITO, Colorado Concept Coatings, LLC) coated glass was selectively etched using concentrated HCl. The substrates were thoroughly cleaned with detergent, water, hexanes, isopropanol, methanol, and acetone. Poly(3,4-ethylenedioxythiophene):poly(styrene sulfonate) (PEDOT:PSS, Clevios-P® purchased from H. C. Starck) was filtered with a 5 µm syringe filter, deposited using spin coating and dried at 165 °C for 20 min. When appropriate, electrospun P3HT:PCBM fibers were deposited from a cyclopentanone dispersion by spin coating. A solution of P3HT:PCBM (15 mg/mL and 9 mg/mL in chlorobenzene, respectively) was used to interconnect the fibers and was deposited using spin coating after filtration with a 0.45 µm syringe filter. This solution was heated to 60 °C prior to spin coating. When appropriate, the devices were annealed at 160 °C for 10 minutes. The resulting active layers were all ~100 nm in thickness. Aluminum electrodes were evaporated onto the substrate at a thickness of ~100 nm. The active surface area of the device was 0.16 cm^2. Spin coating of solubilized P3HT:PCBM layer, device annealing, and electrode evaporation were performed in a glove box under dry N_2.

2.2.4 Characterization

Current-voltage characteristics were obtained with a Keithley 237 High Voltage Source under AM1.5 solar radiation at a power density of 100 mW/cm^2 using a Newport Oriel Full Spectrum Solar Simulator under N_2. Fiber morphologies were studied using a FEI/Phillips XL30 field-emission environmental scanning electron microscope (FE-ESEM) and Philips CM-200 transmission electron microscope (TEM). UV-visible absorption spectra were obtained using a Perkin Elmer Lambda 900 UV/Vis/NIR spectrometer. P3HT:PCBM surface phase separation was studied with atomic force microscopy (AFM) using a Veeco Dimension 3100 Scanning Probe Microscope equipped with a NanoScope V controller and operated in Tapping Mode. Electron diffraction experiments were performed using Philips CM-200 TEM. Active layers were removed from device substrates by slowly dipping the devices in water to remove the PEDOT:PSS under-layer. Fragments of the P3HT:PCBM active layers were then collected on copper TEM grids. Synchrotron experiments were carried out at the small (wide) angle x-ray scattering (SAXS/WAXS) beamline 7.3.3 of the Advanced Light Source at Lawrence Berkeley National Laboratory at 10keV (1.24Å) from a bend magnet and focused via a Mo/B4C double multilayer monochromator. SAXS and WAXS were carried out simultaneously using high speed Dectris Pilatus 100k and Dectris Pilatus 1M detectors. Time-resolved experiments were performed at 10Hz frame collection. 2D images were reduced using Nika macros for Igor Pro.[66] Images were corrected for transmission, background, and initial beam intensity fluctuations. For in-situ annealing experiments, samples were sealed in a custom-made heating chamber provided by Dr. Alexander Hexamer of Berkeley Lab's Advanced Light Source. The chamber consisted of a hot plate (with remote temperature control) an inlet to purge the chamber with He to prevent rapid oxidation of the BHJ material and to reduce air scattering and kapton windows to allow for x-rays to pass. The temperature was ramped for 25 °C to 160 °C at a rate of ~13.5 °C/min, held at 106 °C for 10 min, then cooled back to 25 °C at a cooling rate of ~ 14 °C/min. GIXD experiments were taken consecutively at 2 min intervals over a total of 30 min.

2.3 Results and Discussion

Coaxial electrospinning is used to create P3HT:PCBM-PCL core-sheath fibers, which are subsequently stripped of the PCL sheath layer and embedded within the active layer of a BHJ-OPV. This is accomplished by first depositing a layer of P3HT:PCBM fibers onto the ITO:PEDOT electrode followed by depositing a backfill layer of fully solublized P3HT:PCBM. This was done to interconnect the fibers and to prevent the two electrodes from coming into contact due to the porous nature of the deposited fibers (see Experimental Section for details). The process is shown schematically in Fig. 2.1. For reference, the energy level diagram of this system is given in Fig. 2.2 and the device architecture is seen in Fig 2.3. The overall fiber morphology of as made coaxial fibers is shown in Fig. 2.1a. As seen in the TEM micrograph Fig. 2.1b, a uniform core-sheath structure is obtained between the PCL sheath phase and P3HT:PCBM core phase with fiber diameters as large as 1.5 μm and as low as 300 nm. The average outer fiber diameter is 650 nm ± ~500 nm, Fig. 2.1a). This moderately large size distribution is not uncommon in electrospun fibers.[67,68,69] P3HT:PCBM fibers are obtained by dissolving the PCL sheath in cyclopentanone, a solvent which does not dissolve P3HT or PCBM. The resulting P3HT:PCBM fibers are shown in Figs. 2.1c and 2.1d. The high-resolution TEM micrograph of Fig. 2.1d shows short range P3HT chain stacking (~ 10 nm in length), despite the absence of thermal annealing. It has been previously reported[37,70,71,72] that molecular stacking and ordering along the fiber direction occurs in electrospun fibers due to the intense shear forces encountered on the polymer solution during electrospinning. The P3HT:PCBM fibers have diameters of 120 ± 30 nm, but tend to arrange into 500 ± 100 nm wide fiber-like structures (Fig. 2.1c). The P3HT-PCBM fibers are approximately on the size scale of active layer film thicknesses utilized in efficient OPV devices. If instead of using the coaxial approach described above, homogenous solutions of P3HT, PCBM and PCL (or poly(ethylene oxide) -PEO) are electrospun, then nanofibers were not obtained after removal of the PCL or PEO. Instead, the removal of the insulating polymer phase resulted in either micron-sized spherical aggregates or similar sized fibers (Fig. 2.4), neither of which would be beneficial for BHJs as charge recombination dominates in thicker films.[73,74] However, it has been observed[60] that electrospinning a solution of only P3HT and PCL yields nanoscale P3HT fibers after stripping away the PCL, indicating that the addition of PCBM greatly influences the phase separation between the two polymers within the blended electrospun fibers. This highlights the advantage of coaxial electrospinning as the separation between PV and insulating materials is better controlled and the electrospinning process is largely controlled to the properties of the sheath solution.[75]

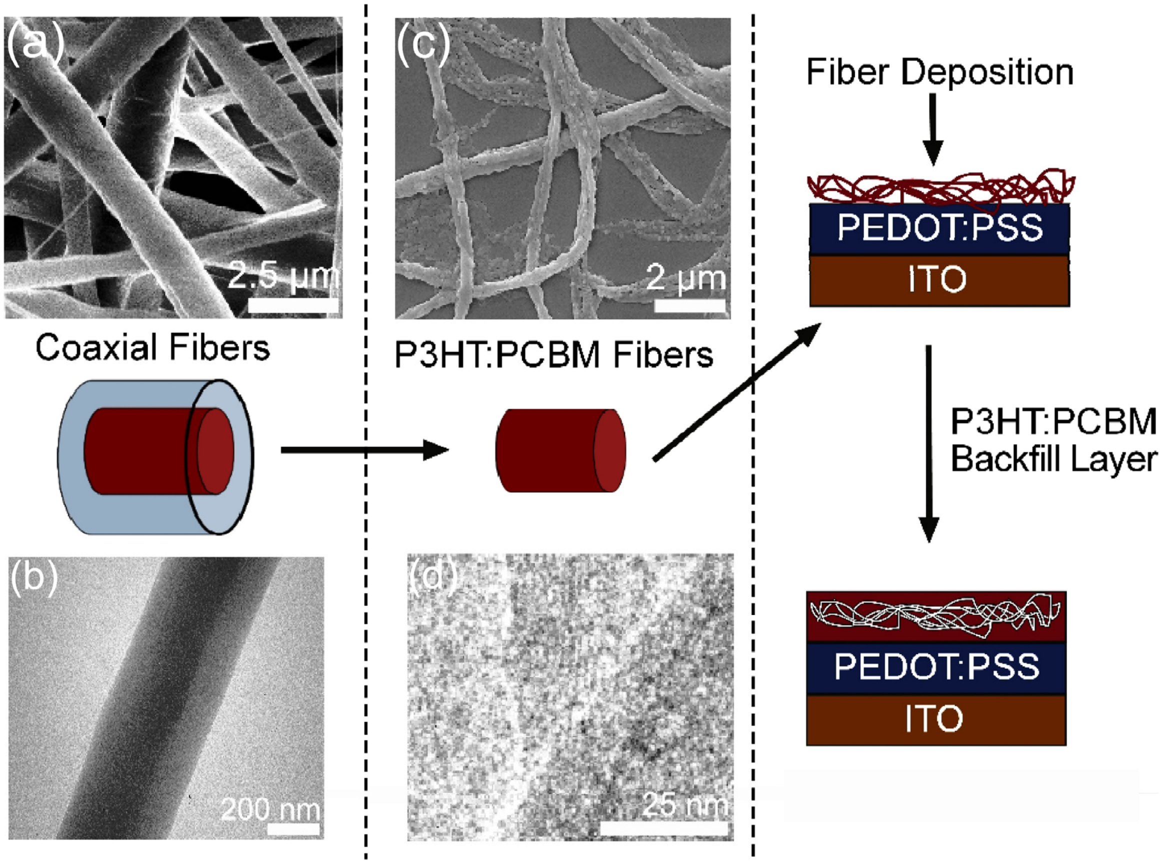

Fig. 2.1 A schematic depicting P3HT-PCBM fiber generation from the coaxial fibers and the subsequent deposition of nanofibers within the active layer of the BHJ-OPV device, along with (a) SEM micrograph and (b) TEM micrograph of P3HT:PCBM (core) – PCL (sheath) fibers (2.5 µm and 200 nm scale bars respectively), (c) SEM micrograph of P3HT:PCBM nanofibers after removal of the sheath PCL (2 µm scale bar) and, (d) high resolution TEM of the P3HT:PCBM fibers after removal of the sheath PCL (25 nm scale bar).

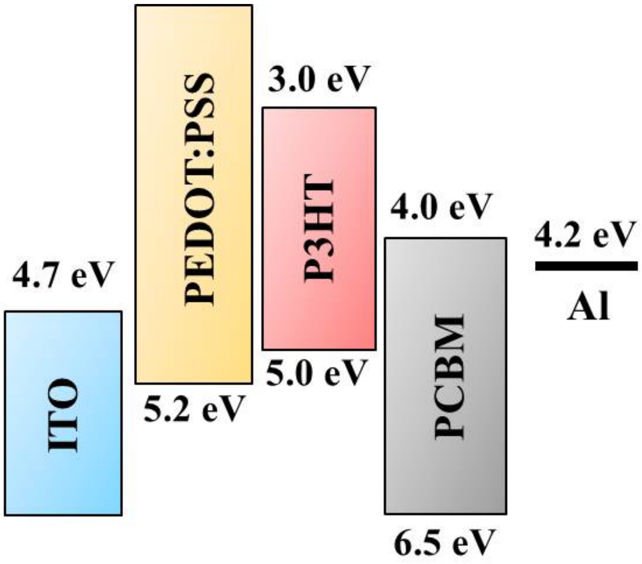

Fig. 2.2 Energy level diagram for the BJH-OPV studied in this chapter.

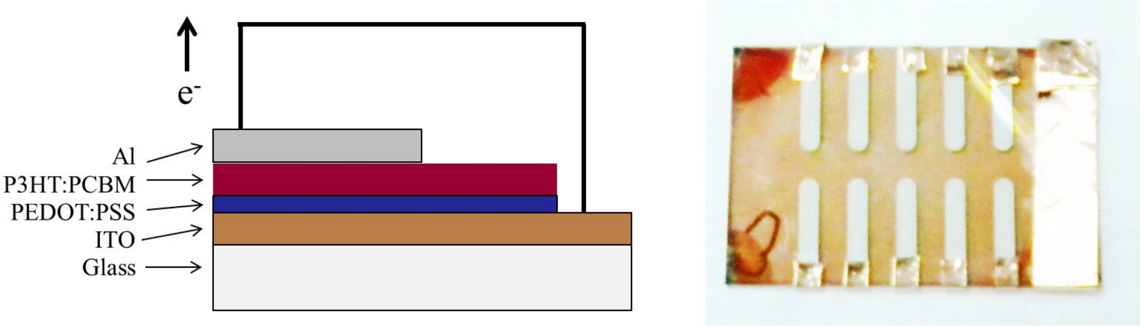

Fig. 2.3 Device architecture and device photo.

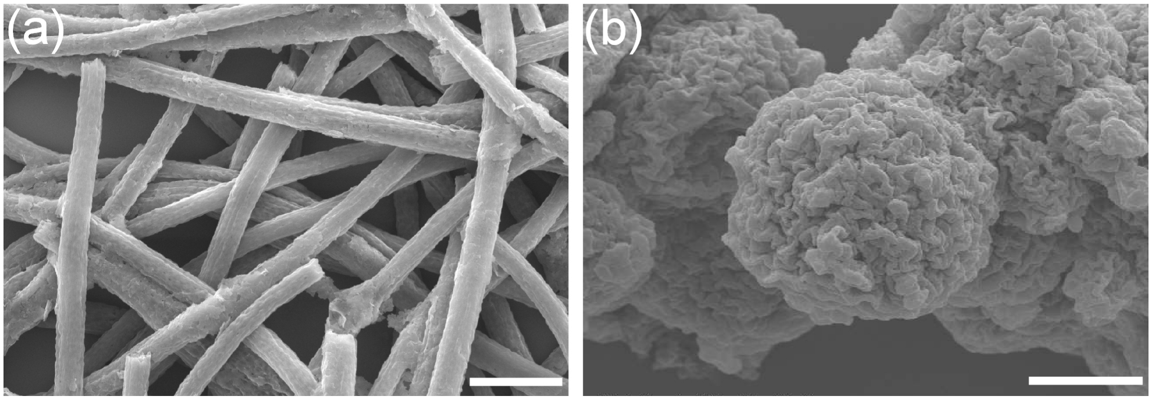

Fig. 2.4 P3HT-PCBM structures obtained by electrospinning blends of (a) 3 wt% P3HT, 2.4 wt% PCBM, 1 wt% PEO in $CHCl_3$ at 0.6 kV/cm (10 μm scale bar) and (b) 13.5 wt% PCL, 2 wt% P3HT, 1.2 wt% PCBM in $CHCl_3$ at 0.6 kV/cm (5 μm scale bar) followed by subsequent removal of the insulating polymer with acetronitrile or cyclopentanone respectively.

The pure P3HT:PCBM fibers were incorporated into the active layer of BHJ-OPV devices by spin coating from a dispersion of fibers in cyclopentanone. Next, a homogenous solution of P3HT:PCBM is deposited to completely backfill the porous fibrous network together forming a uniform active layer for the device (Fig. 2.1, schematic). While this results in partial re-dissolution of the fibers, the fibers still serve as a template for the soluble P3HT. This methodology has been previously reported[33] for OPV fabrication using solution processed fibers. Device characteristics for fiber-based and thin film devices averaged over 20 devices on at least 6 different films are presented in Table 2.1. The best performing device from each sample is given in Table 2.2, with corresponding current density-voltage curves shown in Fig. 2.5. Each sample had a film thickness of ~ 100 nm. With the inclusion of electrospun P3HT:PCBM fibers to un-annealed P3HT:PCBM layers, the short-circuit current density (J_{sc}) and fill factor (FF) both increased on average by 0.7 mA/cm^2 and 4 % respectively, resulting in a power conversion efficiency (PCE) increase from 1.6% to 2.0%. This represents a 25% increase from the un-annealed P3HT:PCBM film devices. The highest PCE achieved for the un-annealed devices was 2.3% and 2.6% for thin film and electrospun fiber based devices. After thermal annealing for 10 min at 160 °C both fiber and film devices exhibited a decrease in the open circuit voltage (V_{oc}) and increases in J_{sc}, FF, and PCE. Devices with electrospun P3HT:PCBM fibers on average had a 1.0 mA/cm^2 increase in J_{sc}, 9 % increase in FF, and 0.8 % increase in PCE compared to thin-film based annealed device. The highest PCE achieved for the annealed thin film and electrospun fiber based devices was 3.2% and 4.0% respectively. The increases in J_{sc} and FF are indicative of increased photon absorption, increased free charge generation, decreased charge recombination and/or increase in charge mobility.[3] No change in the V_{oc} was seen between fiber and film-only based devices. Device characteristics of thin film devices are consistent with those seen in the literature with the same P3HT:PCBM ratio and annealing procedure.[76,77]

Table 2.1. Average values of open-circuit voltage (V_{oc}), short-circuit current (J_{sc}), fill factor (F.F.) and power conversion efficiency (η) for each device.

Sample	V_{oc} (V)	J_{Sc} (mA/cm^2)	F.F. (%)	η (%)
P3HT:PCBM Film	0.67 ± 0.04	6.1 ± 0.5	40 ± 4	**1.6 ± 0.3**
P3HT:PCBM Film (annealed)	0.58 ± 0.02	8.7 ± 0.7	46 ± 6	**2.4 ± 0.5**

P3HT:PCBM Fibers	0.65 ± 0.03	6.8 ± 0.9	44 ± 6	**2.0 ± 0.5**
P3HT:PCBM Fibers (annealed)	**0.59 ± 0.01**	**9.7 ± 0.6**	**55 + 4**	**3.2 ± 0.4**

Table 2.2. Device characteristics of the best performing devices for each sample type.

Sample	V_{oc} (V)	J_{Sc} (mA/cm^2)	F.F. (%)	η (%)
P3HT:PCBM Film	0.64	6.7	46	**2.3**
P3HT:PCBM Film (annealed)	0.59	10.0	54	**3.2**
P3HT:PCBM Fibers	0.63	8.1	52	**2.6**
P3HT:PCBM Fibers (annealed)	**0.59**	**10.7**	**63**	**4.0**

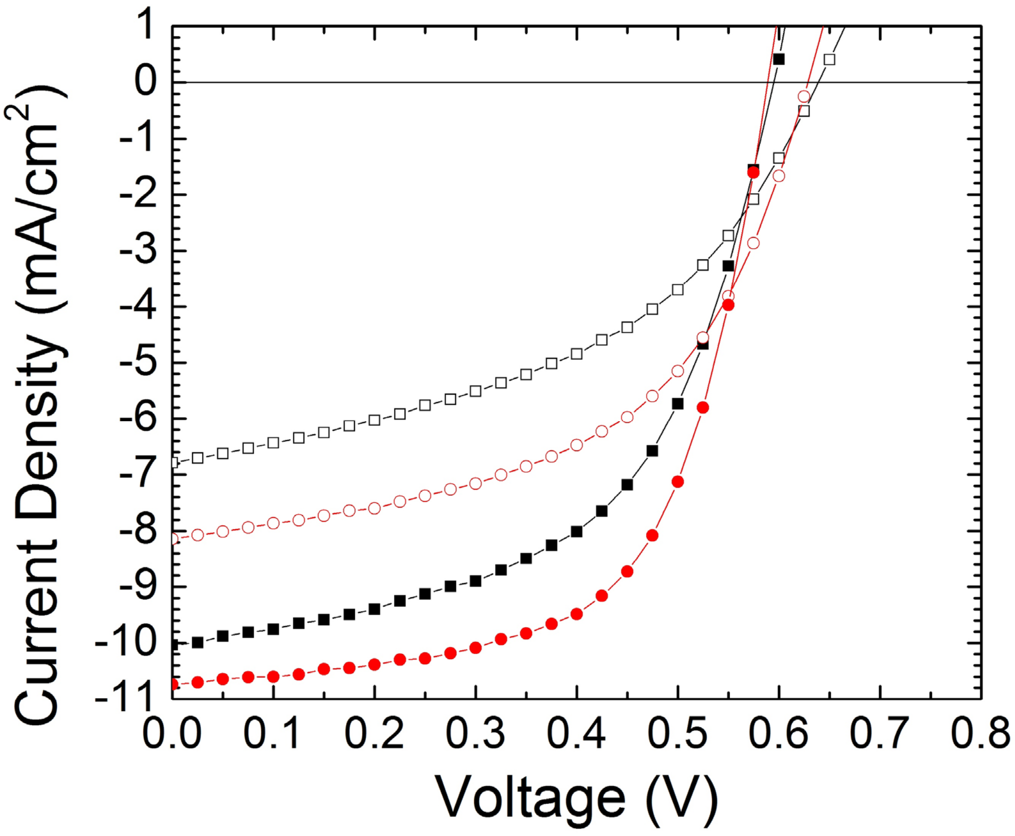

Fig. 2.5 Current density-voltages curves for devices with active layers of P3HT:PCBM film from chlorobenzene (-□-), P3HT:PCBM film from chlorobenzene annealed at 160 °C for 10 minutes (-■-), P3HT:PCBM fibers with a P3HT:PCBM backfill layer (-○-) and P3HT:PCBM fibers with a P3HT:PCBM backfill layer annealed at 160 °C for 10

minutes (-●-) under AM1.5 conditions at 100 mW/cm^2. Curves are from devices from Table 2.

To investigate the origin of this increased PCE in devices which incorporate electrospun fibers, the materials and structures were characterized using optical absorption spectroscopy, diffraction measurements, and atomic force microscopy. The visible absorption spectra for solutions, fiber dispersions in cyclopentanone and thin film devices of P3HT:PCBM are shown in Fig. 2.6. P3HT solution in chlorobenzene shows a broad absorption with a peak at ~450 nm (Fig. 2.6a, black line). The dispersion of electrospun fibers in cyclopentanone shows two distinct peaks and one shoulder peak at ~520 nm, ~560 nm and ~605 nm (Fig. 2.6a, red line). This red shift in absorption characteristics from the solubilized P3HT is indicative of an increase in the conjugation length present in the dispersed fibers of P3HT:PCBM. These peaks correspond to π-π^* transition in solidified P3HT,[78,79] with the shoulder peak being attributed to strong inter-chain interactions.[80] These features are also observed in P3HT fibers made by solution processing reported by Berson et al,[33] although the 610 nm shoulder is lower in relative magnitude compared to the solidified absorption peaks. This suggests the presence of stronger inter-chain interactions from the electrospun fibers. The fiber and film-based device absorption spectra are shown in Fig. 2.6b. The unannealed fiber device exhibits a small red shift (~10 nm) from the unannealed thin-film device, which is attributed to an increased conjugation length. The absorbance of both thin film and fiber-based devices is increased after annealing, particularly for the electrospun fiber-based device. A second peak appears at ~ 550 nm along with a shoulder peak at 610 nm, which again reflects an increase in P3HT inter-chain interactions. The transition dipole moment of the π-π^* transition in P3HT is oriented along the polymer chain axis.[81] As light impinges onto the BHJ normal to the substrate, and increase in absorption between films of identical thicknesses would be due to increased overlap between the transition dipole moment and the electric field vector of the incoming light. The increased absorption in the electrospun fiber based device is thus due to a comparatively larger percentage of polymer chains aligned parallel to the substrate. This increase in photon absorption will lead to an increase in exciton formation which in turn will lead to a larger amount of photo-generated carriers.[82]

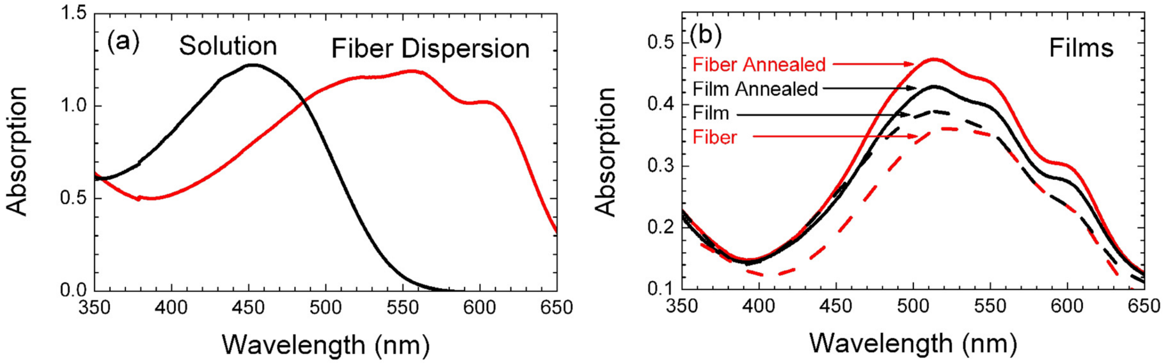

Figure 2.6. Visible absorption spectra of (a) P3HT:PCBM solution in chlorobenzene (black line) and P3HT:PCBM nanofiber dispersion in cyclopentanone and (b) BHJ-OPV devices: P3HT:PCBM films not annealed (black, dashed line) and annealed at 160 °C for 10 minutes (black, solid line) and P3HT:PCBM fibers with a P3HT:PCBM backfill layer not annealed (red, dashed line) and 160 °C for 10 minutes (red, solid line).

Electron and x-ray diffraction measurements were performed in order to study the structural order in annealed fibers and devices. For reference, two crystal planes [(100) and (020)] corresponding to the main diffraction peaks in P3HT are shown in Fig. 2.7a.[83] Fig. 2.7b shows a TEM micrograph of P3HT:PCBM fibers after removal of the PCL sheath and subsequent annealing. The corresponding electron diffraction pattern is shown in Fig. 2.7c. The P3HT:PCBM fibers show strong diffractions from (100) and (020) planes and exhibit fiber symmetry. As chain alignment is often observed in electrospun fibers and both (100) and (020) diffractions are observed it is probable that the polymer chains are aligned along the fiber axis with a mixture of [100] and [010] directions oriented radially along the fiber. For comparison, Inn et al.[84] have shown that P3HT nanofibers made by solution processing techniques do not exhibit the (100) reflections in electron diffraction patterns as these planes are parallel to the electron beam. Electron diffraction patterns of the annealed P3HT:PCBM films without and with incorporated electrospun fibers are shown in Figs. 2.7d and 2.7e, respectively. One dimensional scans shown are shown in Fig. 2.7f. The annealed P3HT:PCBM film exhibits reflections from both the (100) and (020) planes, with a more intense diffraction intensity seen from the (100) plane in this orientation (electron beam normal to the substrate plane). The annealed active layer derived from electrospun fibers shows a different diffraction pattern. Diffraction peaks from the (100) and (020) planes are observed, but the (020) peak is much more intense than the (100) peak. This is evidence that the two devices exhibit different preferences in P3HT crystallite orientation. Since the (020) planes show a stronger diffraction in the fiber derived active layer and a higher optical absorption is observed, a higher quantity of P3HT molecules are likely oriented with the [100] direction normal to the substrate. Without pre-deposited electrospun fibers, the P3HT:PCBM film exhibits a higher intensity in (100) relative to (020). As such, a larger percentage of P3HT polymer chains are likely oriented with the [010] direction perpendicular to the substrate in the film device.

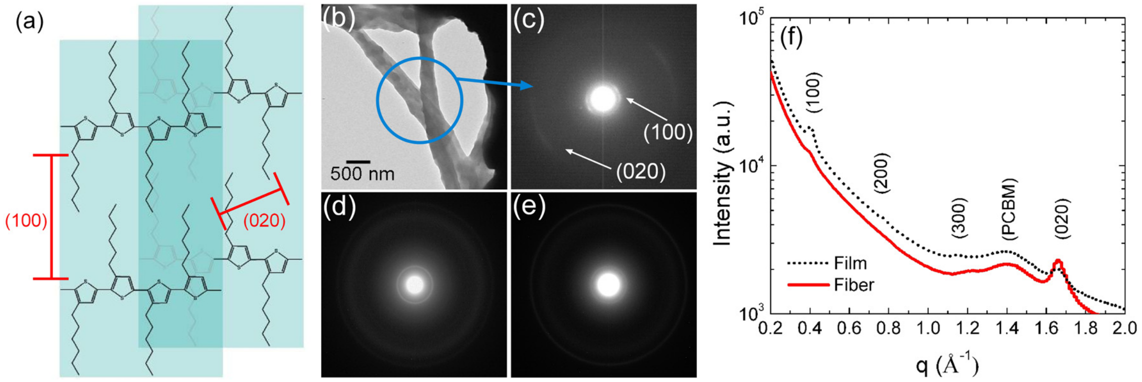

Figure 2.7. (a) Schematic of P3HT crystal structure with (100) and (020) planes highlighted, (b) TEM micrograph of pure P3HT:PCBM fibers annealed for 160 °C for 10 min, (c) electron diffraction pattern from (b) exhibiting fiber symmetry, (d) electron diffraction pattern from a P3HT:PCBM film annealed for 160 °C for 10 min, (e) electron diffraction pattern from a film of P3HT:PCBM fibers with a P3HT:PCBM backfill layer annealed at 160 °C for 10 minutes, and (f) one dimensional scan of (d) (dash lines) and (e) (solid lines).

GIXD results (Fig. 2.8 provide complementary information that confirms the results from the electron diffraction measurements experiments. The 2D pattern for the P3HT:PCBM film-only active layer (Fig. 2.8a) shows a more intense (020) diffraction peak when compared to the electrospun fiber-based active layer (Fig. 2.8b). Conversely, the (100) and higher order (200) and (300) planes are more intense in the fiber-derived active layer when compared to the P3HT:PCBM film. This is more evident in corresponding 1D patterns shown in Fig. 2.8c. For the electrospun fiber-based active layer, the (100) set of reflections are more intense than the (020) on the meridian which indicate that a higher percentage of P3HT crystallites have the π-stacking direction oriented parallel with the substrate. The opposite is seen for the active layer without electrospun fibers, as the (020) peak appears more intense than (100) peak. These results are consistent with those obtained using electron diffraction regarding P3HT crystallite orientation, as both of these experimental methods provide orthogonal information with respect to the P3HT crystallite orientation. As such, the intensity ratio between the (100) and (020) directions should be reversed when comparing the electron diffraction and GIXD data. Herman's orientation parameters[85] were calculated from the azimuthal angle scans (Fig. 2.9) for both electrospun fiber and thin film devices. Crystallites in a sample are perfectly aligned if the orientation parameter equals one, while a completely isotropic sample has an orientation parameter of zero. The active layer with electrospun fibers exhibits a larger orientation parameter (0.72) in the (100) planes than the thin film active layer (0.56). This indicates better in-plane alignment of these crystallites.

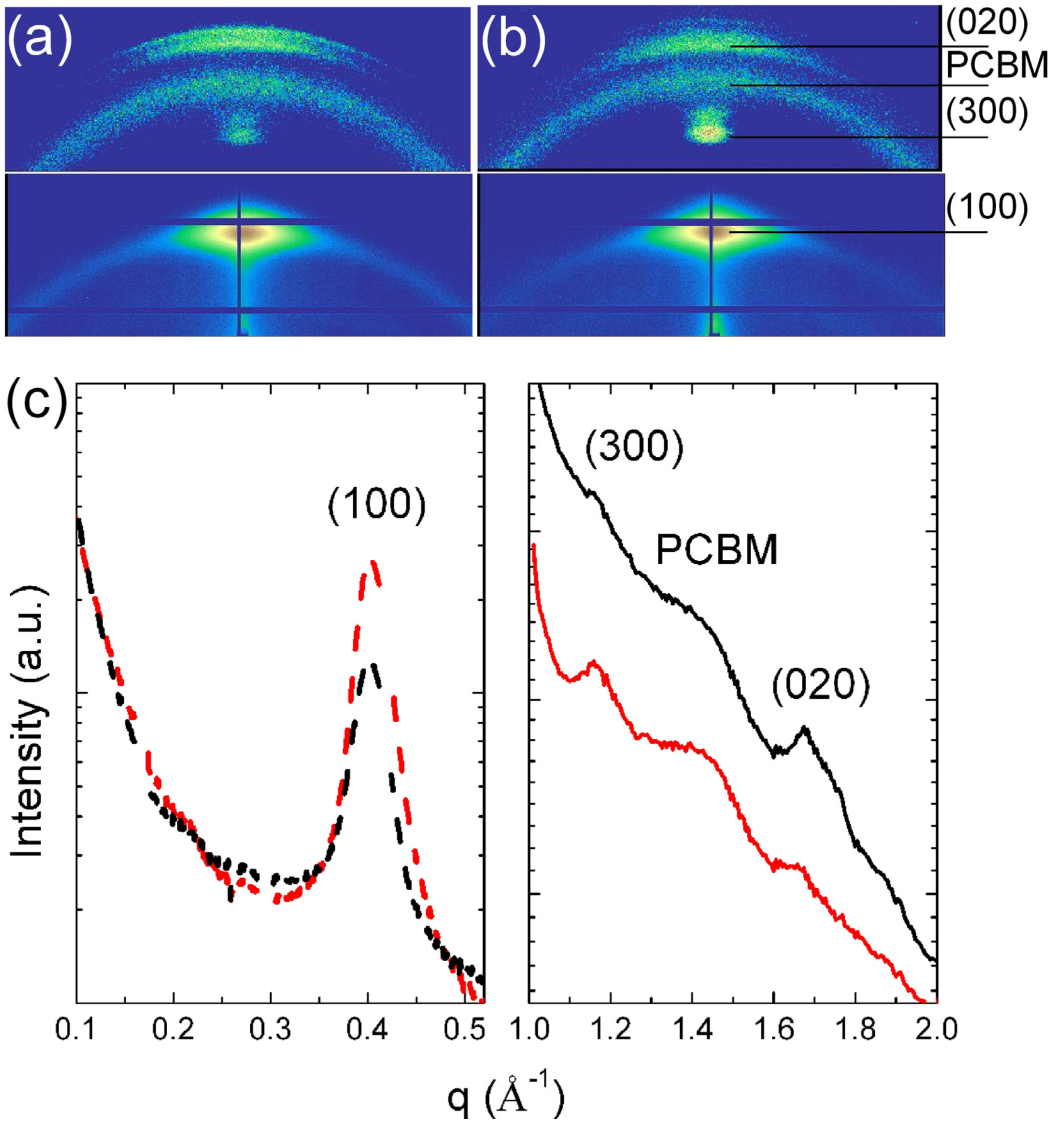

Fig. 2.8 Two dimensional GIXD patterns of devices consisting of (a) a P3HT:PCBM active layer annealed for 160 °C for 10 min and (b) fiber-based P3HT:PCBM active layer

annealed at 160 °C for 10 minutes. The top pattern is wide angles scattering and the bottom is small angle scattering (c) Corresponding small angle (dashed lines) and wide angle (solid lines) diffraction patterns of P3HT:PCBM films (black lines) and fiber-based P3HT:PCBM films (red lines).

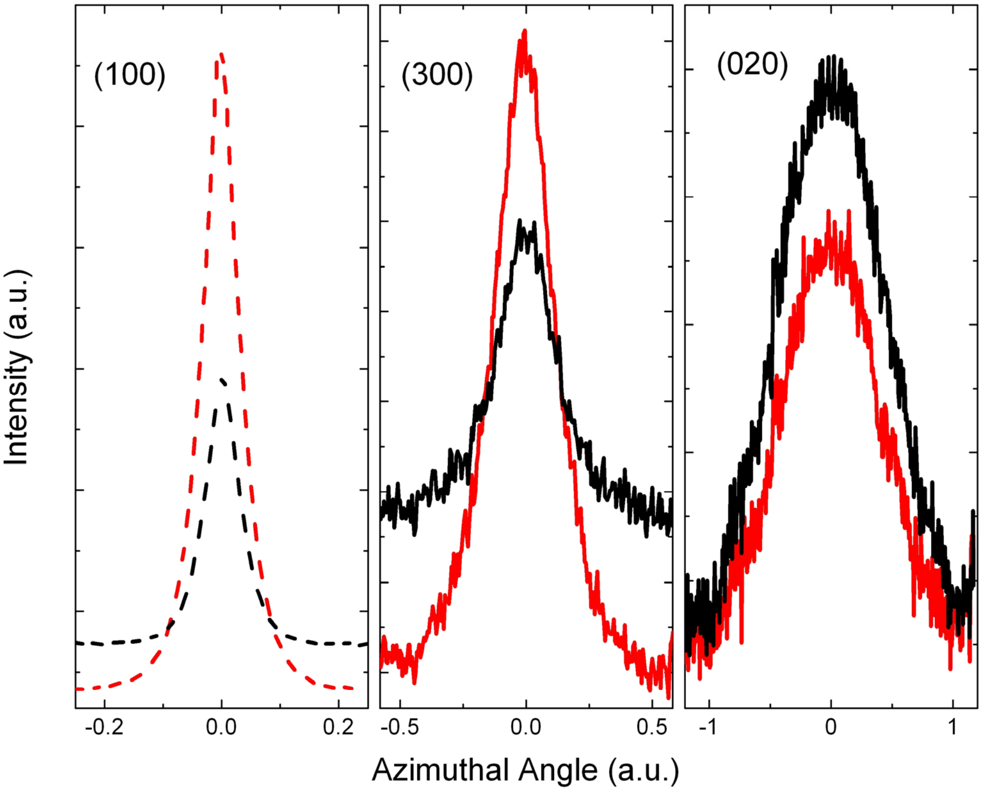

Fig. 2.9 Azimuthal angle of the (100), (300), and (020) reflections for P3HT:PCBM films (black lines) and fiber-based P3HT:PCBM films (red lines).

The distinct orientation difference between the two samples is caused by the presence of electrospun fibers within the active layer which ultimately leads to the difference in device performance. After the backfill deposition of solubilized P3HT:PCBM onto the electrospun P3HT:PCBM fibers, it is probable that the fibers act as a template for in-plane chain alignment throughout the active layer. This conclusion is evident when considering the increased optical absorption due to in-plane alignment of the π-π* transition along the polymer backbone (Fig. 2.6b) and the fiber symmetry displayed in annealed P3HT:PCBM fibers (Fig. 2.7c). Increased photon absorption would lead to the generation of more excitons, which in turn increases the number of carriers potentially available for collection. It is presumed that regions in the electrospun fiber based active layer not in the vicinity of the pre-deposited fibers adopt a crystallite orientation similar to that of the thin film active layer (π-stacking predominately normal to the substrate). Charge transport has been found to be highest along the polymer backbone, then through π-stacking, and finally through alkyl chains in P3HT.[86,87] The fibrous regions are thus responsible for increased photon absorption and an in-plane charge transport while the non-fibrous regions transport charge to the appropriate electrodes. The thin film based devices comparatively lack the amount of in-plane chain alignment and thus does not absorb as many photons, leading to a lower PCE.

To further investigate the role of electrospun fibers in the structure and orientation of BHJ-OPV active layers, in-situ annealing GIXD studies were performed. Diffraction patterns were taken every two minutes during the annealing processes similar to those used in the previous experimentation in a custom made heating chamber (Fig. 2.10). The size of the P3HT crystallites during annealing were approximated from the full-width at half-maximum (FWHM) for the (100) diffraction using the Scherrer's equation[88] (Fig. 2.11). The thin film device shows an average crystallite size of ~ 165 Å, which slowly increases to ~170 Å throughout the annealing process. The electrospun fiber based device has crystallites with a thickness of ~170 Å prior to annealing. During annealing, the size of the crystallites oscillates around this value until the temperature starts to decrease. A sharp increase in the crystallite size than occurs, to a final value of ~205 Å. An increase in crystallite size has been found to lead to improved PCE which is attributed increased light harvesting[89] and, to a lesser extent, increased carrier mobility.[90,91] This can also be used to explain the higher PCE exhibited by the electrospun fiber based device.

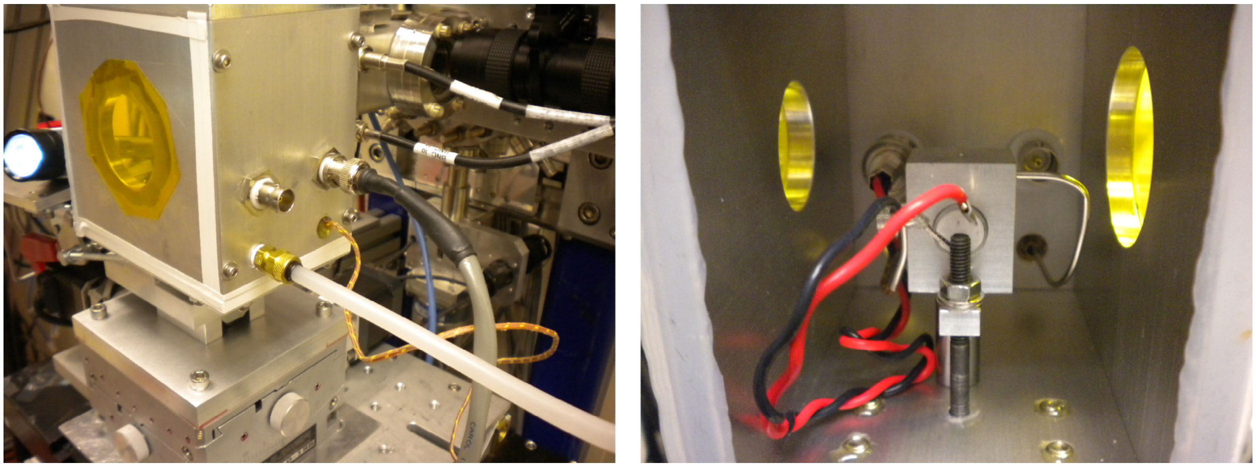

Fig. 2.10 Heating chamber used for in-situ annealing GIXD experiments.

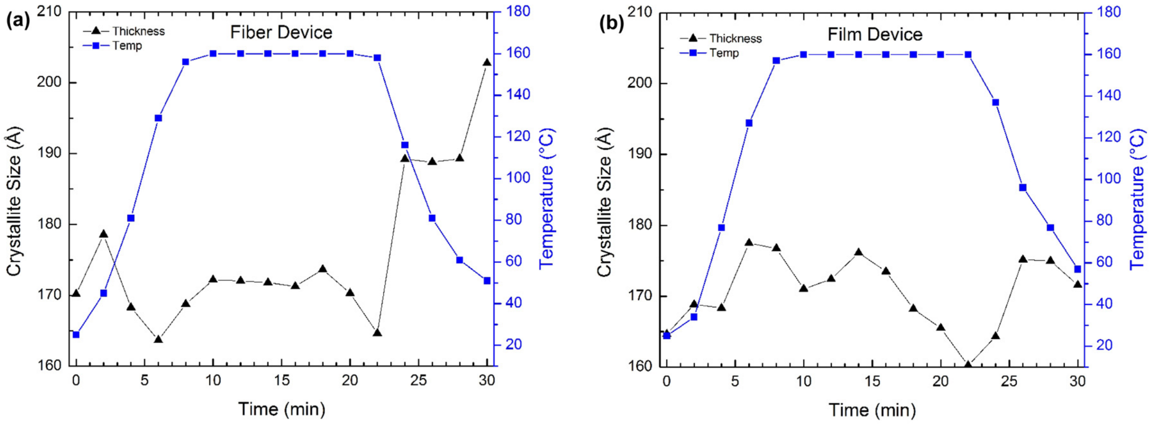

Fig. 2.11 Crystallite size as a function of thermal annealing. Crystallite size calculated from P3HT (100) diffractions for (a); the electrospun fiber based device and (b) thin film device.

D-spacing between (100) planes in P3HT were found to change during the annealing process for all devices tested (Fig. 2.12). The d-spacing increases during annealing then decreases irreversibly upon cooling to a value greater than the un-annealed material. This has been previously observed in other studies[92,93] and has been attributed to thermal expansion. The electrospun fiber based devices displays a slightly lower d-spacing than the thin film devices (Figs. 2.12a and 2.12b), but also exhibits a shoulder peak of larger d-spacing (~18.3 Å) once the annealing temperature of 160 °C has been reached. This shoulder peak disappears from the diffraction pattern after the annealing process. In-situ annealing GIXD experiments and subsequent d-spacing analysis were also performed for P3HT:PCBM fibers (Fig. 2.12c). The (100) d-spacing for the electrospun fibers remains around 18.3 Å through the heating a cooling processes. This is particularly interesting for as the shoulder peaks in Fig. 2.12b have the same d-spacing as the stand-alone fibers, which suggest the structure of the P3HT:PCBM fibers is partially maintained during the backfill process. Not much is known on the effect of d-spacing on device performance. Yang and co-workers suggest that lower V_{oc} values in P3HT:PCBM devices with small-molecule processing agents were due to lower d-spacing values in these devices. However, the results presented in this chapter show the contrary, and thus more work is needed to fully understand the effect that d-spacing on device performance. Regardless, the data shown in Fig. 2.12 demonstrates that the structural coherence of the electrospun fibers is maintained after the deposition of the backfill layer.

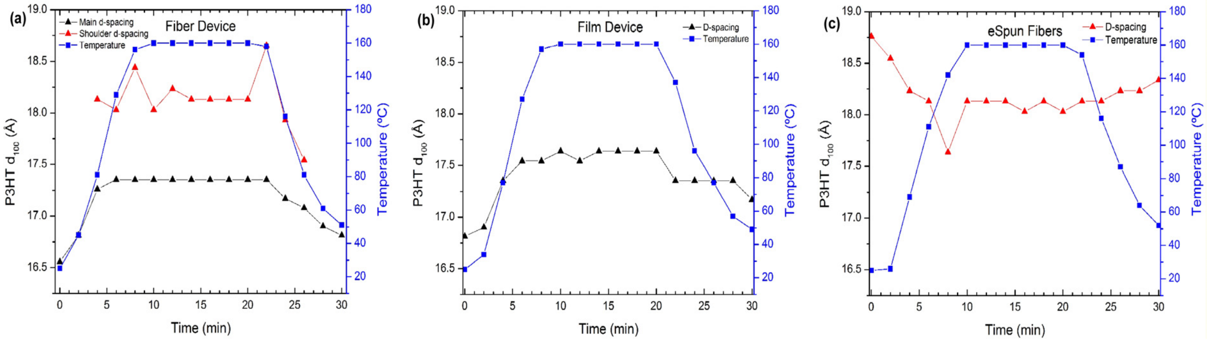

Fig. 2.12 P3HT (100) d-spacing as a function of thermal annealing for (a); the electrospun fiber based device (shoulder peak d-spacing shown in red), (b) thin film device and (c) P3HT-PCBM fibers dropcast on PEDOT/ITO electrode.

The Herman's orientation parameter was also calculated from the in-situ annealing GIXD measurements (Fig. 2.13). As reported above, the electrospun fiber device shows a higher orientation parameter after annealing than the thin film device. Through the annealing process, the value of the orientation parameter does not change drastically for either the electrospun fiber device or thin film device. The fiber based device maintains a larger orientation parameter than the thin film device during the annealing process. These results suggest that the increase orientation of P3HT crystallites is due exclusively to the presence of the electrospun fibers and not from thermal annealing.

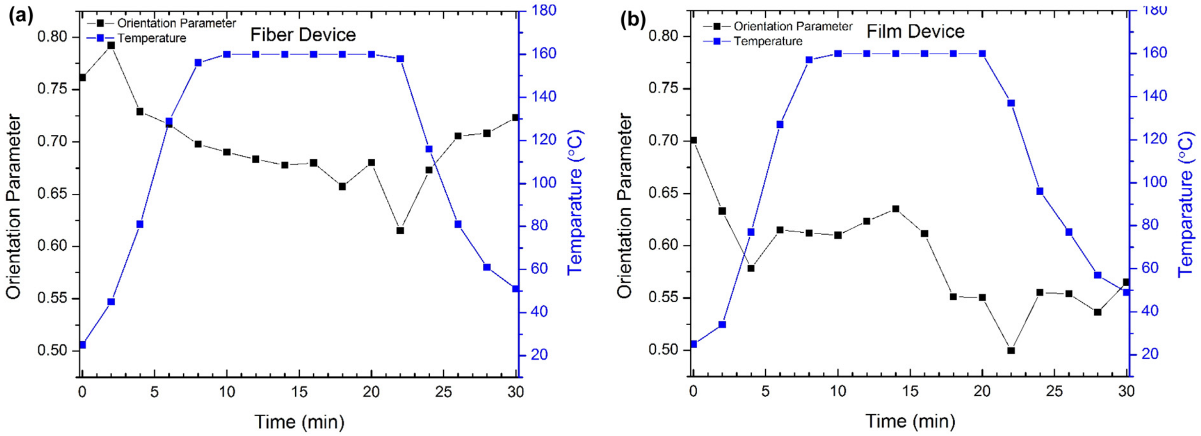

Fig. 2.13 Orientation pararmeter as a function of thermal annealing for (a); the electrospun fiber based device (shoulder peak d-spacing shown in red), and (b) thin film device.

The surface roughness and surface morphology of the devices was studied using AFM (Fig. 2.14). The surface of a P3HT:PCBM BHJ has been shown to be rich in P3HT for films made from spin coating and thus is not representative of the bulk morphology,[94,95] leaving AFM data to be often over-interpreted. However, the inclusion of electrospun fibers (on the size scale of the BHJ thickness) likely invokes a unique morphology and surface roughness and thus should be examined. Height images from unannealed and annealed thin film devices are shown in Figs. 2.14a and 2.14c respectively. The root-mean-square (RMS) surface roughness from these devices is 6.22 Å for the unannealed device and 9.06 Å for the annealed device. These values are comparable to what is typically observed for such films.[96] The addition of electrospun P3HT:PCBM fibers to the active layer yields an RMS surface roughness of 9.41 Å (Fig. 2.14e), which is larger than the annealed device without electrospun fibers. Further annealing of the fiber-based active layer yields a RMS surface roughness double that of the unannealed device (18.4 Å, Fig. 2.14g). While an increase in surface roughness is often thought to be a "signature" of higher efficiency devices,[31] it is difficult to completely decouple the effects of altered BHJ morphology and increased surface roughness on device performance. The nanoscale phase separation was studied using phase imaging, wherein "hard" and "soft" segments yield different contrast levels in the image. The unannealed P3HT:PCBM film device shows small domains of P3HT and PCBM (Fig. 2.14b), which after annealing characteristically become larger (Fig. 2.14d).[23] Devices with the inclusion of electrospun P3HT:PCBM fibers show a very different morphology for both unannealed (Fig. 2.14f) and annealed (Fig. 2.14h) devices. The morphologies show anisotropic features that are much smaller (~15 nm) than the electrospun P3HT:PCBM fibers, which tend to partially orient in a similar direction over 200 to 500 nm length scales. It is likely that these 200-500 nm oriented regions are remnants from the electrospun P3HT:PCBM fibers. Due to electron beam damage the in-plane orientation of these P3HT crystallites could not be captured with TEM. However, optical absorption data (Fig. 2.6) suggest these anisotropic features, absent in the thin film devices, must have P3HT chains aligned in the plane of the substrate.

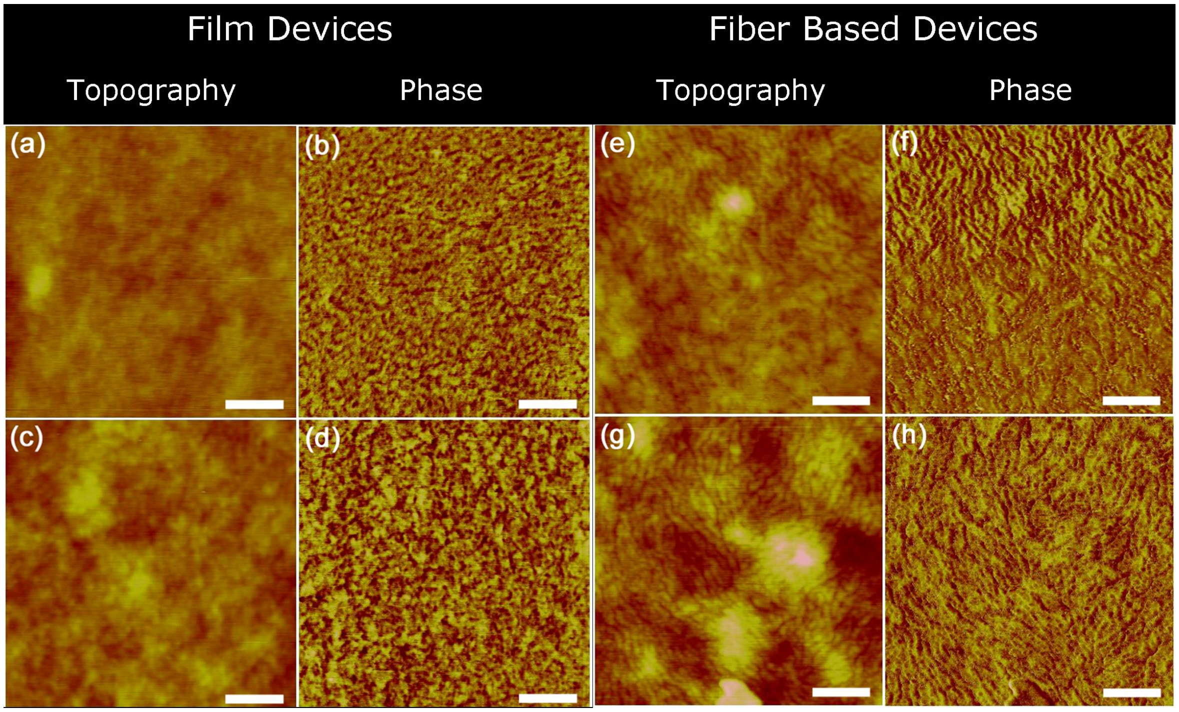

Fig. 2.14 AFM topography (left) and phase images (right) of devices from a, b) as cast film of P3HT:PCBM, c,d) annealed film of P3HT:PCBM at 160 °C for 10 minutes, e,f), P3HT:PCBM fibers with a P3HT:PCBM backfill layer and g,h) P3HT:PCBM fibers with a P3HT:PCBM backfill layer annealed at 160 °C for 10 minutes. All height images have a 15 nm z-axis range. All images are 1 μm × 1 μm.

2.4 Conclusions

P3HT:PCBM fibers were made via coaxial electrospinning using PCL as the sacrificial sheath material. By using coaxial electrospinning, a uniform phase separation between the PV materials and the more easily electrospun polymer can be achieved which is not possible by simply blending the materials. Selectively stripping the PCL from the coaxial fibers yields pure P3HT:PCBM nanofibers. When embedded within the active layer these fibers likely act as templates for increased in-plane polymer chain alignment in these devices and invoke an orientation likely beneficial for higher charge mobility. This altered macroscopic orientation, leads to increased J_{sc}, FF, and PCE in the BHJ-OPV devices when compared to films of P3HT:PCBM of identical composition (2.4 to 3.2% average PCE in annealed samples, best PCE of 3.2 and 4.0%). The use of electrospun fibers within the active layer of BHJ-OPV is a promising methodology for improving the performance of such devices. This methodology is more practical than creating free standing "solar clothes" due to the ease of device fabrication and the resulting increased PCEs that are more useful for real world PV applications. Thermal solution processing of polymeric nanofibers is only possible if the material can dissolve at an elevated temperature in a particular solvent and re-crystallize in a fibrous manner once the temperature has been lowered. This likely cannot be done in the presence of another molecular moiety, such as an electron accepting material. Electrospinning allows for a relatively large amount of fibrous material of almost any composition to be easily generated in a short amount of time which can be implemented into the active layer of the device. The use of coaxial electrospinning, in particular, is even more advantageous as it avoids issues with blended polymer morphologies, uses smaller quantities of active layer material, and uses an electrospinning process largely governed by the electrospinability of the sheath material. While this initial study has focused on the use of P3HT:PCBM, it is likely that this methodology for creating electrospun fibers can be extended to other electron donor/electron acceptor materials systems.

---

[1] The bulk of this chapter appears in: N. M. Bedford, M. B. Dickerson, L. F. Drummy, H. Koerner, K. M. Singh, M. F. Durstock, R. R. Naik, A. J. Steckl, *Small*, **2011**, *submitted.*

[2] G. Dennler, M. C. Scharber, C. J. Brabec, *Adv. Mater.* **2009**, *21*, 1323-1338.

[3] J. Peet, A. J. Heeger, G. C. Bazan, *Acc. Chem. Res.* **2009**, *42*, 1700-1708.

[4] A. J. Moulé, K. Meerholz, *Adv. Funct. Mater.* **2009**, *19*, 3028-3036.

[5] B. C. Thompson, J. M. J. Fréchet, *Angew. Chem. Int. Ed.* **2008**, *47*, 58-77.

[6] C. J. Brabec, J. A. Hauch, P. Schilinsky, C. Waldauf *Mater. Res. Soc. Bull.* **2005**, *30*, 50-52.

[7] W. Ma, C. Yang, X. Gong, K. Lee, A. J. Heeger, *Adv. Funct. Mater.* **2005**, *15*, 1617-1622.

[8] G. Li, V. Shrotriya, J. Huang, Y. Yao, T. Moriarty, K. Emery, Y. Yang, *Nat. Mater.* **2005**, *4*, 864-868.

[9] M. Reyes-Reyes, K. Kim, J. Dewald, R. López-Sandoval, A. Avadhanula, S. Curran, D. L. Carroll, *Org. Lett.* **2005**, *7*, 5749-5752.

[10] H.-Y. Chen, J. Hou, S. Zhang, Y. Liang, G. Yang, Y. Yang, L. Yu, G. Li, *Nat. Photonics* **2009**, *3*, 649-653.

[11] S. H. Park, A. Roy, S. Beaupré, S. Cho, N. Coates, J. S. Moon, D. Moses, M. Leclerc, K. Lee, A. J. Heeger, *Nat. Photonics* **2009**, *3*, 297-303.

[12] Y. Lang, D. Feng, Y. Wu, S.-T. Tsai, G. Li, C. Ray, L. Yu, *J. Amer. Chem. Soc.* **2009**, *131*, 7792-7799.

[13] Y. Lang, Y. Wu, D. Feng, S.-T. Tsai, H.-J. Son, G. Li, L. Yu, *J. Amer. Chem. Soc.* **2009,** *131*, 56-57.

[14] C.-P. Chen, S.-H. Chan, T.-C. Chao, C. Ting, B.-T. Ko, *J. Amer. Chem. Soc.* **2008**, *130*, 12828-12833.

[15] N. Blouin, A. Michaud, M. Leclerc, *Adv. Mater.* **2007**, *19*, 2295-2300.

[16] J. Chen, Y. Cao, *Acc. Chem. Res.* **2009**, *42*, 1709-1718.

[17] O. Inganäs, F. Zhang, M. R. Andersson, *Acc. Chem. Res.* **2009**, *42*, 1731-1739.

[18] J. Y. Kim, K. Lee, N. E. Coates, D. Moses, T.-Q. Nguyen, M. Dante, A. J. Heeger, *Science* **2007**, *317*, 222-225.

---

[19] A. Hadipour, B. de Boer, P. W. M. Blom, *J. Appl. Phys.* **2007**, *102*, 074506.

[20] S. Sista, M.-H. Park, Z. Hong, Y. Wu, J. Hou, W. K. Kwan, G. Li, Y. Yang, *Adv. Mater.* **2010**, *22*, 380-383.

[21] T. Ameri, G. Dennler, C. Lungenschmied, C. J. Brabec, *Energy Environ. Sci.* **2009,** *2*, 347-363.

[22] T. M. Clarke, A. M. Ballantyne, J. Nelson, D. D. C. Bradley, J. R. Durrant, *Adv. Funct. Mater.* **2008**, *18*, 4029-4035.

[23] A. L. Ayzner, D. D. Wanger, C. J. Tassone, S. H. Tolbert, B. J. Schwartz, *J. Phys. Chem C* **2008**, *122*, 18711-18716.

[24] M. Al-Ibrahim, O. Ambacher, S. Sensfuss, G. Gobsch, *Appl. Phys. Lett.* **2005**, *86*, 201120.

[25] G. Li, Y. Yao, H. Yang, V. Shrotriya, G. Yang, Y. Yang, *Adv. Funct. Mater.* **2007**, *17*, 1636-1644.

[26] H. Tang, G. Lu, L. Li, J. Li, Y. Wang, X. Yang, *J. Mater. Chem* **2010**, *20*, 683-688.

[27] J. H. Park, J. S. Kim, J. H. Lee, W. H. Lee, K. Cho, *J. Phys. Chem. C* **2009**, *113*, 17579-17584.

[28] F. Zhang, K. G. Jespersen, C. Björström, M. Svensson, M. R. Andersson, V. Sundström, K. Magnusson, E. Moons, A. Yartsev, O. Inganäs, *Adv. Funct. Mater.* **2006**, *16*, 667-674.

[29] J. Peet, J. Y. Kim, N. E. Coates, W. L. Ma, D. Moses, A. J. Heeger, G. C. Bazan, *Nat. Mater.* **2007**, *6*, 497-500.

[30] J. K. Lee, W. L. Ma, C. J. Brabec, J. Yuen, J. S. Moon, J. Y. Kim, K. Lee, G. C. Bazan, A. J. Heeger, *J. Amer. Chem. Soc.* **2008**, *130*, 3619-3623.

[31] Y. Yao, J. Hou, Z. Xu, G. Li, Y. Yang, *Adv. Funct. Mater.* **2008**, *18*, 1783-1789.

[32] A. J. Moulé, K. Meerholz, *Adv. Mater.* **2008**, *20*, 240-245.

[33] S. Berson, R. De Bettignies, S. Bailly, S. Guillerez, *Adv. Funct. Mater.* **2007**, *17*, 1377-1384.

[34] Y. Zhao, S. Shao, Z. Xie, Y. Geng, L. Wang, *J. Phys. Chem. C* **2009**, *113*, 17235-17239.

[35] H. Xin, F. S. Kim, S. A. Jenekhe, *J. Amer. Chem. Soc.* **2008**, *130*, 5424-5425.

[36] H. Xin, G. Ren, F. S. Kim, S. A. Jenekhe, *Chem. Mater.* **2008**, *20*, 6199-6207.

[37] D. Li, Y. Xia, *Adv. Mater.* **2004**, *16*, 1151-1170.

[38] S. Agarwal, A. Greiner, J. H. Wendorff, *Adv. Funct. Mater.* **2009,** *19*, 2863-2879.

[39] D. H. Reneker, I. Chun, *Nanotechnol.* **1996**, *7*, 216-223.

[40] D. Lukas, A. Sarkar, P. Pokomy, *J. Appl. Phys.* **2008**, *103*, 084309.

[41] A. Kumar, M. Wei, C. Barry, J. Chen, J. Mead, *Macromol. Mater. Eng.* **2010**, *295*, 701-708.

[42] G. Kim, Y.-S. Cho, W. D. Kim, *Eur. Polym. J.* **2006**, *42*, 2031-2038.

[43] E. Kostakova, L. Meszaros, J. Gregr, *Mater. Lett.* **2009**, *63*, 2419-2422.

[44] M. Zukalova, J. Prochazka, Z. Bastl, J. Duchoslav, L. Rubacek, D. Havlicek, L. Kavan, *Chem. Mater.* **2010**, *22*, 4045-4055.

[45] J. Xie, X. Li, Y. Xia, *Macromol. Rapid Comm.* **2008**, *29*, 1775-1792.

[46] H. S. Yoo, T. G. Kim, T. G. Park, *Adv. Drug Del. Rev.* **2009**, *61*, 1033-1042.

[47] Y. Ner, J. G. Grote, J. A. Stuart, G. A. Sotzing, *Angew. Chim. Int. Ed.* **2009**, *48*, 5134-5138.

[48] G. Kwak, G. H. Lee, S.-H. Shim, K.-B. Yoon, *Macromol. Rapid. Commun.* **2008**, *29*, 815-820.

[49] E. Formo, E. Lee, D. Campbell, Y. Xia, *Nano Lett.* **2008**, *8*, 668-672.

[50] S. Zhan, D. Chen, X. Jiao, C. Tao, *J. Phys. Chem. B* **2006**, *110*, 11199-11204.

[51] H.-W. Lu, L. Yu, W. Zheng, Y.-S. Li, Z.-W. Fu, *Electrochem. Solid-State Lett.* **2008**, *11*, A140-A144.

[52] L. Ji, X. Zhang, *Nanotechnol.* **2009**, *20*, 155705.

[53] C. Chang, V. H. Tran, J. Wang, Y.-K. Fuh, L. Lin, *Nano Lett.* **2010**, *10*, 726-731.

[54] A. R. S. Priya, A. Subramania, Y.-S. Jung, K.-J. Kim, *Langmuir* **2008**, *24*, 9816-9819.

[55] X.-S. Qin, S.-Y. Wang, *J. Appl. Polym. Sci.* **2006**, *102*, 1285-1290.

[56] P. Heikkilä, A. Taipale, M. Lehtimäki, A. Harlin, *Polym. Engin. Sci.* **2008**, *48*, 1168-1176.

[57] M. Wang, N. Jing, C. B. Su, J. Kameoka, C.-K. Chou, M.-C. Hung, K.-A. Chang, *Appl. Phys. Lett.***2006**, *88*, 033106

[58] N. M. Bedford, A. J. Steckl, *ACS Appl. Mater. Interfaces* **2010**, *2*, 2448-2455.

---

[59] H. Liu, C. H. Reccius, H. G. Craighead, *Appl. Phys. Lett.* **2005**, *87*, 253106.

[60] S. Lee, G. D. Moon, U. Jeong, *J. Mater. Chem.* **2009**, *19*, 743-748.

[61] S. W. Lee, H. J. Lee, J. H. Choi, W. G. Koh, J. M. Myoung, J. H. Hur, J. J. Park, J. H. Cho, U. Jeong *Nano Lett.* **2010**, *10*, 347-351.

[62] C.-C. Kuo, C.-T. Wang, W.-C. Chen, *Macromol. Symp.* **2009**, *279*, 41-47.

[63] A. Laforgue, L. Robitaille, *Synth. Met.* **2008**, *158*, 577-584.

[64] S. Chuangchote, M. Fujita, T. Sagawa, H. Sakaguchi, S. Yoshikawa *ACS Appl. Mater. Interfaces*, **2010**, *2*, 2995-2997.

[65] S. Sundarrajan, R. Murugan, A. S. Nair, S. Ramakrishna, *Mater. Lett.* **2010**, *64*, 2369-2372.

[66] Comprehensive data reduction macro package for converting 2D SAS area detector to 1D SAS lineout, developed by Jan Ilavsky at Argonne National Laboratory, version 1.17.

[67] S. O. Han, J. H. Youk, K. D. Min, Y. O. Kang, W. H. Park, *Mater. Lett.*, **2008,** *62*, 759-762.

[68] J. M. Deitzel, J. Kleinmeyer, D. Harris, N. C. B. Tan, *Polymer*, **2001**, *42*, 261-272.

[69] S. R. Bhattarai, N. Bhattarai, H. K. Yi, P. H. Hwang, D. I. Cha, H. Y. Kim, *Biomaterials*, **2004**, *25*, 2595-2602.

[70] H. Liu, J. Kameoka, D. A. Czaplewski, H. G. Craighead, *Nano Lett.* **2008**, *4*, 671-675.

[71] K. Zhang, X. Wang, Y. Yang, L. Wang, M. Zhu, B. S. Hsiao, B. Chu, *J. Polym. Sci., Part B: Polym. Phys.* **2010**, *48*, 1118-1125.

[72] Z. Chen, M. D. Foster, W. Zhou, H. Fong, D. H. Reneker, R. Resendes, I. Manners, *Macromolecules* **2001**, *34*, 6156-6158.

[73] P. E. Shaw, A. Ruseckas, I. D. W. Samuel, *Adv. Mater.* **2008**, *20*, 3516-3520.

[74] G. Li, V. Shrotriya, Y. Yao, Y. Yang, *J. Appl. Phys.* **2005**, *98*, 043704.

[75] A. K. Moghe, B. S. Gupta, *Polym. Rev.* **2008**, *48*, 353-377.

[76] D. H. Wang, H. K. Lee, D.-G. Choi, J. H. Park, O. O. Park, *App. Phys. Lett.* **2009**, *95*, 043505.

[77] J. Nakamura, K. Murata, K. Takahashi, *Appl. Phys. Lett.* **2005**, *87*, 132105.

[78] P. D. Cunningham, L. M. Hayden, *J. Phys. Chem. C* **2008**, *112*, 7928-7935.

[79] V. Shrotriya, J. Ouyang, R. J. Tseng, G. Li, Y. Yang, *Chem. Phys. Lett.* **2005**, *411*, 138-143.

[80] P. J. Brown, D. S. Thomas, A. Köhler, J. S. Wilson, J.-S. Kim, C. M. Ramsdale, H, Sirringhaus, R. H. Friend, *Phys. Rev. B* **2003**, *67*, 064203.

[81] M. C. Gurau, D. M. Delongchamp, B. M. Vogel, E. K. Lin, D. A. Fischer, S. Sambasivan, Lee. J. Richter, *Langmuir*, **2007**, *23*, 834-842.

[82] Y. Kim, S. Cook, S. M. Tuladhar, S. A. Choulis, J. Nelson, J. R. Durrant, D. D. C. Bradley, M. Giles, I. McCulloch, C.-S. Ha, M. Ree, *Nat. Mater.* **2006**, *5*, 197-203.

[83] L. F. Drummy, R. J. Davis, D. L. Moore, M. Durstock, R. A. Vaia, J. W. P. Hsu, *Chem. Mater.* **2011**, *23*, 907-912.

[84] K. J. Ihn, J. Moulton, P. Smith, *J. Polym. Sci. Part B Polym. Phys.* **1993**, *31*, 735-742.

[85] S. Saengsuwan, G. R. Mitchell, S. Bualek-Limcharoen, *Polymer*, **2003**, *44*, 5951.

[86] B. O'Connor, R. J. Kline, B. R. Conrad, L. J. Richter, D. Gundlach, M. F. Toney, D. M. DeLongchamp, *Adv. Funct. Mater.* **2011**, *21*, 3697-3705.

[87] Y.-K. Lan, C.-I. Huang, *J. Phys. Chem. B* **2009**, *113*, 14555-14564.

[88] M.-Y. Chiu, U.-S. Jeng, C.-H. Su, K. S. Liang, K.-H. Wei, *Adv. Mater.* **2008**, *20*, 2573-2578.

[89] M. Shin, H. Kim, J. Park, S. Nam, K. Heo, M. Ree, C.-S. Ha, Y. Kim, *Adv. Funct. Mater.* **2010**, *20*, 748-754.

[90] H.-G. Flesch, R. Resel, C. R. McNeill, *Org. Electron.,* **2009**, *10*, 1549.

[91] H.-Y. Chen, H. Yang, G. Yang, S. Sista, R. Zadoyan, G. Li, Y. Yang, *J. Phys. Chem. C*, **2009**, *113*, 7946.

[92] S. Lilliu, T. Agostinelli, E. Pires, M. Hampton, J. Nelson, J. E. Macdonald, *Macromolecules* **2011**, *44*, 2725.

[93] E. Verploegen, R. Mondal, C. J. Bettinger, S. Sok, M. F. Toney, Z. Bao, *Adv. Funct. Mater.* **2010**, *20*, 3519.

---

[94] D. Chen, A. Nakahara, D. Wei, D. Nordlund, T. P. Russel, *Nano Lett.* **2011**, *11*, 561-567.

[95] A. J. Parnell, A. D. F. Dunbar, A. J. Pearson, P. A. Staniec, A. J. C. Dennison, H. Hamamatsu, M. W. A. Skoda, D. G. Lidzey, R. A. L. Jones, *Adv. Mater.* **2010**, *22*, 2444-2447.

[96] B. Xue, B. Vaughan, C.-H. Poh, K. B. Burke, L. Thomsen, A. Stapleton, X. Zhou, G. W. Bryant, W. Belcher, P. C. Dastoor, *J. Phys. Chem. C* **2010,** *114*, 15797-15805.

Chapter 3:
Immobilization of Stable Thylakoid Vesicles in Conductive Nanofibers by Electrospinning[1]

3.1 Introduction

Photosynthetic biological materials recently have been receiving much attention[2] for potential use in optoelectronic, organic photovoltaic (OPV) and sensor applications given their superior photo-responsive properties and inherent biodegradability/renewability. The structural hierarchy of available photosynthetic materials starts with the chromophore (such as chlorophyll molecules, derivatives of chlorophyll and other accessory pigments) and moves up to the pigment-containing membrane-spanning proteins (such as photosystems I and II in plants and reaction center in bacteria). These proteins are part of a double membrane envelope called the thylakoid membrane (or simply thylakoid) which houses the light reactions of photosynthesis that is ultimately responsible for the synthesis of ATP in photosynthetic species (inset, Figure 3.1).[3] Biological photosynthetic chromophores have been previously used in the fabrication of OPVs[4] and dye-sensitized solar cells[5,6,7,8], while photosystems and reaction centers have shown promise in OPVs/photoelectronic[9,10,11,12,13,14,15,16] and sensors applications.[17,18] The inclusion of larger structural units such as thylakoids into a material's matrix is of particular interest as the encapsulation of intact and functioning thylakoids would be a step toward a photosynthetic "living material".[19] Previously, thylakoids embedded into a silica matrix were shown to have improved activity when compared to a free thylakoid suspension[20], while thylakoids immobilized in a cross-linked glutaraldehyde have exhibited the ability to detect herbicides.[21]

Electrospinning[22,23] is an established method for creating continuous fibers ranging from tens of nanometers to microns in diameter. This is accomplished by applying a high voltage between a droplet of solution at the end of a spinneret and a collecting substrate. Under the proper conditions (solution conductivity, viscosity, etc.), the applied electric field causes a liquid jet to eject from the droplet toward the collecting substrate. During this process the jet quickly elongates, reduces in diameter, and loses solvent resulting in a non-woven mesh of fibers with high surface to volume ratio. Previously it has been demonstrated that biological macrostructures such as living cells[24], bacteria[25,26,27,28], viruses[29], and enzymes[30] can be blended into polymer solutions and electrospun while still retaining their biological function.

In this work, electrospinning is used to create nanofibers from a solution of thylakoids, poly(3,4-ethylenedioxythiophene):poly(styrene sulfonate) (PEDOT:PSS, herein referred to as PEDOT) and poly(ethylene oxide) (PEO). By immobilizing thylakoids into electrically conductive PEDOT/PEO nanofibers, changes in electronic properties with response to light can be measured. These nanofibers exhibit light induced changes in electronic properties attributed to the photosystems inside the thylakoids. Transmission electron micrographs show that thylakoid vesicles are present within the fibers, while lipid-specific fluorescence staining also indicates the presence of a stable lipophilic environment within the nanofibers. The viability of the thylakoids during the fiber formation process was tested by measuring light-induced pH change prior to and after electrospinning. To the authors' knowledge, this study represents the first attempt to encapsulate and immobilize active thylakoids into electrospun fibers which could potentially be used in optoelectronic applications.

3.2 Experimental

3.2.1 Thylakoid Isolation

The thylakoid isolation was adapted from Izawa and Good.[31] Briefly, spinach leaves were washed and de-veined, then homogenized in a Waring blender three times for 10 seconds in a cold aqueous solution of 2 mM Na_2EDTA, 40 mM K_2HPO_4, 10 mM KH_2PO_4 and 0.35 mM NaCl. The homogenate was filtered through four layers of cheesecloth and centrifuged at 3000 × g for five minutes. All centrifugation steps were performed at 4 °C (Sorvall RC6 Plus). The resulting pellet was then suspended in a cold solution of 0.2 M sucrose, 50 mM tricine, 3 mM KCl, and 3 mM $MgCl_2$ and centrifuged at 750 × g for one second. The supernatant was then filtered and centrifuged at 3000 × g for five minutes. The pellet was re-suspended in the same tricine buffer solution and centrifuged again at 3000 × g for an additional five minutes. The supernatant was decanted and pellets were concentrated in the tricine buffer solution at a chlorophyll (chl) concentration of ~25 mg/mL as determined using the method of Arnon.[32]

3.2.2 Solution Preparation

In a typical procedure, 10 mL of aqueous PEDOT solution (HC Starck, under the trade name Clevios P) was evaporated until it reached a solid form under vacuum at 35 °C, resulting in ~ 100 mg of solid material. This solid was then re-dispersed in 2.25 mL de-ionized H_2O by vortex mixing and magnetic stirring for at least one hour, followed by the addition of 2.5 mL ethanol. After the addition of 0.045 g of PEO (Acros, MW = 900,000 g/mol) to the dispersion, it was vigorously mixed by magnetic stirring for at least eight hours. PEO is added to the solution to assist in electrospun fiber formation. The motivation for concentrating the initial PEDOT solution was to increase the ratio of PEDOT/PEO which increases the overall electrical conductivity. Where appropriate one mL of the isolated thylakoid solution was added and allowed to stir into the polymer blend for 15 minutes prior to electrospinning. The thylakoid solution was increased to 1.513 mL for osmium tetroxide (OsO_4) stained samples used in TEM analysis. The stained thylakoid solution consisted of 0.5 mL of as-isolated thylakoid solution, 0.5 mL of 4 % paraformaldehyde (Acros) in 23 mM NaH_2PO_4/77 mM Na_2HPO_4 buffer, 13 μL of 8 % glutaric dialdehyde (Acros), and 0.5 mL 4 wt% OsO_4 (Acros). The solution was incubated for 30 minutes at 4 °C after the addition of the fixation agents to the thylakoids. This was followed by an additional 30 minute incubation period at 4 °C after OsO_4 was added to the solution. For fluorescence testing, a stock solution of Nile red dye (Acros) was made in acetone at 1 mg/mL and added to electrospinning solutions at a final dye concentration of 50 μg/mL. All solutions for light-induced pH measurements had an addition of $K_3[Fe(CN)_6]$ to a concentration of 0.3 mM for electron transfer purposes. Isolated thylakoid solutions and electrospinning solutions were used as-is (with the exception of the $K_3[Fe(CN)_6]$) while electrospun fibers were re-dissolved in the isolation buffer medium to a final volume of 10 mL.

3.2.3 Electrospinning

The electrospinning apparatus consisted of a high voltage power supply (Gamma High Voltage), a syringe pump (Stoelting Co.), a spinneret, and a 5 by 5 cm^2 aluminum collecting plate. Electrospinning solutions were fed into an 18 gauge blunt needle at a rate between 0.1 to 0.3 mL/hr. A positive voltage of 25 kV was applied between the spinneret and an aluminum collecting ground electrode separated by a distance of 20 cm. For electrical testing, fibers were collected on glass substrates with aluminum micropatterned electrodes separated by 100 μm. The glass substrate was placed on top of the aluminum collector. All electrospinning experiments were performed at room temperature.

3.2.4 Characterization

Light dependent current versus time (I-t) experiments and current versus voltage (I-V) sweeps were performed using a Hewlett Packard 4140B ammeter/DC voltage source with LabView data acquisition software using probe manipulators (Cascade Microtech Inc.) and a Schott ACE 1 halogen light source. All white light experiments were performed at a power density of ~13 mW/cm^2. When red (λ_p= 625 nm), green (520 nm), or purple (470 nm) filters were used, the power density was ~24, ~7, ~14 mW/cm^2, respectively. All electrical characterization was done in ambient conditions and repeated multiple times in order to ensure good reproducibility. Fiber morphology and thylakoid membrane inclusion were studied using a Phillips CM20 transmission electron microscope operating at 80 kV. Fluorescence imaging was done on a Nikon Eclipse Ti-U fluorescence inverted microscope using a Texas Red filter cube and analyzed using Image J program.[33] Light-induced pH measurements were done using a MeasureNet pH meter and data acquisition software (MeasureNet Technology, Ltd.). Ten μL of 0.1 N HCl was used to calibrate the change in proton concentration for each solution tested.

3.3 Results and Discussion

PEDOT/PEO fibers with and without the inclusion of thylakoids were electrospun onto micropatterned Al-electrodes with an electrode gap distance of 100 μm. (see inset, Figure 3.1). Light induced changes in electrical properties were then measured using the microprobe station shown in Figure 3.1. The light dependent I-V sweeps are shown in Figure 3.2 for PEDOT/PEO fibers without (Figure 3.2a) and with (Figure 3.2b) the inclusions of thylakoids. While care was taken to electrospin the same amount of solution for each experiment (200 μL), the location and distribution of the deposited fibers on the Al-patterned substrates inevitably changed to some degree from experiment to experiment. Therefore, the electrical current values for each experiment were normalized due to the different amounts of material collected between the electrodes. For fibers without thylakoids, there is a drop in electrical conductivity under white light illumination (compared to dark conditions) at higher voltages. This reduction in electrical conductivity is likely due to the degradation of PEDOT under light and the ambient testing conditions.[34,35] When thylakoids are added to the electrospun fibers, this trend is reversed, with slightly higher electrically conductivities reached under white light illumination.

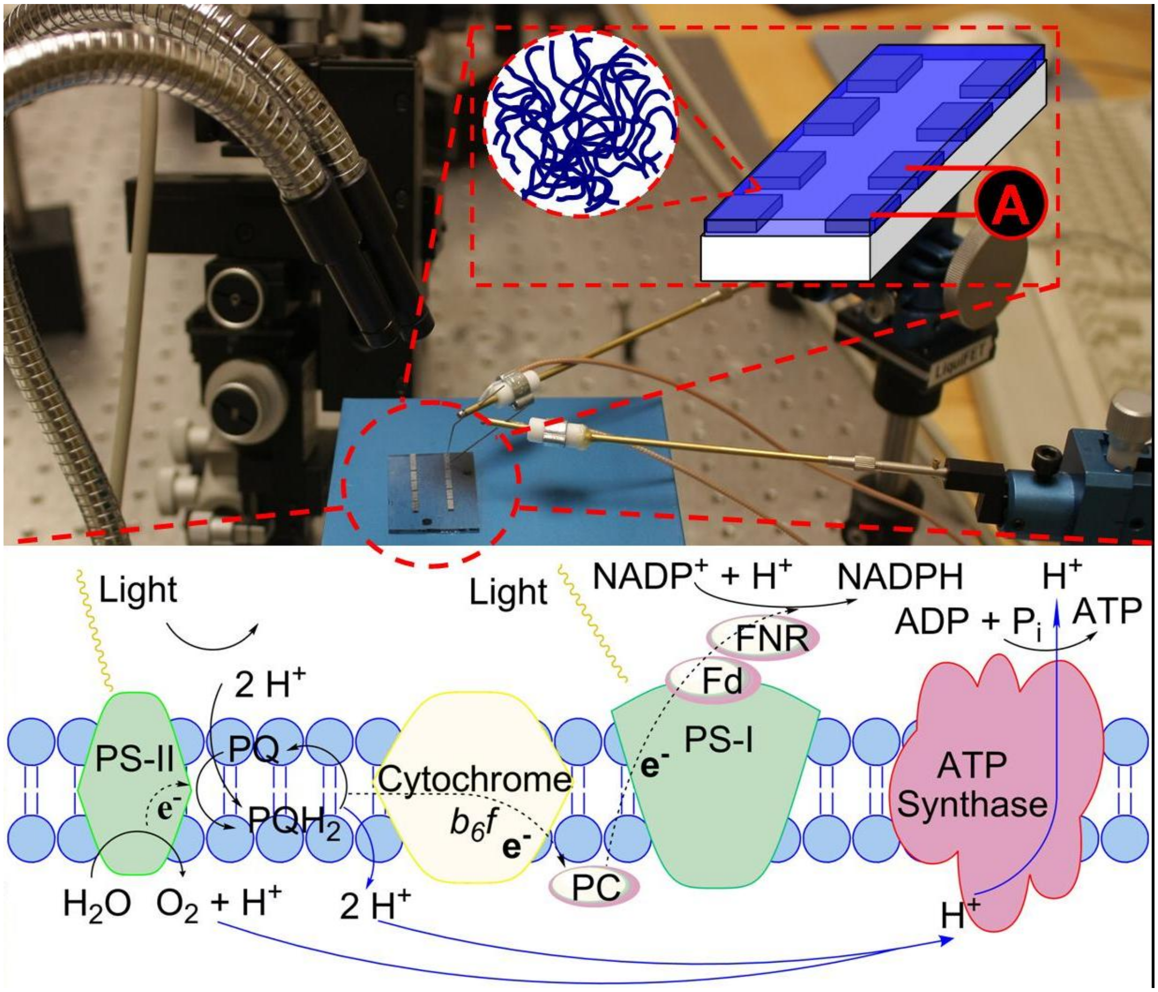

Figure 3.1. Photograph of the electrical testing experiment, with diagrams of the micro-patterned substrates and the light reactions of the photosynthesis within the thylakoids. Spacing between the electrodes is 100 μm. For reference: photosystem I (PS-I), photosystem II (PS-II), plastoquinone (PQ), reduced plastoquinone (PQH_2), plastocyanin (PC), ferredoxin (Fd), ferredoxin-NADP-reductase (FNR), adenosine diphosphate (ADP), adenosine triphosphate (ATP), phosphate (P_i). Proton movement is shown in blue solid lines and electron movement is shown in black, dashed lines.

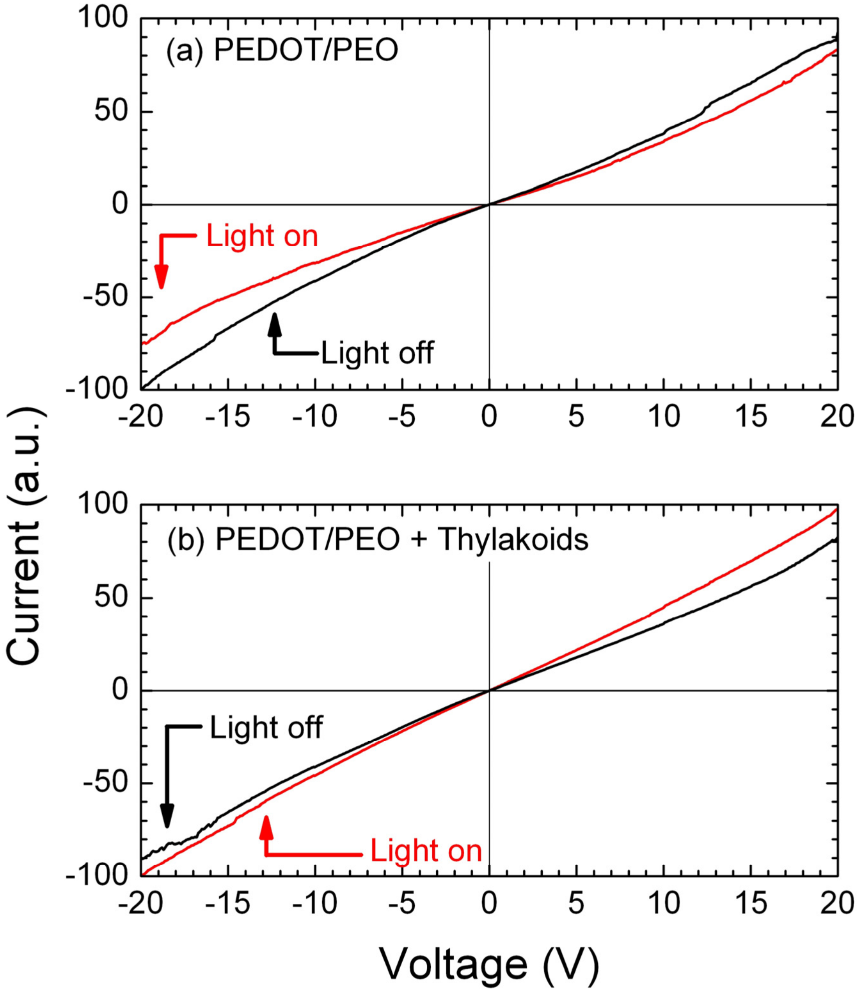

Figure 3.2. I-V sweeps of (a) PEDOT/PEO fibers and (b) PEDOT/PEO + thylakoid fibers under white light illumination.

The concentration of thylakoids in the electrospinning solution was varied to examine what affect the thylakoids had on the overall photocurrent (Figure 3.3). The normalized differences in photocurrent measured at the maximum voltage increases in a linear fashion with thylakoid concentration. The minimal thylakoid concentration needed to produce an increase in photocurrent was found to be ~ 2 mg/mL (in chlorophyll). The effect of power density on the photocurrent was also examined (Figure 3.3). Un-surprisingly, it was found that a larger power density produced a higher photocurrent response for each thylakoid concentration tested. At power densities lower than 1 mW/cm^2 it was discovered that the change in photocurrent to be negligible. Therefore, to produce a measurable photocurrent a power density higher than 1 mW/cm^2 must be used on fibers electrospun from a solution containing a chl concentration of at least 2 mg/mL. For reference, the changes in PEDOT/PEO fiber for both power densities tested are also shown in Figure 3.3.

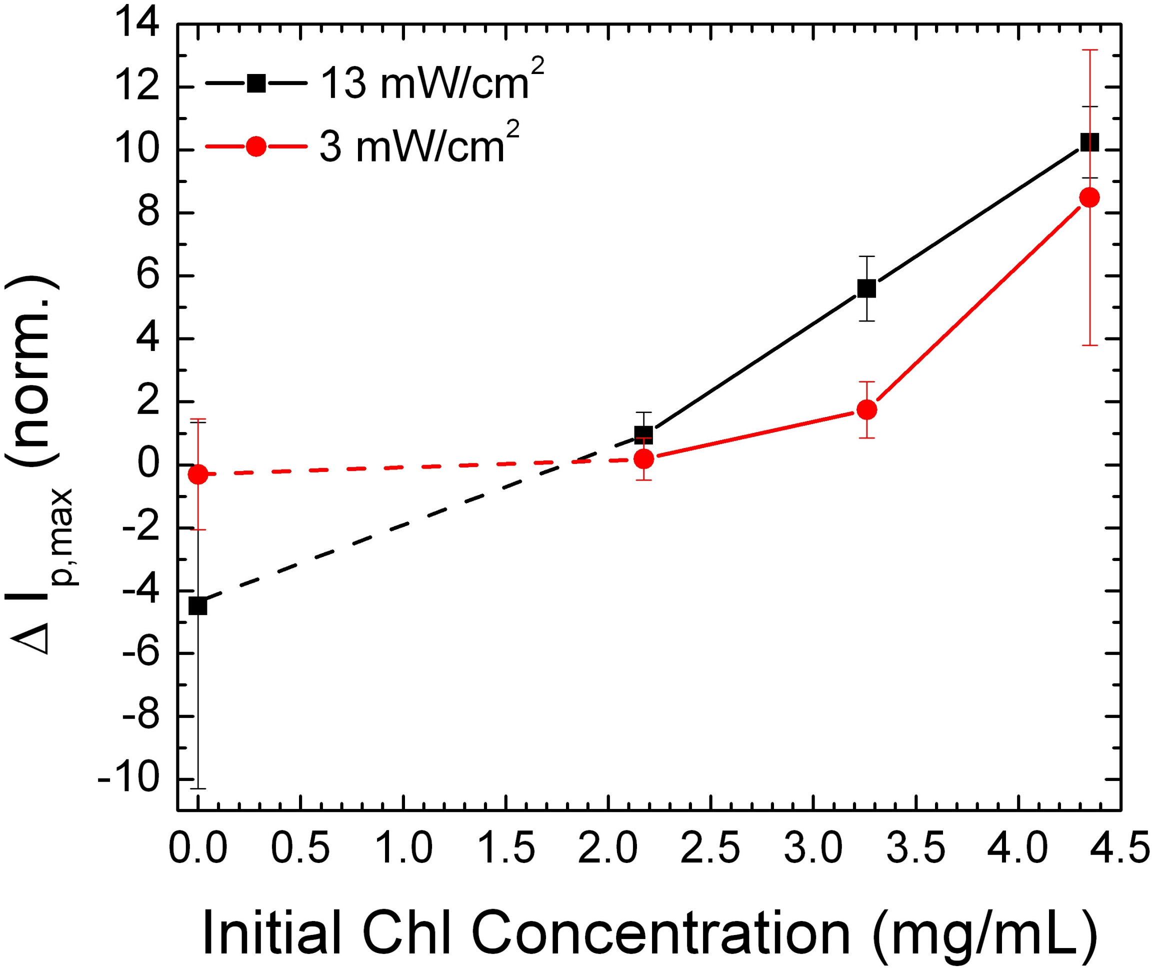

Figure 3.3. Maximum photocurrent vs. the initial chl concentration in solution for 13 mW/cm^2 (squares, black line) and 3 mW/cm^2 (circles, red line).

The electrical current response to a train of light pulses was evaluated for PEDOT/PEO fibers with and without thylakoids for several wavelengths regimes (Figure 3.4). The voltage was held at +5 V and light was pulsed on and off at three minute intervals (Figure 3.4, blue lines). PEDOT/PEO fibers with immobilized thylakoids display a slow increase in current when exposed to light and does not show an overall lost in current throughout the experiment (Figure 3.4a). Fibers without thylakoids show no marked changes in current coincident with light exposure; while an overall decrease in current is observed throughout the duration of the experiment. (Figure 3.4b). The wavelength dependence of the observed light induced current increases was tested for the PEDOT/PEO/thylakoid fibers (Figures 3.4c-3.4e). The wavelengths regimes selected correspond to the main absorption regions for chlorophyll-a and chlorophyll-b (red & purple) as well as a green wavelength region where the two chromophores do not absorb light.[36] As can be seen in Figures 3.4c-3.4e, light of all selected wavelength regions do not produce the same electrical response as does white light. Small current increases were observed at the moment of illumination. A general decrease of current was observed as the experiment progresses. The wavelength sensitivity can be attributed to the interplay between the distinct photosynthetic pigments during the energy transfer processes of photosynthesis *and* their corresponding absorption of light in the visible spectrum. For an electron to be given off in photosynthesis, light is first absorbed by various pigments in the antenna complexes within the photosystem. These pigments, each with their own absorption characteristics, transfer the excitation energy via fluorescence resonance energy transfer (FRET) to a pair of chlorophyll molecules, which then in turn produces a free electron. A loss of photon absorption by any pigment in the photosystem would then hinder the energy transfer process. This would then severely reduce the efficiency of generating a free electron and thus an increase in electrical current in the electrospun fibers is not achieved. This is analogous to the Emerson enhancement effect.[37] As such, these finding show that both the presence of thylakoids in the fibrous material and exposure to a white light source leads to current increases which are due to electrons ejected from photosystems embedded in the thylakoids.

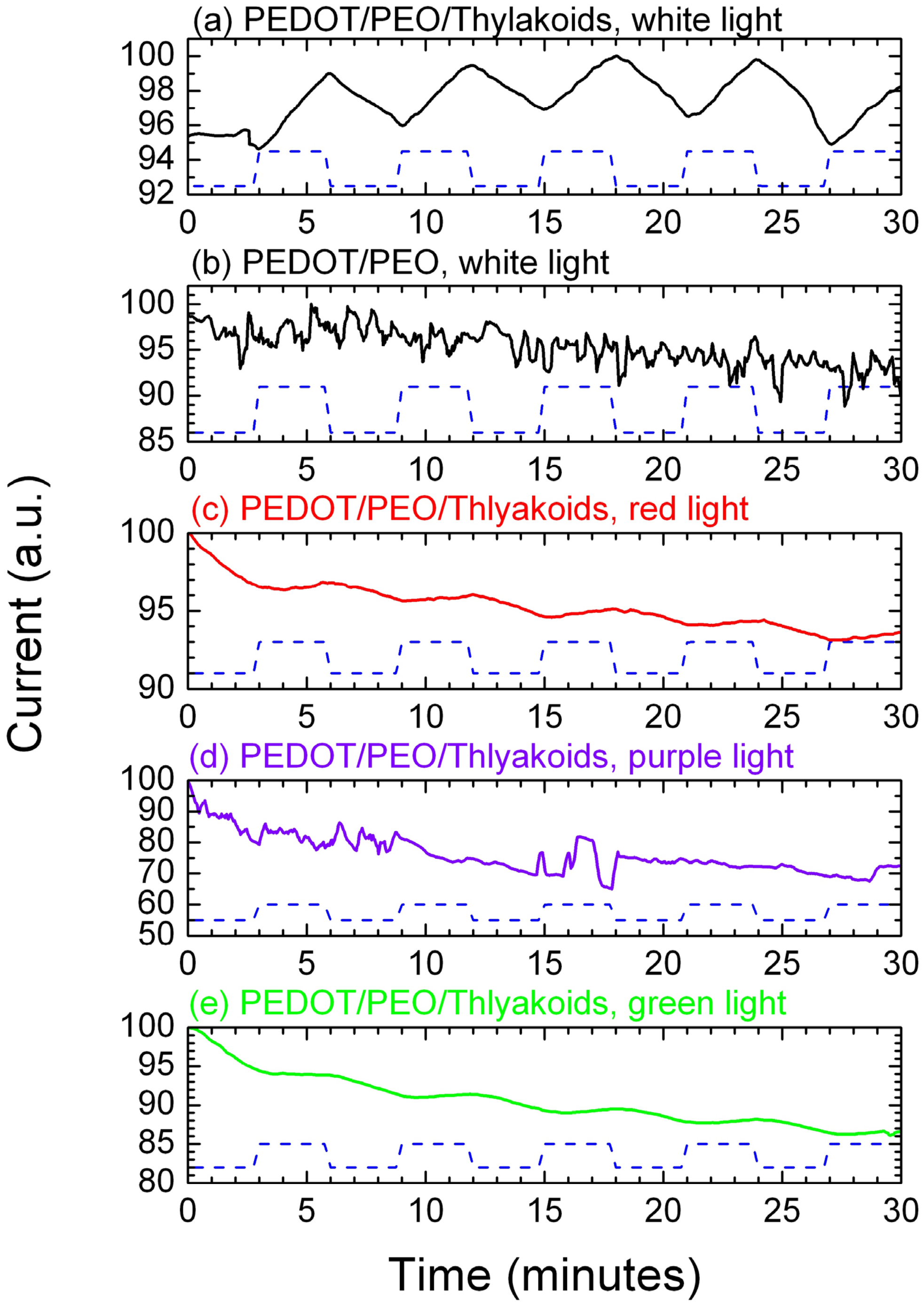

Figure 3.4. Current vs. time measurements with response to light for (a) PEDOT/PEO/thylakoid fibers under white light, (b) PEDOT/PEO fibers under white light, (c) PEDOT/PEO/thylakoid fibers under red light, (d) PEDOT/PEO/thylakoid fibers under purple light, and (e) PEDOT/PEO/thylakoid fibers under green light. The dashed line corresponds to light being on or off.

The PEDOT/PEO fiber morphology and immobilization of thylakoids into PEDOT/PEO fibers and was studied using TEM (Figure 3.5). The single PEDOT/PEO fiber shown in Figure 3.5a has a diameter of ~ 100 nm. With thylakoids added to the electrospinning solution, the resulting fiber diameter is approximately the same (Figure 3.5b) although a clear variation in contrast is present along the fiber. The ovular shapes are the immobilized thylakoids, as they are less dense then the polymeric fibers and thus exhibit a lighter shading in the TEM micrograph. Interestingly enough, the thylakoids tend to arrange themselves perpendicular to the fiber axis, a stark difference to how asymmetric particles arrange in electrospun fibers.[38,39,40,41] To confirm that these vesicles are indeed thylakoids, the lipid stain OsO_4 and fixation agents were added to the thylakoid solution prior to electrospinning, as mentioned in the experimental section (Figure 3.5c). The periphery of the vesicles is clearly darker in contrast with the addition of OsO_4, indicating that a lipid environment is present which is likely the structurally intact thylakoids. The density of the thylakoids in certain regions of the fibers also becomes higher due to the addition of cross-linking moieties in the stained thylakoid solution. The inclusion of the OsO_4 stained thylakoids has a drastic effect on electrospun fiber morphology, as the fibers become more beaded in nature and electrospraying becomes more prevalent. A single isolated thylakoid from the starting solution is shown in Figure 3.5d for reference.

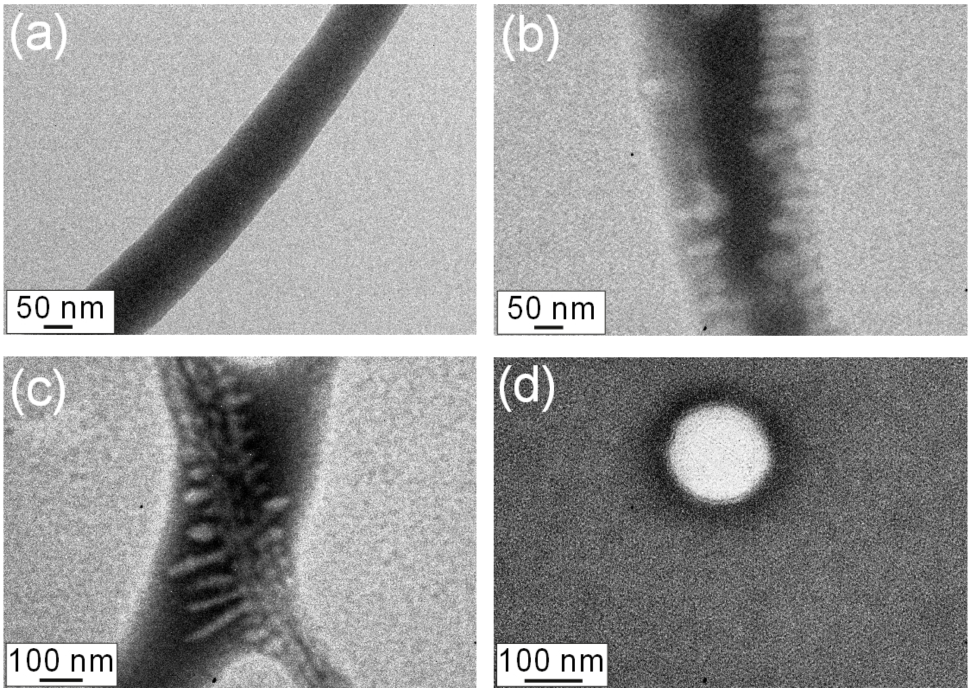

Figure 3.5. TEM micrographs of (a) PEDOT/PEO fibers, (b) PEDOT/PEO/thylakoids fibers, (c) PEDOT/PEO/thylakoid fibers + OsO_4 and fixing agents, and (d) an as isolated thylakoid vesicle.

To further investigate whether stable thylakoids were present in the electrospun PEDOT/PEO fibers, the lipid-specific dye Nile red[42] was added to the electrospinning solutions. Inverted fluorescent microscopy images of fibers with and without thylakoids are shown in Figure 3.6b and Figure 3.6d, respectively. Corresponding bright field images are shown in Figure 3.6a and Figure 3.6c. Comparing the images it is clear that the fluorescence is much higher in fibers where thylakoids were included in the electrospinning solution. Using grey-scale analysis the fluorescence of the PEDOT/PEO/thylakoid fibers is ~ 800 times higher than fibers without thylakoids for the same concentration of Nile red, indicating the presence of an ordered lipid environment within the fibers. Fiber diameters are larger here than in previous experiments due to the acetone present in the electrospinning solution (see Experimental section). The addition of acetone (solvent for Nile red) increases the overall volatility of the electrospinning solution, which has shown to increase fiber diameter in certain polymeric solutions.[43,44,45,46] Acetone is also a poor solvent for both PEDOT and PEO, resulting in overall morphology that includes a higher density of beaded fibers and electrosprayed globules.[47,48]

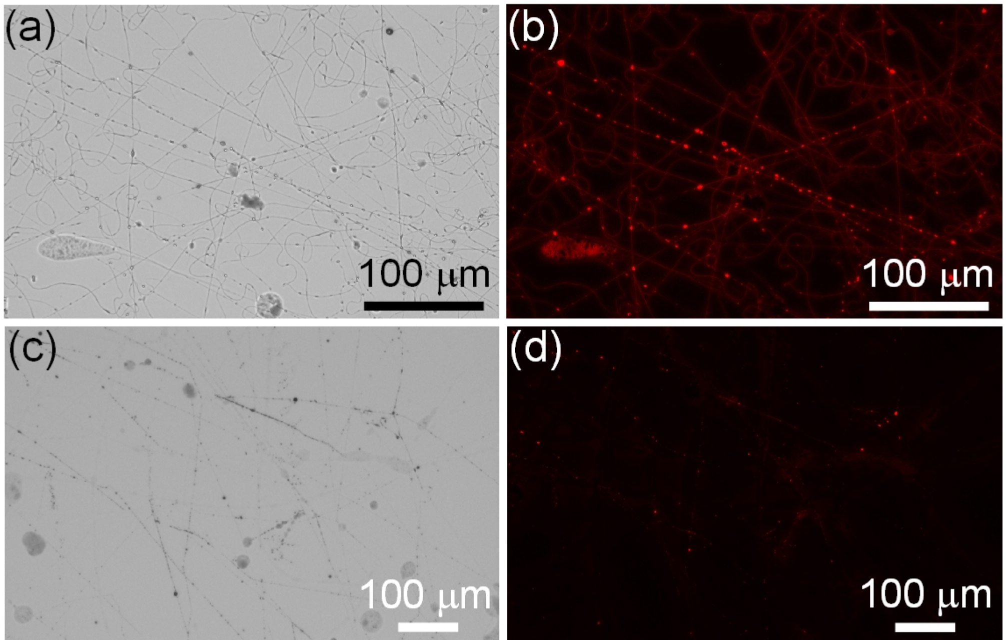

Figure 3.6. Bright field microscopy images of a) nile red stained PEDOT/PEO/thylakoid fibers and (c) nile red stained PEDOT/PEO fibers and fluorescent microscopy images of b) nile red stained PEDOT/PEO/thylakoid fibers and d) nile red stained PEDOT/PEO fibers taken with a Texas Red filter at 2 s exposure time.

White light driven proton gradient measurements were performed to probe the viability of the thylakoids through the electrospinning process. Thylakoids were tested after isolation (Figure 3.7a, green line), after being added to the PEDOT/PEO solution (Figure 3.7b black line), and re-dissolved following electrospinning, all with the addition of 0.3 mM $K_3[Fe(CN)_6]$ and with a pH of 2-2.25. An increase or decrease in the concentration of protons can yield information on the orientation of the thylakoids vesicles, namely whether the conformation is right-side-out or inside-out.[49] The isolated thylakoid solution shows a decrease in proton concentration with light (Figure 3.7a), indicating an uptake of protons from solution due to a majority right-side-out configuration. When thylakoid solution is mixed with PEDOT/PEO solution, a reversed and much larger change in proton concentration response to light is observed (Figure 3.7b). This increase in protons in solution is consistent with inside-out thylakoids.[50] The overall magnitude of the change in proton concentration between the as-isolated thylakoids and the PEDOT/PEO/thylakoid solution suggests that the PEDOT and/or PEO contributes to a configuration change of thylakoids from a mixture of inside-out and right-side-out vesicles to mainly inside-out vesicles. After the PEDOT/PEO/thylakoid solution was electrospun into fibers they were re-dissolved in the tricine buffer. The thylakoids in the re-dissolved solution were tested for their ability to establish light induced proton gradients. As seen in Figure 3.7c, the thylakoids still exhibit the ability to generate a proton gradient and show the same orientation as the electrospinning solution. The lower magnitude of the overall change in proton gradient is likely due to the lower percentage of thylakoids in the solution tested (~ 300 μL of solution electrospun re-dissolved in 10 mL tricine buffer) although a loss of thylakoid activity cannot be ruled out. However, the ability to establish light induced proton gradients illustrates that thylakoids are still active after the electrospinning process.

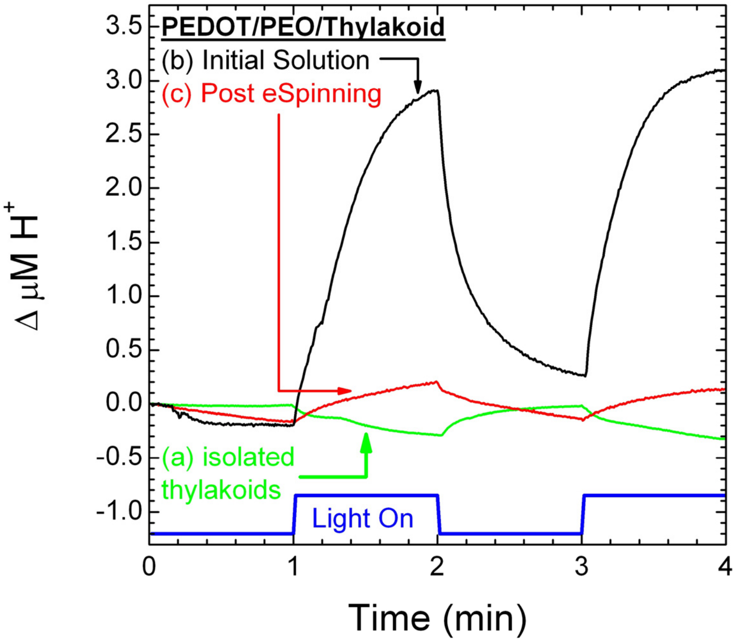

Figure 3.7. pH vs. time measurements with responses to light for (a) isolated thylakoid solution, (b) PEDOT/PEO/thylakoid electrospinning solution and (c) re-dispersed electrospun fibers in tricine buffer solution. Solutions were under white light illumination. The dashed line corresponds to light being on or off.

3.4 Conclusions

Thylakoid vesicles were successfully electrospun into nanofibers of PEDOT/PEO and show viability post-electrospinning. Due to the relatively high electrical conductivity of the polymer nanofiber, light induced electronic properties can be measured. The increase in electrical current of the PEDOT/PEO/thylakoid nanofibers due to exposure to light is likely caused by the still functioning light driven reactions of photosynthesis in the stable thylakoids. This photocurrent was found to increase linearly with thylakoid concentration. The presence of thylakoid environments within the fibers were verified by TEM and fluorescence microscopy with the lipid-specific stains OsO4 and Nile red, respectively. By measuring the light driven changes in pH in various thylakoid solutions, it was determined that thylakoids still have the ability produce proton gradients after the electrospinning process. This coupled with the fibers' ability to produce increases in electrical current upon white light illumination shows that the thylakoids survive the electrospinning process and still perform basic biological functions. The fluorescence and TEM experiments show the presence of stable lipid environments. These results represent a significant step toward incorporating photosynthetic biological function into an artificial system which may be used in optoelectronic applications.

---

[1] The bulk of this chapter appears in: N. M. Bedford, G. D. Winget, S. Punnamaraju, A. J. Steckl, *Biomacromoles*, **2011**, *12*, 778. Copyright the American Chemical Society, 2011.

[2] I. Wilner, E. Katz, *Bioelectronics*, Wiley-VCH Weinheim: Germany 2005

[3] L. Tiaz, E. Zeiger, *Plant Physiology 4th Edition*, Sinauer Associates, Inc., Publishers: Sunderland, MA, 2006.

[4] J.-J. Yun, H.-S Jung, S.-H. Kim, E.-M. Han, V. Vaithianathan, S. A. Jenekhe *Appl. Phys. Lett.* **87** (2005), 123102.

[5] X.-F. Wang, A. Matsuda, Y. Koyama, H. Nagae, S.I. Sasaki, H. Tamiaki, Y. Wada, *Chem. Phys. Lett.* **423** (2006), 470-475.

[6] Y. Amao, T. Komori, *Biosens. Bioelectron* **19** (2004), 843-847.

[7] X.-F. Wang, C.-H. Zhan, T. Maoka, Y. Wada, Y. Koyama, *Chem. Phys. Lett.* **447** (2007), 79-85.

[8] X.-F. Wang, H. Tamiaki, L. Wang, N. Tamai, O. Kitao, H. Zhou, S.-i. Sasaki, *Langmuir* **26** (2010), 6320-6327.

[9] R. Das, P. J. Kiley, M. Segal, J. Norville, A. A. Yu, L. Wang, S. A. Trammell, L. E. Reddick, R. Kumar, F. Stellacci, N. Lebedev, J. Schnur, B. D. Bruce, S. Zhang, M. Baldo, *Nano Lett.* **4** (2004), 1079-1083.

[10] Y. Lu, M. Yuan, Y. Liu, B. Tu, C. Xu, B. Liu, D. Zhao, J. Kong, *Langmuir* **21** (2005), *21*, 4071-4076.

[11] N. Lebedev, S. A. Trammell, A. Spano, E. Lukashev, I. Griva, J. Schnur, *J. Am. Chem. Soc.* **128** (2006), 12044-12045.

[12] L. Frolov, Y. Rosenwaks, C. Carmeli, I. Carmeli, *Adv. Mater.* **17** (2005), 2434-2437.

[13] N. Terasaki, N. Yamamoto, T. Hiraga, I. Sato, Y. Inoue, S. Yamada, *Thin Solid Films* **499** (2006), 153-156.

[14] I. Carmeli, L. Frolov, C. Carmeli, S. Richter, *J. Am. Chem. Soc.* **129** (2007), 12352-12353.

[15] L. Sepunaru, I. Tsimberov, L. Forolov, C. Carmeli, I. Carmeli, Y. Rosenwaks, *Nano Lett.* **9** (2009), 2751-2755.

[16] M. Miyachi,Y. Yamanoi, Y. Shibata, H. Matsumoto, K. Nakazato, M. Konno, K. Ito, Y. Inoue, H. Nishihara, *Chem. Comm.* **46** (2010), 2557-2559.

[17] M. T. Giardi, E. Pace, *Trends Biotechnol.* **23** (2005), 257-263.

[18] D. G. Varsamis, E. Touloupakis, P. Morlacchi, D. F. Ghanotakis, M. T. Giardi, D. C. Cullen, *Talanta* **77** (2008), 42-47.

[19] C. F. Meunier, P. Van Cutsem, Y.-U. Kwon, B.-L. Su, *J. Mater. Chem.* **19** (2009), 4131-4137.

[20] C. F. Meunier, P. Van Cutsem, Y.-U. Kwon, B.-L. Su, *J. Mater. Chem.* **19** (2009), 1535-1542.

---

[21] P. Euzet, M. T. Giardi, R. Rouillon, *Anal. Chim. Acta*. **539** (2005), 263-269.

[22] D. Li, Y. Xia, *Adv. Mater.* **16** (2004), 1151-1170.

[23] S. Agarwal, A. Greiner, J. H. Wendorff, *Adv. Funct. Mater.* **19** (2009), 2863-2879.

[24] A. Townsend-Nicholson, S. N. Jayasinghe, *Biomacromolecules* **7** (2006), 3364-3369.

[25] W. Salalha, J. Kuhn, Y. Dror, E. Zussman, *Nanotechnol.* **17** (2006), 4675-4861.

[26] M. Gensheimer, M. Becker, A. Brandis-Heep, J. H. Wendorff, R. K. Thauer, A. Greiner, *Adv. Mater.* **19** (2007), 2480-2482.

[27] S. Klein, J. Kuhn, R. Avrahami, S. Tarre, M. Beliavski, M. Green, E. Zussman, *Biomacromolecules* **10** (2009), 1751-1756.

[28] A. López-Rubio, E. Sanchez, Y. Sanz, J. M.Lagaron, *Biomacromolecules* **10** (2009), 2823-2829.

[29] S.-W. Lee, A. M. Belcher, *Nano Lett.* **4** (2004), 387-390.

[30] A. C. Patel, S. Li, J.-M. Yuan, Y. Wei, *Nano Lett.* **6** (2006), 1042-1046.

[31] S. Izawa, N. E. Good, *Plant Physiol.* **41** (1966), 533-543.

[32] D. Arnon, *Plant Physiol.* **24** (1942) 1-15.

[33] Available at: http://rsbweb.nih.gov/ij/

[34] S. Marciniak, X. Crispin, K. Uvdal, M. Trzcinski, J. Birgerson, L. Groenendaal, F. Louwet, W.R. Salaneck, *Synth. Met.* **141** (2004), 67-73.

[35] J.-S. Kim, P. K. H. Ho, C. E. Murphy, N. Baynes, R. H. Friend, *Adv. Mater.* **14** (2002), 206-209.

[36] H.R. Horton, L. A. Moran, K. G. Scrimgeour, M. D. Perry, J. D. Rawn, *Principles of Biochemistry 4th Edition* Pearson Prentice Hall: Upper Saddle River, NJ, 2006.

[37] R. Emerson, R. Chalmers, C. Cederstrand, *Proc. Nat. Acad. Sci.* **43** (1957), 133-143.

[38] H. Hou, J. J. Ge, J. Zeng, Q. Li, D. H. Reneker, A. Greiner, S. Z. D. Cheng, *Chem. Mater.* **17** (2005), 967-973.

[39] Q. Zhang, Z. Chang, M. Zhu, X. Mo, D. Chen, *Nanotechnol.* **18** (2007), 115611.

[40] M. Bashouti, W. Salalha, M. Brumer, E. Zussman, E. Lifshitz, *ChemPhysChem* **7** (2006), 102-106.

[41] G.-M. Kim, A. Sh Asran, G. H. Michler, P. Simon, J.-S. Kim, *Bioinsp. Biomim.* **3** (2008), 046003.

[42] P. Greenspan, E. P. Mayer, S. D. Fowler, *J. Cell Bio.* **100** (1985), 965-973.

[43] C. J. Thompson, G. C. Chase, A. L. Yarin, D. H. Reneker, *Polymer* **48** (2007), 6913-6922.

[44] S. Tungprapa, T. Puangparn, M. Weerasombut, I. Jangchud, P. Fakum, S. Semongkhol, C. Meechaisue, P. Supaphol, *Cellulose* **14** (2007), 563-575.

[45] M.-L. Cheng, C.-C. Lin, H.-L. Su, P.-Y. Chen, Y.-M. Sun, *Polymer* **49** (2008), 546.

[46] K. Yoon, B. S. Hsiao, B. Chu, *Polymer* **50** (2009), 2893-2899.

[47] S. L. Shenoy, W. D. Bates, G. Wnek, *Polymer* **46** (2005), 8990-9004.

[48] L. Buruaga, A. Gonzalez, J. J. Iruin, *J. Mater. Sci.* **44** (2009), 3186-3191.

[49] B. Andersson, C. Sundby, H.-E. Åkerlund, P.-Å. Albertsson, *Physiol. Plant.*, **65** (1985), 322-330.

[50] B. Andersson, H.-E. Åkerlund, P.-Å. Albertsson, *FEBS Lett.*, **77** (1977), 141-145.

Chapter 4:
Photocatalytic Self Cleaning Textile Fibers by Coaxial Electrospinning[1]

4.1 Introduction

Chemical degradation and self-cleaning by hydrophilic semiconductor photocatalysts, such as titania (TiO_2), have a wide range of applications including toxic chemical decomposition,[2,3,4] protective/self-cleaning clothing,[5] self-cleaning glass,[6] and self-cleaning membranes.[7] Photocatalytic activity is initiated when incident photons are absorbed by the photocatalyst creating excited electrons in the conduction band and holes in the valence band.[8] These electrons and holes lead to the formation of hydroxyl and oxygen radicals, which react with chemicals at the surface of the photocatalyst. Of particular note, chemically protective and self-cleaning clothing have obvious health, environmental, and military applications. Studies have been performed on titania treated textile materials, such as natural cotton,[5] chemically modified cotton[9], polyamide fibers[10], and chemically modified wool-like fibers.[11] The chemical modification performed increases the number of hydroxyl or carboxylic acid groups on the surface of the fiber, which have shown to adhere very well to titania.[8,10] In these studies the radiation used was often chosen to mimic the sun's spectrum at relatively high power densities. Typically, the UV component of the solar spectrum (200 nm to 400 nm) is responsible for photocatalytic activity. Somewhat surprisingly photocatalytic self-cleaning is rarely tested in light of longer wavelengths and lower intensities resembling typical indoor working conditions.

A major shortcoming of these treated textiles is the poor surface-to-volume ratio (SVR), limiting the overall photocatalytic activity. Electrospinning[12] has become an extremely versatile technique for the formation of fibers of various materials with applications including (but not limited to) tissue engineering[13], drug delivery[14], sensors[15], and superhydrophobicity[16,17]. To increase the SVR, electrospinning has been previously implemented to create non-woven fibrous TiO_2-based meshes by the electrospinning of a titania precursor followed by calcination[18] or using plasma treatment of electrospun fibers followed by repeated cycles of surface attachment of TiO_2 nanoparticles on the surface.[19] In these previous electrospinning reports the materials electrospun were not based on typical materials used for clothing/textile applications.

In this study, photocatalytic self-cleaning textile fibers with high SVR are created using the coaxial electrospinning method.[20,21,22,23] Cellulose acetate (CA) is used as the core phase which after a deacetylation step becomes cellulose. Cellulose, a biopolymer of consisting of β-1,4-glycosidic linked D-glucose units, is one of the most abundant naturally occurring materials and is commonly found in green plant cell walls and wood.[24] Cotton and cotton textiles contain as much as 90% cellulose. A dispersion of TiO_2 nanoparticles (here the Degussa P-25 mixture of titania phases) with and without a low concentration of CA is used as the sheath phase to disperse titania nanoparticles along the fibers' outer surface. The titania nanoparticles attach to the electrospun fiber in flight by adhesion to hydroxyl groups already present in the CA. A simple deacetylation step produces cellulose fibers. The coaxial electrospun fibers show self cleaning effects in *indoor* lighting conditions and outperform electrospun cellulose fibers surface loaded with TiO_2. While the vast majority of the light used in these experiments is above the considered cutoff wavelength of titania (~400 nm), photocatalytic activity is still observed due to titania's superior properties in charge-pair recombination lifetime, interfacial charge transfer rate, and near band gap light absorption.[8] In particular, mixed anatase/rutile phase titania (such as P-25) promotes stable charge separation because of unique charge trapping sites found between the two phases.[25,26] It has been shown that TiO_2 can photo-catalytically outperform materials with smaller band gaps at these wavelengths because of these superior properties.[27] Furthermore, exposure to acidic environments[28,29] and number of peripheral hydroxyl groups[30] have shown to increase photocatalytic activity. The photocatalytic fibers maintain their self cleaning properties after multiple staining and washing steps.

4.2 Experimental

4.2.1 Sample Preparation

Electrospinning solutions of CA were made to a concentration of 17 wt% in 80/20 acetic acid/water.[31] CA was added to the acetic acid solution and sonicated at low power until all the CA dissolved. For coaxial electrospinning, sheath solutions of TiO_2/CA were made at concentrations of 4 wt% TiO_2 and 2 wt% CA in 60/25/15 acetic acid/acetone/water by volume. The titania was added to a solution of acetic acid and water, sonicated at low power for two hours, followed by the addition of CA and acetone with another two hour low power sonication step. Sheath solutions of TiO_2 were made at 3 wt% in 85:15 acetic acid/water and sonicated for two hours. Solutions for surface loading of electrospun cellulose fibers with titania were made at 2 wt% in water and sonicated two hour prior to use. Aqueous Key Acid Blue solutions were made at a concentration of 0.1 wt% and aqueous sulforhodamine solutions were made at a concentration of 0.01 wt%. For x-ray diffraction (XRD) experiments samples of titania were dispersed in water or 85:15 acetic acid/water as described above, followed by solvent evaporation at 125 °C.

4.2.2 Electrospinning

The electrospinning apparatus (Figure 4.1) used a variable high voltage power supply (Glassman High Voltage). Solutions were pumped through an 18 gauge blunt needle for conventional electrospinning at a flow rate of 0.5-0.8 mL/hr using a syringe pump (Stoelting Co.). For coaxial electrospinning with a concentric nozzle (Nisco Engineering) solutions were pumped at a core flow rate of 0.5-0.8 mL/hr and a sheath flow rate of 0.05-0.3 mL/hr or 0.2-0.4 mL/hr for TiO_2 and TiO_2/CA solutions, respectively. When using a dispersion of titania as the sheath solution, it is important to note that the flow rate needs to be carefully monitored as electrospraying of titania occurs easily at higher flow rates. A positive voltage of 25 kV was applied between the spinneret and an aluminum collecting ground electrode separated by a distance of 11 cm. All electrospinning experiments were performed at room temperature.

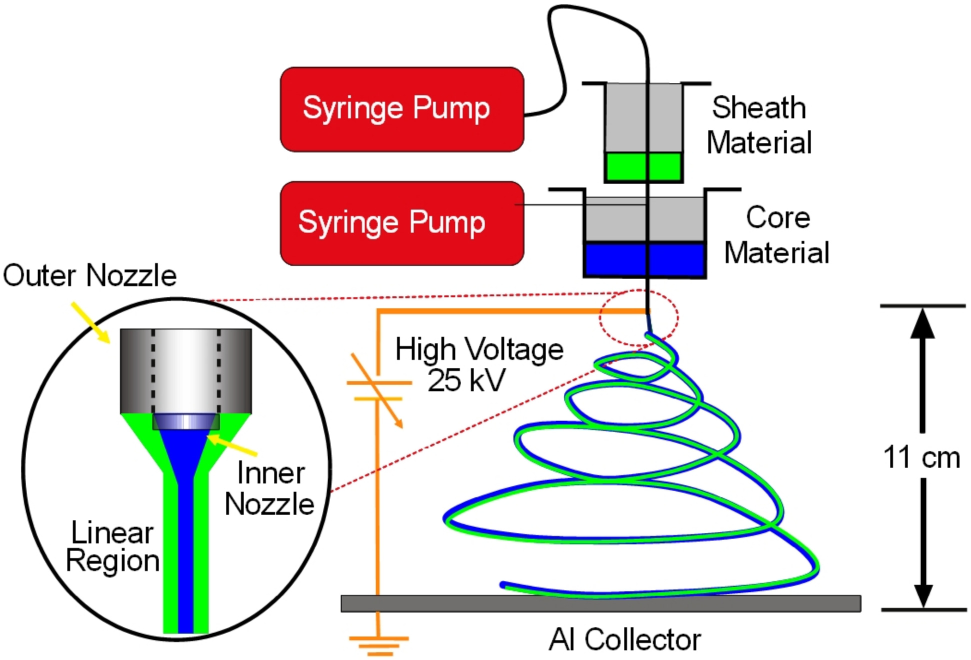

Figure 4.1. Schematic of coaxial electrospinning set-up. The inset shows an illustration of a coaxial droplet under applied voltage.

4.2.3 Deacetylation of CA

CA fiber mats were deacetylated in 0.5 N KOH in ethanol for 30 minutes at room temperature. After 30 minutes, the fiber mats were placed in 0.5 N aqueous HCl, followed by an excess of 0.5 N aqueous KOH. The fiber mats were back neutralized by 0.5 N aqueous HCl.

4.2.4 TiO_2 Loading

The TiO_2 nanoparticle surface loading treatment was adapted from Meilert *et al.*[8] Cellulose fiber mats were placed in 40 mL of aqueous 2 wt% TiO_2 solution for one hour at 75 °C. The loaded TiO_2-cellulose fiber mats were then dried at 100 °C for 30 minutes, followed by sonication in water for five minutes to remove any unbound titania.

4.2.5 Sample Washing

Samples were placed in a laundry detergent (3 wt%) solution under stirring for 1 hour, followed by 30 minutes of stirring in water. Samples were then dried in air at room temperature.

4.2.6 Titanium Assay

The titanium (Ti) assay is adapted from Sedaira et al.[32] Fiber samples (~ 10 mg) were dissolved in one mL of 50 % (w/v) ammonium sulfate in concentrated sulfuric acid at elevated temperature. 100 μL of the fiber solution was then added to 20 mL of 0.3125 % (w/v) 5-chlorosalicylic acid, 0.125 M $NaClO_4$ in 50:50 water/ethanol, adjusted to pH = 3 (± 0.1) with concentrated ammonium hydroxide, and diluted to 25 mL with water. The solution turned yellow, indicative of the formation of a Ti/5-chlorosalicylic acid complex. The quantification of Ti was performed by measuring the absorption of the solution at 355 nm. A standard solution of Ti was made by dissolving titania nanoparticles in 50 % (w/v) ammonium sulfate in concentrated sulfuric acid to a final concentration of 4 mg/ml at elevated temperature under reflux. The standard was added at varying volumes to the 5-chlorosalicyclic acid solution in a similar fashion as described above in order to obtain a calibration curve.

4.2.7 Characterization

Fiber morphology was studied using a FEI/Phillips XL30 field-emission environmental scanning electron microscope (FE-ESEM). The deacetylation process was confirmed with infrared (IR) spectroscopy using a Nicolet Nexus 870 FTIR spectrometer from Thermo Electron

Corporation in adsorption mode. A halogen light source was used at a power density of ~13 mW/cm^2 and ~27 mW/cm^2 for stain discoloration/decomposition experiments and UV-Vis characterization experiments, respectively. UV-Vis experiments were performed on a Perkin Elmer Lambda 900 UV/Vis/NIR spectrometer in absorption mode by measuring the absorption peak of Key Acid Blue at 628 nm. The cross section of photocatalytic electrospun fiber mats were analyzed using a JEOL 1230 Transmission Electron Microscope (TEM) operating at 80 kV. XRD patterns of titania samples were collected using a X'Pert Pro MPD x-ray diffractometer from PANalytical using Cu Kα_1 radiation.

4.3 Results and Discussion

The deacetylation of electrospun CA fibers is an established method to obtain cellulose nanofibers.[33,34,35] The reaction from CA to cellulose shown in Figure 4.2 was confirmed for the electrospun fibers by IR spectroscopy. The spectrum for CA (Figure 4.3, black line) contains the characteristic IR peaks associated with the acetyl group at 1745 cm^{-1} ($\nu_{C=O}$) and 1375 cm^{-1} (ν_{C-CH_3}). After 30 minutes of deacetylation, these peaks are absent from the IR spectrum (Figure 4.3, red line). Along with the significant increase in intensity for the C-OH peak at ~ 3500 cm^{-1}, this shows that the deacetylation process was successful and cellulose is obtained.[34]

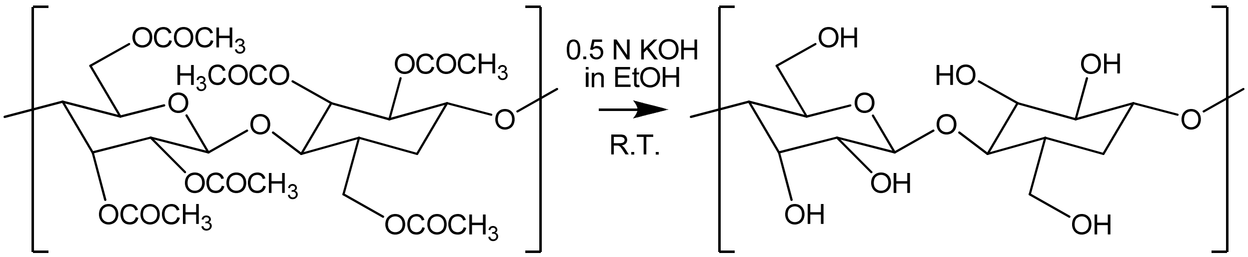

Figure 4.2. Reaction of cellulose acetate with 0.5 N KOH in EtOH.

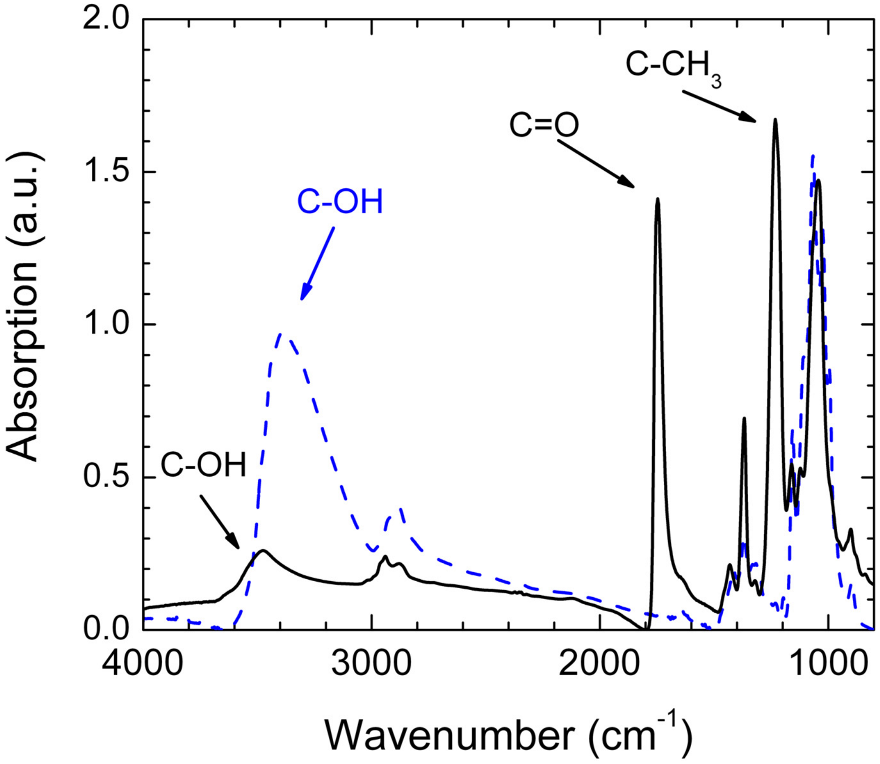

Figure 4.3. IR absorption spectrum of CA nanofibers (black, solid) and deacetylated cellulose (blue, dashed) fibers. Arrows indicate changing functional groups.

FE-SEM images of CA fibers and cellulose fibers are shown in Figures 4.4a and 4.4b, respectively. The CA fibers have diameters that range from 100-600 nm, with the diameter of the majority of fibers at ~ 250 nm. At the surface, the cellulose fibers appear to have been changed very little by deacetylation. The cellulose fibers have a similar diameter range, with the majority at ~ 200 nm, slightly smaller than the parent CA fibers. During deacetylation, acetyl groups are replaced by hydroxyl groups, changing from ~ 60% hydroxyl content of CA from manufacturer to nearly 100% hydroxyl content (Figure 4.3). This greatly increases the likelihood of hydrogen bonding in the fiber structure. Hydrogen bonding is known to play a crucial role in the structure of cellulose[36], and is the main reason for its low solubility in most solvents systems. The increase in secondary bonding within the structure and crystallographic differences between hydroxylated and acetylated cellulose[37,38] are likely causes for the change in fiber diameter and morphology.

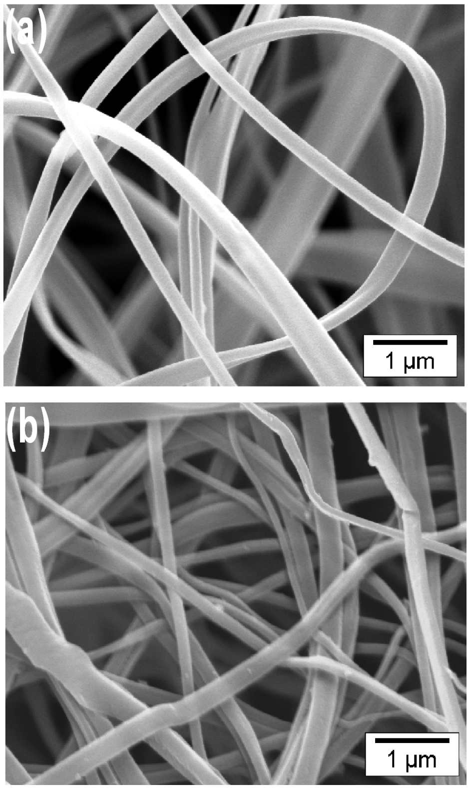

Figure 4.4. SEM microphotographs of nanofibers formed by conventional electrospinning: (a) as-spun CA; (b) post-deacetylation cellulose. (20kx magnification).

The morphology of cellulose-titania electrospun fibers using a coaxial nozzle was studied using FE-SEM. Selected examples indicative of important features are illustrated in the photomicrographs of Figure 4.5. Fibers electrospun with a blended TiO_2/CA sheath solution are shown in Figure 4.5a before deacetylation and in Figure 4.5b after deacetylation. Morphological differences between fibers created from conventional and coaxial nozzle configurations (Figure 4.4 vs. Figure 4.5a) are clearly apparent. Asymmetrical and concave-like beads are formed and the fiber diameters are mostly around ~200 nm, with no fibers of diameters higher than ~300 nm being observed. The overall fiber thinning can be attributed to bead formation as the beads consume more polymer, reducing the amount available for fiber formation. This bead formation is not observed with conventionally electrospun CA nanofibers. Beads could be attributed to CA-TiO_2 clustering in solution as the titania binds to the CA. TiO_2 nanoparticles in clusters of varying sizes are observed adhering to fibers and within the beaded sections. Upon deacetylation seminal morphological changes occur: beaded regions disappear, the average fiber diameter increases, and titania coverage appears more widespread. A migration of nanoparticles during deacetylation could contribute to this effect since the TiO_2 nanoparticles would bind to the deacetylating solvent as well, which would allow for their diffusion through the deacetylating medium. Another possible explanation could be polymer chain rearrangement during deacetylation leading to the uncovering of previously embedded nanoparticles.

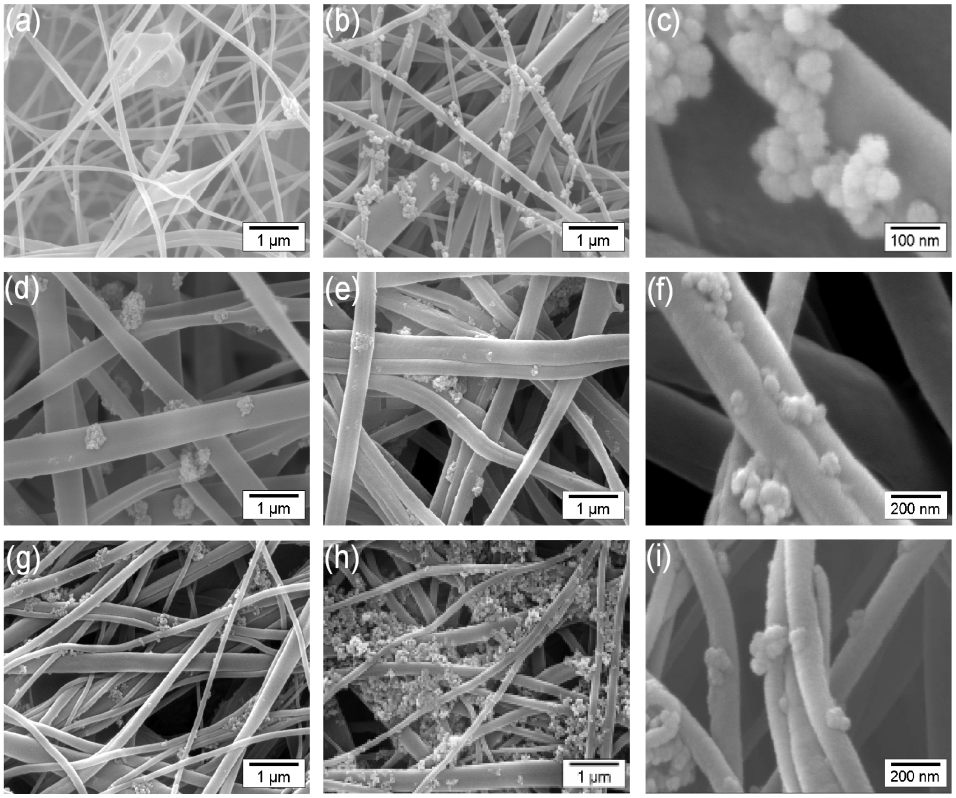

Figure 4.5. SEM microphotographs of TiO_2-containing nanofibers formed by coaxial electrospinning. CA (core) - TiO_2/CA (sheath): (a) as-spun; (b) (c) post- deacetylation cellulose;CA (core) - TiO_2 (sheath): (d) as-spun; (e) (f) post- deacetylation cellulose;); Post-deacetylated cellulose fibers surface loaded with TiO_2: (g) (h) (i).

Fibers electrospun with a dispersion of TiO_2 as a sheath solution are shown Figure 4.5d (before deacetylation) and Figures 4.5e (after deacetylation). Unlike the previous case, fiber diameter and morphologies remain relatively unchanged upon deacetylation. Prior to deacetylation, titania appears mostly in aggregated clusters along the fibers, while the size and number of aggregates decrease after deacetylation. As for the case of TiO_2/CA sheath fibers, this could be attributed to nanoparticles migration in the deacetylating medium. Cellulose nanofibers *surface loaded* with TiO_2 are shown in Figures 4.5g and 4.5h. Fiber diameter and morphology are comparable to cellulose (core) – TiO_2 (sheath) fibers, but the titania distribution varies greatly across the fiber mat. It is worth noting that the hydroxyl functionality in the cellulose fibers does not bind titania as well as carboxylic acid modified cellulose, which more uniformly binds TiO_2. As such, the latter is often used because of its advantageous titania binding ability.[9,11,39] High magnification SEM micrographs are shown in Figures 4.5c, 4.5f, & 4.5i to better display the titania nanoparticle clusters formed on cellulose fibers with various techniques. TEM cross sections are shown in Figure 4.6 for the fibers made by coaxial electrospinning and surface loading techniques. Due to the similar elemental composition of the epoxy used for casting and the cellulose nanofibers, contrast between the two materials is very low. In general, clusters of titania are seen throughout the cross section of the fiber mats for both samples. At higher magnifications the amount, distribution, and density of titania appears similar for samples made by coaxial electrospinning (Figure 4.6a) and surface loading (Figure 4.6c) methods. However, at lower magnification it is clearly seen that the fibers made by coaxial electrospinning have a better titania distribution in the cross section compared to the more aggregated titania seen in samples made by surface loading (Figures 4.6b and 4.6d).

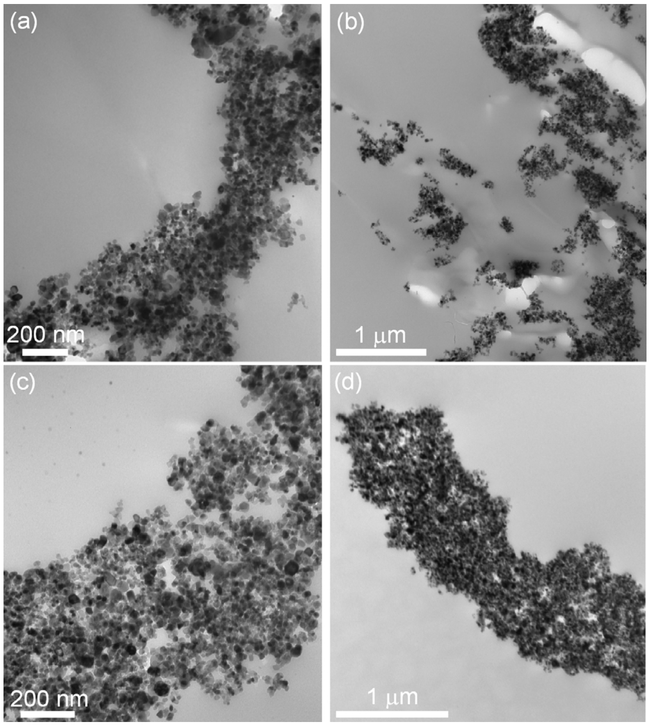

Figure 4.6. TEM cross section microphotographs of cellulose (core) – TiO_2 (sheath) fiber mats (Figure 3a and Figure 3b) and cellulose fibers surface loaded with TiO_2 (Figure 3c and Figure 3d).

The photodegradation properties of the electrospun fibers were initially examined by testing the decomposition of a blue dye solution under halogen lamp irradiation. Halogen lighting is used because it better resembles indoor lighting conditions and represents the lower level of achievable photocatalytic activity. The halogen lamp emission spectrum is shown in Figure 4.7 along with the absorption spectrum of TiO_2 nanoparticles. The halogen lamp emits a very low number of photons in the UV range compared to visible range photons. As expected, the absorption of the TiO_2 measured from the electrospun cellulose fibers is mainly in the UV region, with a small amount of peak extending into the visible range. The photocatalytic properties of titania allows for the small amount of near band gap light to be effectively used in molecular decomposition.

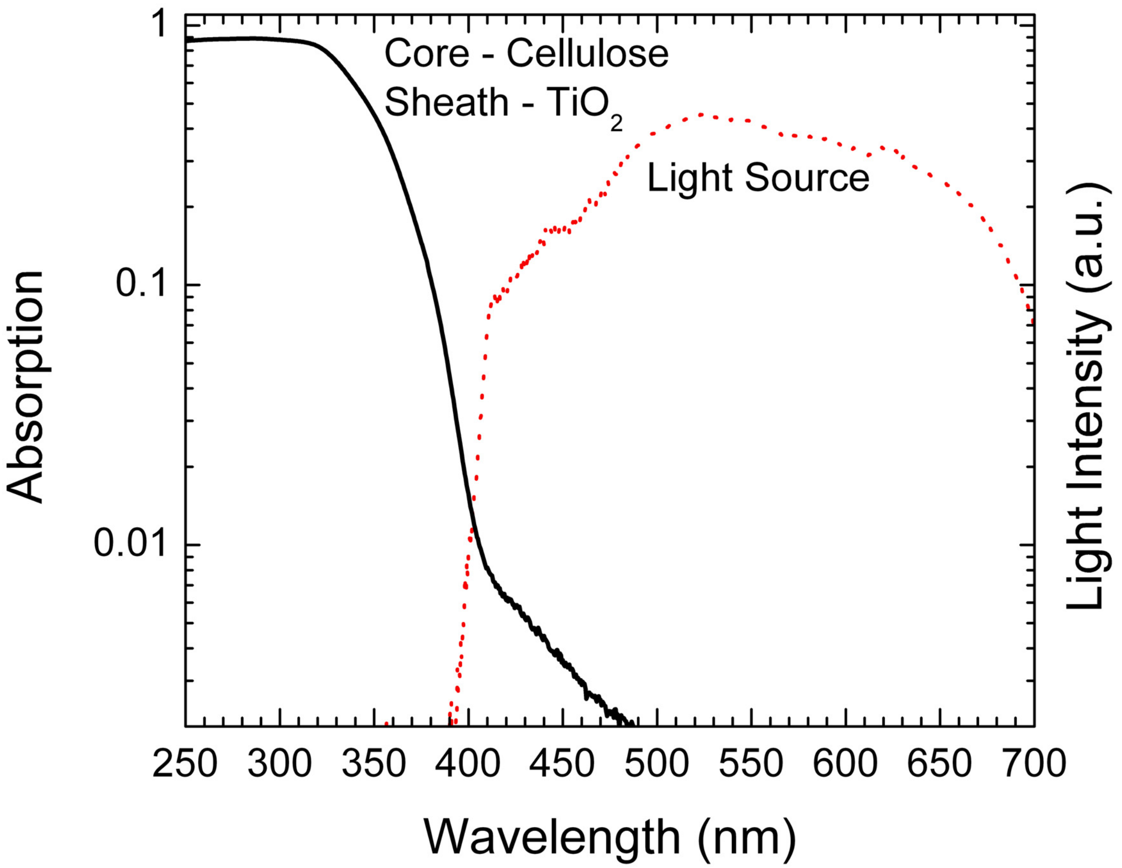

Figure 4.7. Optical spectra relevant to the self-cleaning process: TiO_2 nanoparticle absorption and halogen lamp emission.

Figure 4.8 contains photographs illustrating the decomposition over a period of 24 hours of KeyAcid Blue dye solutions by plain cellulose nanofibers, TiO_2 surface loaded cellulose nanofibers, cellulose (core) – TiO_2/cellulose blend (sheath) nanofibers, and cellulose (core) – TiO_2 (sheath) nanofibers under halogen illumination at a power density of ~13 mW/cm^2. The cellulose nanofiber mat shows a slow discoloration with time and is used for reference. Titania surface loaded fibers do show photocatalytic activity. However, this type of fiber mat does not show full discoloration over the entire stained area. Fibers made using the coaxial nozzle with a TiO_2/cellulose blended sheath show little degradation despite the appearance of nanoparticles on the exterior of the fibers (Figure 4.5b). It is conceivable that the titania is covered in a thin layer of cellulose since the nanoparticles were initially in a solution with a partially hydroxyl functionalized polymer. This would then impede free radical generation and slow the self-cleaning process. Cellulose (core) – TiO_2 (sheath) fibers display the best self-cleaning characteristics as the blue dye solution is almost completely eliminated throughout the entire stain region after 24 hours. For comparison, a mat of un-reacted CA (core) – TiO_2 (sheath) fibers was stained using 0.1 wt% blue dye solution (Figure 4.9). While the amount of dye is not fully degraded over the 24 hour period, the fibers do exhibit significant photocatalytic activity. The intense initial dye color is due to the lower wettability of the CA fibers. This shows that the catalytic properties of titania are largely unaffected by the deacetylation process.

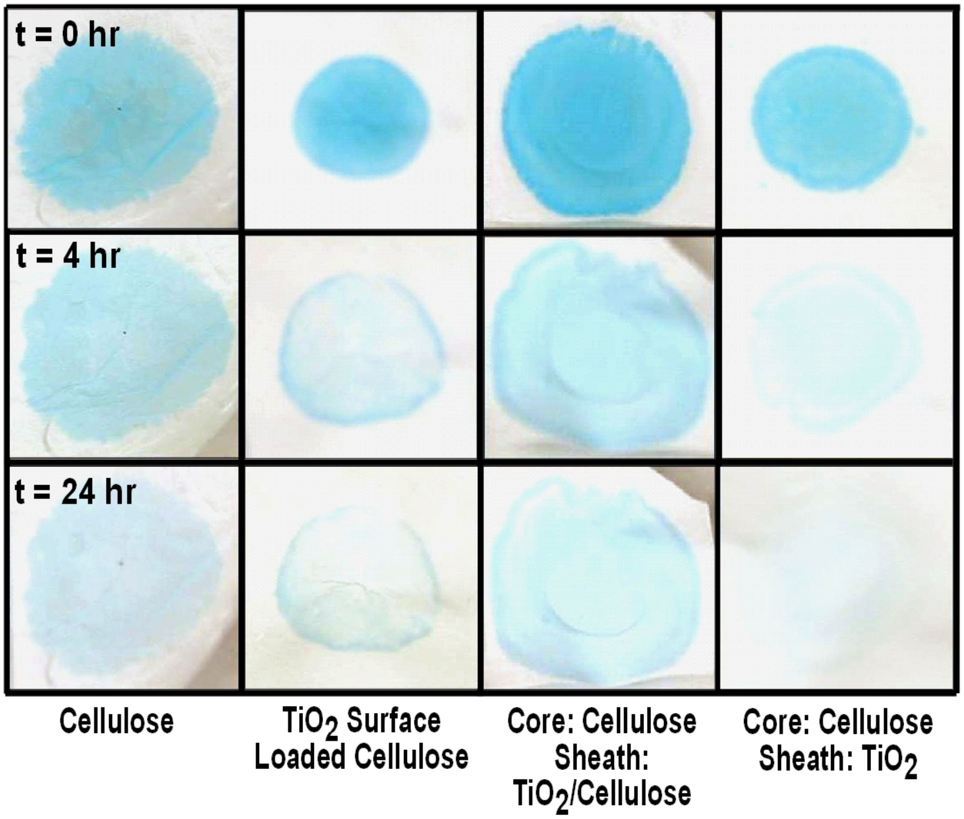

Figure 4.8. Photographs showing the discoloration of Keyacid Blue (0.1 wt%) stain in electrospun non-woven mats exposed to halogen light (~13 mW/cm2) over a 24 hour period: (a) cellulose nanofibers; (b) TiO_2 surface loaded cellulose nanofibers; (c) cellulose (core) - TiO_2/cellulose (sheath) nanofibers; (d) cellulose (core) - TiO_2 (sheath) nanofibers.

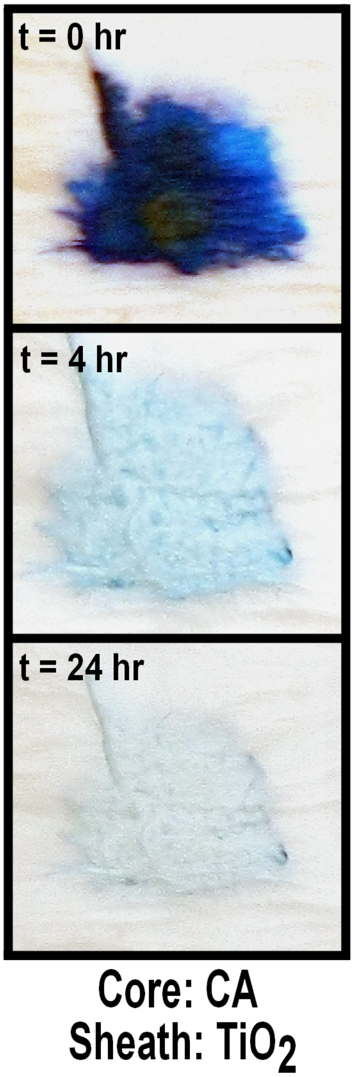

Figure 4.9. Photographs showing the discoloration of Keyacid Blue (0.1 wt%) stain in coaxial electrospun non-woven mats of CA (core) – TiO_2 (sheath) fibers exposed to halogen light (~13 mW/cm2) over a 24 hour period.

Optical absorption of the fiber mats as a function of time is used to provide a quantitative evaluation of the decrease in KeyAcid Blue dye concentration due the self-cleaning activity of various nanofibers. The results are shown in Figure 4.10. In these experiments, the concentration is normalized to the value at time equal to zero and the illuminator power density was ~27 mW/cm^2. It is assumed that to a first order approximation the dye absorption in the fiber is linearly proportional to its concentration. The plain cellulose fibers show a nearly linear reduction in the dye absorption with time. After ten hours of halogen lamp exposure the fiber mat has reduced its dye concentration by ~30%, corresponding to a dye decomposition rate of 6.7×10^{-6} mM/min. All of the TiO_2-containing nanofibers exhibited a two-mode discoloration pattern, consisting of a rapid initial decay for the first one to two hours followed by a more slowly time-varying component. As observed qualitatively in the photographs of Figure 4.8, nanofibers with a blended TiO_2/cellulose sheath phase show slightly stronger chemical degradation than the pure cellulose nanofibers, reaching a 50% concentration after ten hours with an exponential decomposition rate constant of 4.5×10^{-6} mM/min. The cellulose (core) – TiO_2 (sheath) nanofibers decompose the dye molecules more quickly than the blended sheath nanofibers reaching a rate constant of 1.8×10^{-5} mM/min. In this case, the photocatalytic process is able to reach 100% dye decomposition (in ~7 hours). The surface loaded nanofibers exhibit a quick degradation to ~20% of the initial dye concentration in less than one hour, followed by a very slow concentration decay for the remainder of the exposure time (~9 hours). The equivalent exponential decay rate constant of 6.1×10^{-5} mM/min is the fastest in the initial time regime. However, unlike the coaxial fibers the surface loaded photocatalytic process only reaches a maximum of 80% dye decomposition. The chemical decomposition characteristics of the coaxial electrospun derived and surface loaded fiber mats are consistent with the amount of TiO_2 in each mat and with the method of its incorporation. The surface loaded mat is likely to have a non uniform TiO_2 concentration with the highest value near the top surface of the mat. This would result in faster initial decay, but because of the lower total amount of titania the ultimate decomposition will not be as complete as for the fiber mat made using coaxial electrospinning.

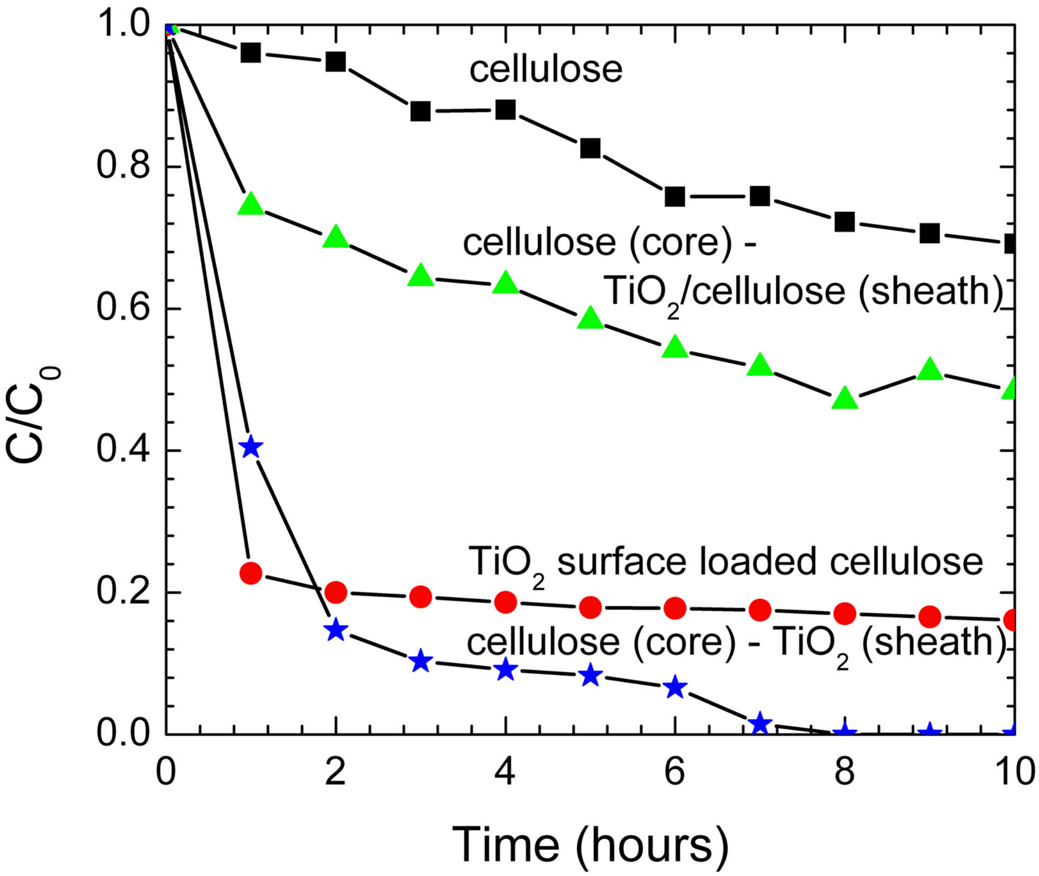

Figure 4.10. Concentration of Keyacid Blue (0.1 wt%) in electrospun non-woven mats exposed to halogen light (~27 mW/cm^2) as a function of time: cellulose nanofibers (black squares), cellulose (core) - TiO_2/cellulose (sheath) nanofibers (green triangles), TiO_2 surface loaded cellulose nanofibers (red circles), cellulose (core) - TiO_2 (sheath) nanofibers (blue stars).

Initially, the surface density of dye molecules on the surface of the fiber mats for each sample is ~3.8 × 10^{15} dye molecules/cm^2, while the total flux of photons on the surface is ~1.9 × 10^{21} photons/cm^2 for the complete decomposition of the dye in the cellulose (core) –TiO_2 (sheath) example. This corresponds to one dye molecule decomposing for every 5 × 10^5 photons. Clearly, this vast majority of photons are not utilized in the decomposition process because of the very low absorption in the visible range. However, the coaxial electrospinning method allows for a larger quantity of TiO_2 to be embedded into the nonwoven mat, leading to the full decomposition of the dye molecules in seven to eight hours. It is anticipated that using N- and/or

F-doped TiO_2 which has a lower bandgap[40] will reduce the total decomposition from hours to minutes.

Ti assay and XRD experiments were performed in order to better understand the photocatalytic properties of the fiber mats made by coaxial electrospinning and by surface loading techniques. The Ti assay is used to quantify the amount of titania present in the fiber mats. From Figure 4.11, the concentration of Ti in the surface loaded fibers in solution is 0.017 ± 0.006 mM, whereas the solution from the fiber mats made by coaxial electrospinning is 0.011 ± 0.006 mM. This corresponds to a titania/fiber mat percentage of 3.4 and 2.2 ± 0.5%, respectively, indicating that the amount of titania in the surface loaded electrospun fibers mats is slightly larger compared to the fibers made by coaxial electrospinning. To determine any crystallographic differences between the titania in the surface loaded and coaxial electrospun fiber mats, titania nanoparticle dispersions were made in a similar fashion as used for coaxial electrospinning (85% acetic acid solution) and for surface loading (aqueous solution), followed by the removal of the solvent. In the perspective of the whole diffraction pattern it appears the patterns are identical (Figure 4.12), exhibiting all the characteristic peaks for P-25 titania. However, upon closer inspection (inset, Figure 4.12) it becomes clear that the crystallite size for the nanoparticles treated in water (surface loaded fibers) is larger than those treated in 85% acetic acid (coaxial electrospun fibers). Using the Scherrer equation,[41] it was estimated that the crystallite size for water and 85% acetic acid treated samples are 17.4 ± 0.9 nm, and 14.8 ± 0.5 nm respectively. A decrease in crystallite size is known to increase photocatalytic activity,[42] while differences in crystallite sizes have been observed in titania films cast in different solvents following sonication.[43] Despite the slightly larger amount of titania measured in the photocatalytic fiber mats made by surface loading techniques, the fibers made by coaxial electrospinning exhibit a more complete photocatalytic degradation of the analytes tested. This can be attributed to the higher uniformity of the titania along the fibers and within the fiber mats compared to surface loading methods (Figure 4.5e vs. Figure 4.5g and Figure 4.5h; Figure 4.6b vs. Figure 4.6d) and to the smaller crystallite size titania present in the coaxial electrospun fibers.

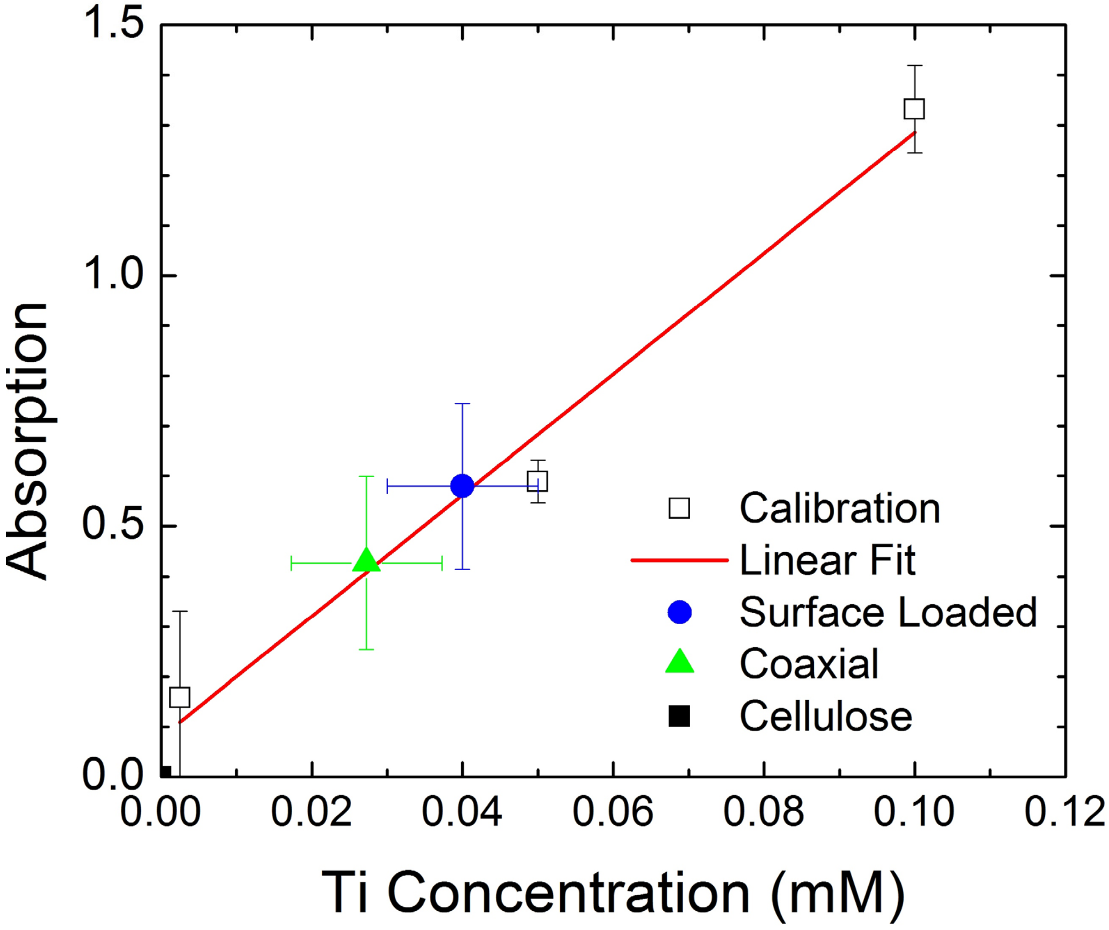

Figure 4.11. Absorption at 355 nm of Ti from the Ti/5-chlorosalicylic acid as a function of Ti in solution: cellulose nanofibers (solid black square), cellulose (core) - TiO_2/cellulose (sheath) nanofibers (solid green triangle), TiO_2 surface loaded cellulose nanofibers (solid blue circle). Calibration curve (red) calculated from black squares, $R^2 = 0.969$.

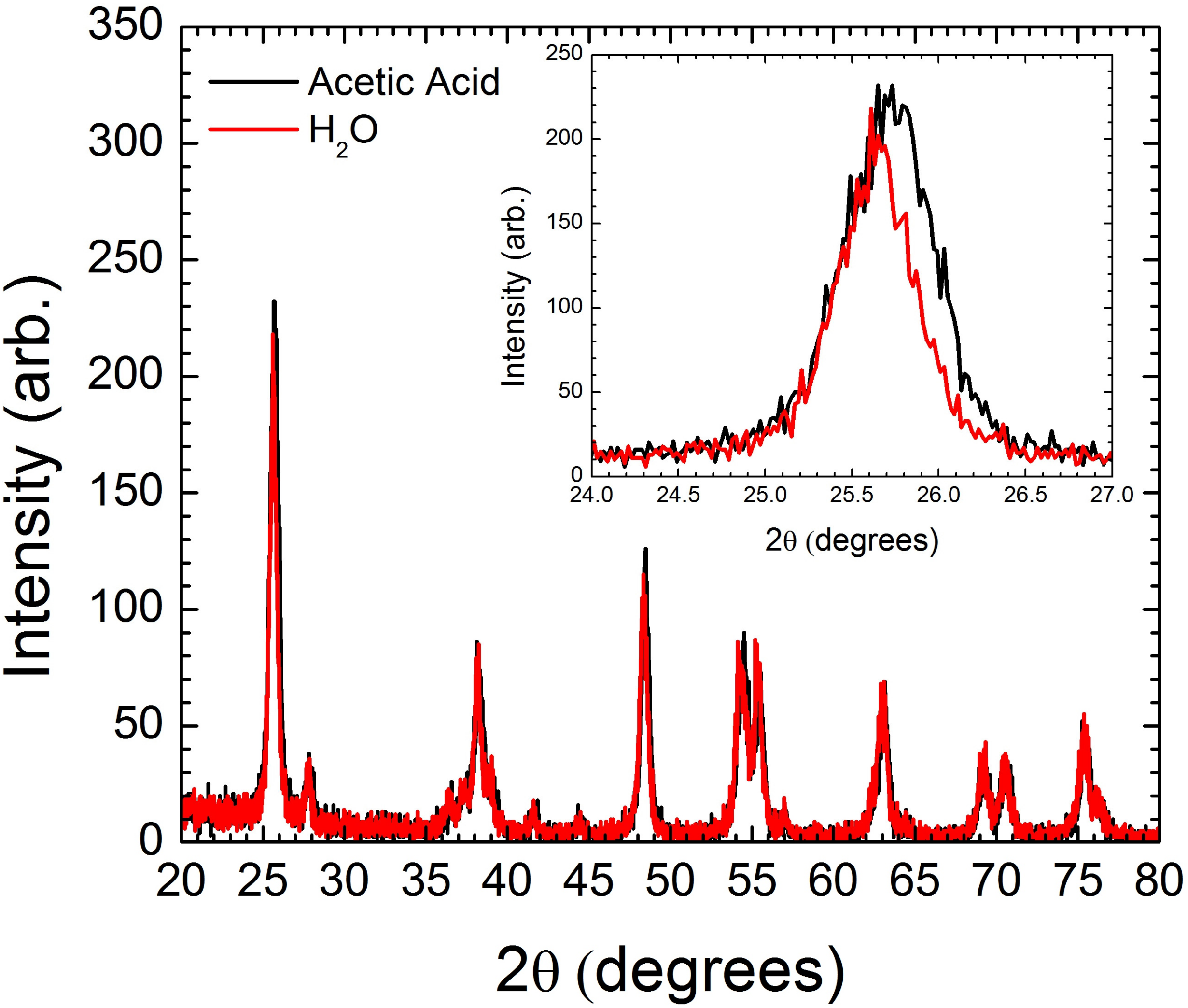

Figure 4.12. XRD patterns from P-25 titania cast from H_2O (red line) and 85:15 acetic acid/H_2O (black line). Inset shows largest anatase peak at ~25.7° 2θ.

To study both the durability and safety of the photocatalytic cellulose nanofibers, longevity tests were performed to determine the multiple-use performance and adherence of the titania to the nanofibers, as the safety of nanoscale TiO_2 has come into question.[44,45] Photographs of the fiber mat at different stages of the process are shown in Figure 4.13. Using the same lighting conditions as the experiments described in Figure 4.8, the electrospun fibers made by coaxial electrospinning with a titania sheath were first stained with the KeyAcid Blue dye solution, and then exposed to halogen irradiation to obtain self-cleaning though photodegradation.

After 24 hours, the same sample was re-stained with a sulforhodamine dye solution. Within the next 24 hours the stain is again nearly 100% removed from the sample by photodegradation. This sample was stained a 3rd time with red wine, again becoming discolored within 24 hours. The sample was next washed (using the procedure described in the experimental section) after which the sample was completely white. An increased amount (2x) of red wine was used for the 4th staining of the sample, and a similar discoloration is observed once again. Following a second washing step, an even larger amount of red wine was used for the 5th and final staining (four times the initial red wine staining), fully saturating the sample. The final discoloration effect is not as pronounced as in the previous trials, yet there is still an observable cleaning effect, even after multiple staining and washing processes. SEM photographs of these fibers after the initial staining only and after one staining, washing, and drying cycle are shown in Figure 4.14a and Figure 4.14b. These images show that the morphology of the cellulose fibers is unchanged and titania is still bound throughout the staining and washing processes. For reference, an SEM photograph of cellulose fibers (without TiO_2) after staining and exposure to halogen light is shown in Figure 4.14c.

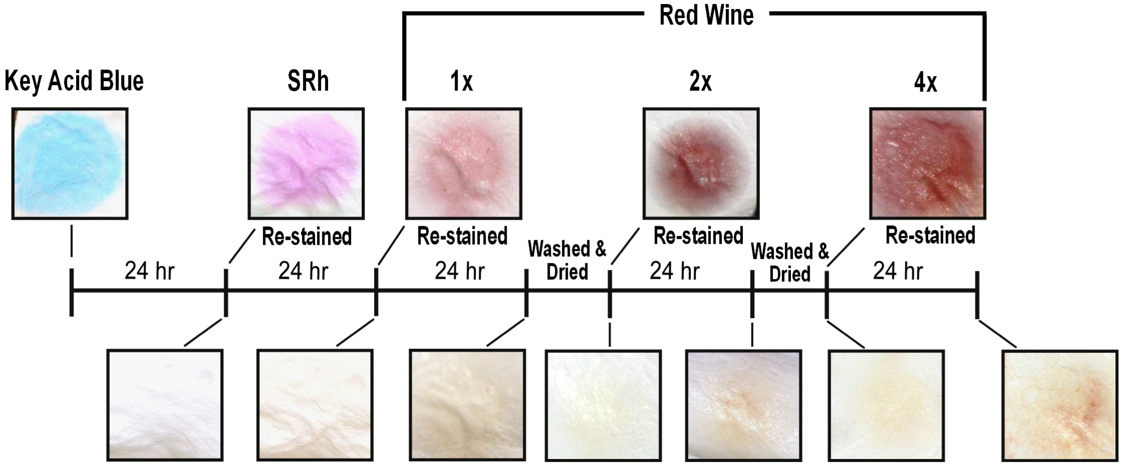

Figure 4.13. Photographs of non-woven mat formed by cellulose (core) - TiO_2 (sheath) fibers sequentially stained with dye solution (Keyacid Blue and sulforhodamine) and wine, halogen irradiated and washed and dried. From left to right: Keyacid Blue (0.1 wt%) solution; re-stained with sulforhodamine (0.01 wt%) solution; re-stained with red wine; washed, dried, and re-stained with twice the amount of red wine; then washed, dried, and completely saturated with four time the amount of red wine.

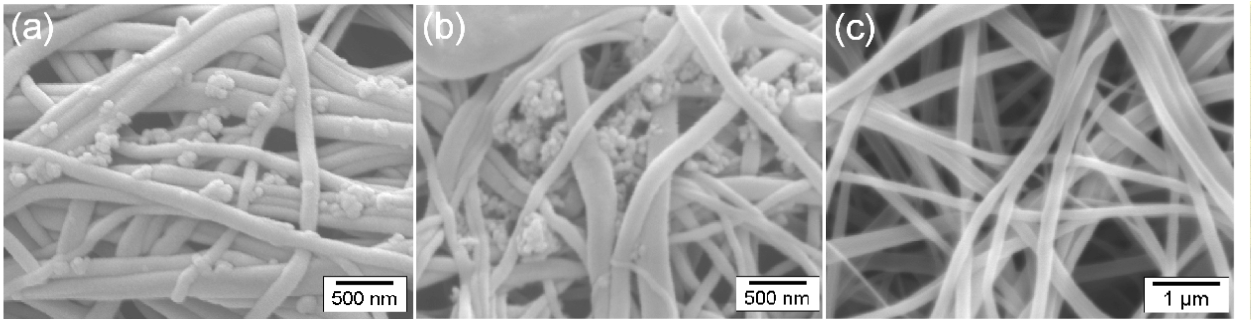

Figure 4.14. SEM microphotographs of (a) cellulose (core) – TiO_2 (sheath) fibers after being stained with a 0.1 wt% KeyAcid Blue solution and irradiated with ~13 mW/cm^2 halogen lighting for 24 hours, (b) cellulose (core) – TiO_2 (sheath) fibers after being stained with a 0.1 wt% KeyAcid Blue solution, irradiated with ~13 mW/cm^2 halogen lighting for 24 hours, and washed and dried according as described in the experimental section, and (c) cellulose fibers after being stained with a 0.1 wt% KeyAcid Blue solution and irradiated with ~13 mW/cm^2 halogen lighting for 24 hours.

4.4 Conclusions

Photocatalytic self-cleaning textile nanofibers have been created using coaxial electrospinning. Self cleaning activity is obtained in light typical of an indoor working environment. It was found that fibers created by coaxial electrospinning outperform those made by simple loading procedures and have the added benefit of requiring less post-electrospinning modification. It is worth noting that this study represents the lowest possible photocatalytic activity using this method. A more efficient photocatalyst (nitrogen or fluorine doped $TiO_{2,}$ and noble metal doped/bound TiO_2 for example) could be used to further accelerate the self cleaning performance. Different chemical functionalities can be employed to improve the adherence of the titania to the polymer, while testing in UV light would also increase the photocatalytic behavior seen in these experiments. In light of these considerations, it is concluded that the photocatalytic self cleaning textile fibers fabricated by coaxial electrospinning are comparable to non-electrospun photocatalytic self cleaning textile fibers seen in the literature that use better photocatalytic materials and sub-band gap wavelength light sources. This illustrates the important role played by the high surface to volume ratio of the material fabricated by coaxial electrospinning. The results of this study clearly show the versatility of coaxial electrospinning in general and more specifically indicate the promise of using this method for self-cleaning textiles applications.

---

[1] The bulk of this chapter appears in: N. M. Bedford, A. J. Steckl, *ACS Appl. Mater. Interfaces*, **2010**, *2*, 2448. Copyright the American Chemical Society, 2010.

[2] Molinari, R.; Mungari, M.; Drioli, E.; Di Paola, A.; Loddo, V.; Palmisano, L. Schiavello, M. *Catal. Today*, **2000**, *55*, 71.

[3] Vorontsov, A. V.; Chen, Y.-C.; Smirniotis, P. G. *J. Haz. Mater.* **2004**, *B113*, 89.

[4] Štengl, V.; Mařiková, M.; Bakardjieva, S.; Šubrt, J.; Opluštil, F.; Olšanska, M *J. Chem. Technol. Biotechnol.* **2005**, *18*, 754.

[5] Uddin, M. J.; Cesano, F.; Scarano, D.; Bonino, F.; Agostini, G.; Spoto, G.; Bordiga, S.; Zecchina, A. *J Photochem. Photobio. A: Chem.* **2008**, *199*, 64.

[6] Zhao, X.; Zhao, Q.; Yu, J.; Liu, B. *J. Non-Cryst. Solids* **2008**, *354*, 1424.

[7] Madaeni, S. S.; Ghaemi, N. *J. Membr. Sci.* **2007**, *303*, 221.

[8] Hoffmann, M. R.; Martin, S. T.; Choi, W.; Behnemann, D. W. *Chem. Rev.* **1995**, *95*, 69.

[9] Meilert, K. T.; Laub, D.; Kiwi, J. *J. Mol. Cat. A: Chem.* **2005**, *237*, 101.

[10] Textor, T.; Schröter, F.; Schollmeyer, E. *Macromol. Symp.* **2007**, *254*, 196.

[11] Daoud, W. A.; Leung, S. K.; Tung, W. S.; Xin, J. H.; Cheuk, K.; Qi, K. *Chem. Mater.* **2008**, *20*, 1242.

[12] Li, D.; Xia, Y. *Adv. Mater.* **2004**, *16 (14)*, 1151.

[13] Powell, H. M.; Boyce, S. T. *J. Biomed. Res., Part A* **2007**, *84A(4)*, 1078.

[14] Kenawy, E.-R.; Bowlin, G. L.; Mansfield, K.; Layman, J.; Simpson, D. G.; Sanders, E. H.; Wnek, G. E. *J. Control. Release* **2002**, *81*, 57.

[15] Liu, H.; Kameoka, J.; Czaplewski, D. A.; Craighead, H. G. *Nano Lett.* **2004**, *4(4)*, 671.

---

[16] Ma, M.; Gupta, M.; Li, Z.; Zhai, L.; Gleason, K. K.; Cohen, R. E.; Rubner, M. F.; Rutledge, G. C. *Adv. Mater.* **2007**, *19*, 255.
[17] Han, D.; Steckl, A. J. *Langmuir* **2009**, *25(16)*, 9454.
[18] Li, D.; Xia, Y. *Nano Lett.* **2003**, *3*, 555.
[19] Lee, J. A.; Krogman, K. C.; Ma, Minglin, Hill, R. M; Hammond, P. T.; Rutledge, G. C. *Adv Mater* **2009**, *21*, 1252.
[20] Yu, J. H.; Fridrikh, S. V.; Rutledge, G. C. *Adv. Mat.* **2004**, *16*, 1562.
[21] Li, D.; Xia, Y. *Nano Lett.* **2004**, *4(5)*, 933.
[22] Wang, M.; Jing, N.; Su, C. B.; Kameoka, J.; Chou, C.-K.; Hung, M.-C.; Chang, K.-A. *Appl. Phys. Lett.* **2006**, *88*, 033106.
[23] Han, X.-J.; Huang, Z.-M.; He, C.-C.; Liu, L.; Han, X.-J.; Wu, Q.-S. *Poly. Comp.* **2006**, *27*, 381.
[24] Heinze, T.; Liebert, T. *Prog. Polym. Sci.* **2001**, *26*, 1689.
[25] Hurum, D. C.; Agrios, A. G.; Gray, K. A.; Rajh, T.; Thurnauer, M. C. *J. Phys. Chem. B* **2003**, *107*, 4545.
[26] Hurum, D. C.; Gray, K. A.; Rajh, T.; Thurnauer, M. C. *J. Phys. Chem. B* **2005**, *109*, 977.
[27] Linkous, C. A.; Carter, G. J.; Locuson, D. B.; Ouellette, A. J.; Slattery, D. K.; Smitha, L. A. *Environ. Sci. Technol.* **2000**, *34*, 4754.
[28] Yu, J. C.; Yu, J.; Zhao, J. *Appl. Catal. B: Environ.* **2002**, *36*, 31.
[29] Cao, Y.; Yang, W.; Chen, Y.; Du, H.; Yue, P. *Appl. Sur. Sci.* **2004**, *236*, 223.
[30] Nagaveni, K.; Sivalingam, G.; Hegde, M. S.; Madras, G. *Appl. Catal. B: Environ.* **2004**, *48*, 83.
[31] Han, S.-O.; Youk, J.-H.; Min, K.-D.; Kang, Y.-O.; Park, W.-H. *Mat. Lett.* **2008**, *62*, 759.
[32] Sedaira, H.; Idriss, K. A.; Shafei Abdel-Aziz, M.; *Analyst* **1996**, *121*, 1079.
[33] Liu, H.; Hsieh, Y.-L. *J. Poly. Sci.: Part B: Poly. Phys.* **2002**, *40*, 2119.
[34] Son, W. K.; Youk, J. H.; Lee, T. S. ; Park, W. H. *J. Poly. Sci.: Part B: Poly. Phys.* **2004**, *42*, 5.
[35] Ma, Z.; Kotaki, M.; Ramakrishna, S. *J. Membr. Sci.* **2005**, *265*, 115.
[36] Zhao, H.; Kwak, J. H.; Wang, Y.; Franz, J. A.; White, J. M.; Holladay, J. E. *Carbohydr. Poly.* **2007,** *67*, 97.
[37] Nishiyama, Y.; Langan, P; Chanzy, H. *J. Amer. Chem. Soc.* **2002**, *124*, 9074.
[38] Stipanovic, A. J.; Sarko, A. *Polymer* **1978**, *19*, 3.
[39] Yuranova, T.; Laub, D.; Kiwi, J. *Catal. Today* **2007**, *122*, 109.
[40] Pelaez, M.; de la Cruz, A. A.; Stathatos, E.; Falaras, P.; Dionysiou, D. D. *Catal. Today* **2009,** *144*, 19.
[41] Gao, L.; Li, Q.; Song, Z.; Wang, J. *Sens. Actuators, B* **2000**, *71*, 179.
[42] Anpo, M.; Shima, T.; Kodama, S.; Kubokawa, Y. *J. Phys. Chem.* **1987**, *91*, 4305.
[43] Uzunova-Bujnova, M.; Todorovska, R.; Milanova, M.; Kralchevska, R.; Todorovsky, D. *Appl. Sur. Sci.* **2009**, *256*, 830.
[44] Lu, N.; Zhu, Z.; Zhao, X.; Tao, R.; Yang, X.; Gao, Z. *Biochem. Biophys. Res. Comm.* **2008**, *370*, 675.
[45] Chen, H.-W.; Su, S.-F.; Chien, C.-T.; Lin, W.-H.; Yu, S.-L.; Chou, C.-C.; Chen, J. J. W.; Yang, P.-C. *Fed. Amer. Soc. Exper. Bio. J.* **2006**, *20*, E1732.

Chapter 5:
Degradation of Potent Cyanobacteria Toxin Microcystin-LR Using Photocatalytic Cellulosic Electrospun Fibers[1]

5.1 Introduction

The need for low cost and efficient water treatment strategies is an ever increasing necessity given various potential sources of pollution attributed by industrial and natural sources.[2,3,4,5,6,7] Solar light driven photocatalysis with nanoparticles (such as titania, TiO_2) show tremendous promise as a simplistic and energy efficient technology for water purification and treatment.[8,9] Metal oxide photocatalysts readily generate hydroxyl and oxygen radicals upon exposure to light exceeding the band gap energy which degrade organic contaminants at the surface of the photocatalyst.[10] The titania nanoparticle variant P-25, in particular, exhibits the highest photocatalytic degradation of most organic contaminants of the commercially available metal oxide photocatalysts. This is due to longer charge-pair recombination lifetime and faster interfacial charge transfer rate.[10] Titania is also a comparatively inexpensive nanomaterial and is chemically stable, thus allowing it to be implemented in a wide variety of applications.[11,12,13,14,15]

The controlled immobilization of titania nanoparticles is a major obstacle in the successful use of these materials for water purification. Nanoscale titania is difficult to recover from free suspensions due to their intrinsically small sizes. Simple immobilization of the photocatalytic materials onto conventional substrates reduces the available surface area due to the interactions between the photocatalyst and substrate, limiting the rate of photocatalytic activity. Another issue with more common variants of titania is the inefficient absorption of a higher portion of the solar spectrum as these nanoparticles typically only absorb UV light. This only encompasses ~5% of the solar spectrum, which limits the amount of available sunlight that can be used for photocatalysis. To circumvent this issue, methodologies have been developed to extend the photon absorption properties of titania into the visible light region of the solar spectrum. These include dye sensitization[16,17,18] and doping with metal[19,20,21] and non-metal[22,23,24,25,26,27,28,29] elements. In water treatment applications, the use of dyes and metal dopants are not suitable for long term usage due to potential leaching of these materials from the photocatalyst which could potentially pose serious environmental and health issues. Doping with non-metal elements, such as carbon, nitrogen, fluorine, and sulfur serves as an environmentally benign alternative to increase the photon collecting efficiency of solar light driven photocatalyst in titania.

The immobilization of titania onto a membrane-like substrate would be of interest in water treatment applications as it could circumvent issues with using nanoparticle colloids and could still potentially have a high surface area to volume ratio. Furthermore, if the substrate was from a biodegradable, renewable and inexpensive source it would have added environmental and economical benefits. Cellulosic materials could serve as environmentally friendly substrate candidates for titania given the low cost, biodegradable/renewable and chemical robustness of these materials.[30] Cellulosic materials can be modified with the appropriate functionalities to have higher affinity for titania nanoparticles. Titania based photocatalytic textile-like materials could also be useful in other applications, such as protective/self cleaning clothing. Various groups have reported on the use of commercially available cellulosic textiles as substrates for titania.[31,32,33] An issue with these substrates is a relatively low surface area to volume ratio given the large fiber diameter used in commercial textiles. Non-woven three-dimensional meshes containing nano and sub-micron sized fibers can be easily obtained using the electrostatic fiber deposition process known as electrospinning.[34,35] Electrospun photocatalytic fibers have been previously made from titania sol/polymeric fibers (which after calcination yields pure titania),[36,37,38] electrospun polymeric fibers with layer-by-layer assembly of titania nanoparticles post electrospinning,[39,40] and by coaxial electrospinning.[41]

In this study, we report on the use of photocatalytic cellulosic non-woven nanofiber mats created by electrospinning for the degradation of the potent toxin microcystin-LR (MC-LR). MC-LR is one of the most commonly found cyanobacteria toxin generated by the more frequently occurring cyanobacteria algae blooms in various water sources across the world. The toxin natural proximity to drinking water sources, high water solubility, modest chemical stability, and high hepatoxicity have made water-bound MC-LR a serious health risk.[42,43] In an attempt to combat this problem, high surface area photocatalytic cellulosic fibers are generated by first electrospinning solutions of cellulose acetate (CA) into non-woven fiber meshes. The CA fibers are then converted to succinylated cellulose fibers through a series of simple reactions. The succinylated fibers are then loaded with titania from aqueous dispersions. Visible light activated titania are used to absorb a larger portion of the solar spectrum. The fiber mats surface area, titania surface coverage, and overall amount of titania in the photocatalytic electrospun fiber mats were found to have varying effects on the overall MC-LR degradation. These high surface area non-woven photocatalytic mats can effectively degrade MC-LR and show promise for photocatalytic drinking water treatment using solar light.

5.2 Experimental

5.2.1 Electrospinning

Solutions of cellulose acetate (CA, 39.8% acetyl content, M_w = 30,000 g/mol, purchased from Sigma-Aldrich) were made in 90% and 80% acetic acid (aq) at a concentration of 17 wt%.[44] Electrospinning was performed using a variable high voltage power supply (Glassman High Voltage) operating at 25 kV using a 5 × 5 cm Al collecting plate. CA solutions were fed to a spinneret (18 gauge blunt needle) at a flow rate of 0.5-0.6 mL/h using a syringe pump (Stoelting Co.). The spinneret to substrate distance was set to 11 cm for all experiments. All electrospinning experiments were performed under ambient conditions.

5.2.2 Fiber Processing

CA fibers were deacetylated to cellulose using 0.5 N KOH in ethanol, as described previously.[41] After 30 min, the cellulose fibers were removed from the ethanol solution and placed in 0.5 N HCl, followed by neutralization using 0.5 N KOH (aq). The fiber mats were washed in distilled water then dried under ambient conditions. The fibers were then placed in a 10% (w/v) succinic anhydride in dimethylformamide (DMF) solution for succinylation of the hydroxyl groups for two hours at 65 °C.[45] The succinylated cellulose fibers were then washed extensively with DMF to remove any un-reacted succinic anhydride and water to remove the DMF. The samples were then loaded with 1 wt% titania nanoparticle dispersions (sonicated with an ultrasonicator prior to loading) at acidic (pH=2), near-neutral (pH=6), and basic (pH= 10) pH for one hour at 75 °C. Acidic and basic solutions were made with HCl and KOH respectively. Titania dispersions consisted of P-25 (Degussa Aeroxide, purchased from Acros Organics), visible light activated Kronos vpl 7000 (purchased from Kronos Worldwide Inc., herein referred to only as Kronos), or nitrogen and fluorine doped titania (NF-TiO_2) made by sol gel techniques. NF-TiO_2 synthesis details can be found elsewhere.[23] Titania loaded fiber samples were sonicated in distilled water immediately after loading to remove any unbound titania.

5.2.3 Photocatalytic Degradation of MC-LR

For the photocatalytic evaluation of the electrospun fibers, double distilled water (pH 5.7) was spiked with an aliquot of MC-LR standard (Calbiochem) to achieve an initial concentration of 500 ± 20 μg/L of MC-LR. Each fiber mesh was weighted (~ 25 mg) and introduced to a glass reactor (I.D. 4.7 cm) that contains the previously spiked solution. A solar simulator (Newport Corporation) equipped with a 300 W Xe lamp, atmospheric attenuation (AM 1.5) and an infrared (IR) blocking filter was employed as light source. To obtain visible light irradiation only, an additional UV-block filter was included in the set up. The average light intensity reaching the reactor was 25 mW/cm^2 for the visible range as measured by a broadband radiant power meter (Newport Corporation). For the experiments under solar irradiation, the UV-block filter was removed and the average light intensity was 47.1 mW/cm^2. The reactor was sealed and cooled down with a fan to prevent evaporation during irradiation. Adsorption experiments were carried out under dark conditions to account for MC-LR absorption onto the photocatalytic fibers. Samples were obtained at established times and the concentration of MC-LR was determined by liquid chromatography according Antoniou et al.[46] A slight variation to the analytical method was done by introducing a C18 Discovery (Supelco) column with 2.1 μm particle size in order to reduce the flow rate to 0.2 ml/min and the injection volume to 20 μL.

5.2.4 Characterization

Fiber morphology was studied using a FEI/Phillips XL30 field-emission environmental scanning electron microscope (FE-ESEM). Chemical modification of cellulosic fibers was characterized using a Thermo Scientific Nicolet 6700 infrared spectroscopy (IR) spectrometer operating in transmission mode. BET analysis was performed with a Tristar 3000 (Micromeritics) porosimeter analyzer. The samples were vacuum freeze-dried (Labconco) for 24 h before analysis. X-ray photoelectron spectroscopy was performed using an M-Probe Surface Spectrometer (Surface Science) to determine the surface Ti/C ratio on the fiber samples. Ti-assay experiments were performed using a modified method from Sedaira et al.[47] Briefly, fiber samples were dissolved in 50 % (w/v) ammonium sulfate in concentrated sulfuric acid at elevated temperature. 100 µL of the digested material was then added to 20 mL of 0.3125 % (w/v) 5-chlorosalicylic acid, 0.125 M $NaClO_4$ in 50:50 water/ethanol, adjusted to pH = 3 (± 0.1) with concentrated ammonium hydroxide, and diluted to 25 mL with water. The quantification of Ti was performed by measuring the absorption of the solution at 355 nm. A standard solution of Ti was made by dissolving titania nanoparticles in 50 % (w/v) ammonium sulfate in concentrated sulfuric acid to obtain a calibration curve. In order to obtain the size distribution of titania particles, dynamic light scattering (DLS) was performed by ALV/CGS-3 using a 22 mW HeNe laser operating at 632.8 nm with a data acquisition time of 30 s.

5.3 Results and Discussion

To determine the effect of available surface area on photocatalytic performance, the electrospun fiber diameter was varied by changing the amount of acetic acid in the electrospinning solution as previously reported.[44] Fibers electrospun from a 17 wt% solutions of 80% and 90% acetic acid (aq) are shown in Fig. 5.1. Average fiber diameter, BET surface area, and pore volume for these samples are given in Table 5.1. Fibers electrospun from an 80% acetic acid solution have an average diameter of 230 ± 40 nm, while fibers electrospun from a 90% acetic acid solution have an average diameter of 320 ± 120 nm. This increase in fiber diameter and range of fiber diameter with increasing acetic acid is consistent with reported values.[44] Fibers electrospun from the 80% acetic acid solution showed a two-fold increase in BET surface area (4.84 ± 0.05 m^2/g vs. 2.94 ± 0.04 m^2/g) and pore volume (8.9×10^{-3} cm^3/g vs. 4.8×10^{-3} cm^3/g) compared to fibers electrospun from the 90% acetic acid solutions (Table 5.1). The CA electrospun fibers were then converted to cellulose, followed by a succinylation reaction to functionalize the cellulosic fibers with carboxylic acid groups (see experimental section). SEM images of fibers with each of the described functionalities are shown in Fig. 5.2 for fibers electrospun from 80% acetic acid (aq) solutions. Conversion of the CA fibers (Fig. 5.2a) to cellulose fibers (Fig. 5.2b) and then to succinylated cellulose fibers (Fig. 5.2c) resulted in a negligible change in overall fiber diameter and morphology of the fibers. An absence of morphological changes are also observed in fibers electrospun from 90% acetic acid (aq) solutions. Carboxylic acid functionality was used as these groups are known to bind titania better than acetyl and hydroxyl groups found in the CA and cellulose fibers.[31,45,48] To illustrate this, identical concentrations of P-25 were loaded onto cellulose fibers and succinylated cellulose fibers as shown in Fig. 5.3. There is a clear difference in the amount of titania loaded onto the carboxylic acid functionalized fibers (Fig. 5.3a) than the hydroxyl containing cellulosic fibers (Fig. 5.3b). IR spectroscopy was used to confirm the conversion of the cellulosic fiber materials (Fig. 5.4). The initial CA fibers have a strong peaks at 1740 cm^{-1} and 1230 cm^{-1} (Fig. 5.4, red line) that are associated with carbonyl stretching and ether bond stretching in the acetyl group, respectively.[49] Following deacetylation, the aforementioned peaks are absent from the spectrum (Fig. 5.4, dashed black line) along with the addition of the broad peak from 3600-3000 cm^{-1} corresponding to hydroxyl groups. Upon addition of succinic acid to the hydroxyl groups of the cellulose, the carbonyl peak reappears at 1715 cm^{-1}, while maintaining the broad peak for the hydroxyl group (Fig. 5.4, dashed blue line). The shift in lower absorption wavenumber from the carbonyl in the acetyl to carboxylic acid group is consistent with other reports.[50,51]

Table 5.1. Fiber diameter, BET surface area, and pore volume measurements from non-woven fiber mat samples electrospun from varying concentrations of acetic acid.

Fiber Sample	**Fiber Diameter (nm)**	**BET Surface Area** (m^2/g)	**Pore Volume** (cm^3/g)
80% acetic acid	230 ± 40	4.84 ± 0.05	0.0089
90% acetic acid	320 ± 120	2.94 ± 0.04	0.0048

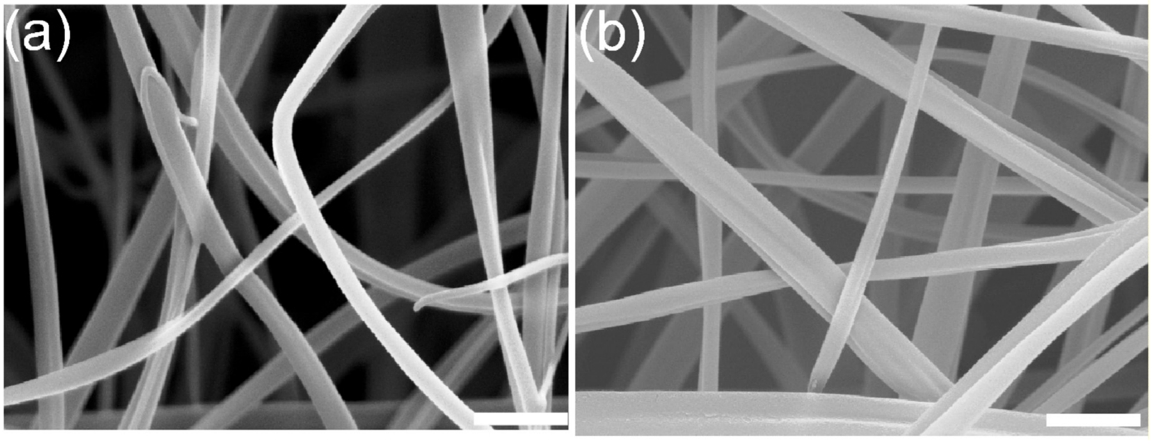

Figure 5.1. FE-SEM images of CA fibers electrospun from (a), 80% acetic acid solution (aq) and (b) 90% acetic acid solution (aq). Scales bars equal 1 μm.

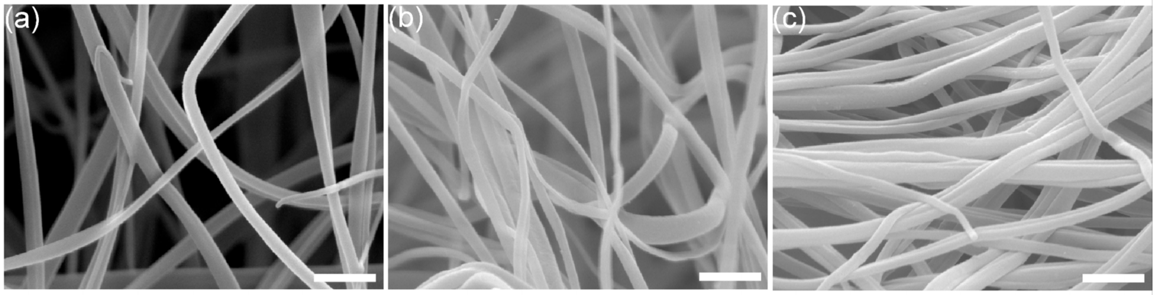

Figure 5.2. FE-SEM images of (a), CA nanofibers, (b) cellulose nanofibers, and (c) succinylated cellulose nanofibers. Initial CA nanofibers were electrospun from an 80% acetic acid solution (aq). All scales bars equal 1 μm.

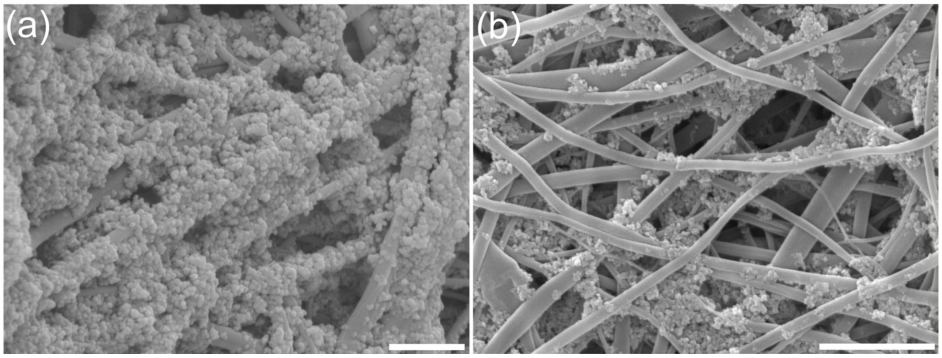

Figure 5.3. FE-SEM images of P-25 loaded fibers from a 17 wt% CA solution in 80% acetic acid (aq). (a) Succinylated cellulose fibers (scale bar equals 1 μm), and (b) cellulose fibers, (scale bar equals 2 μm).

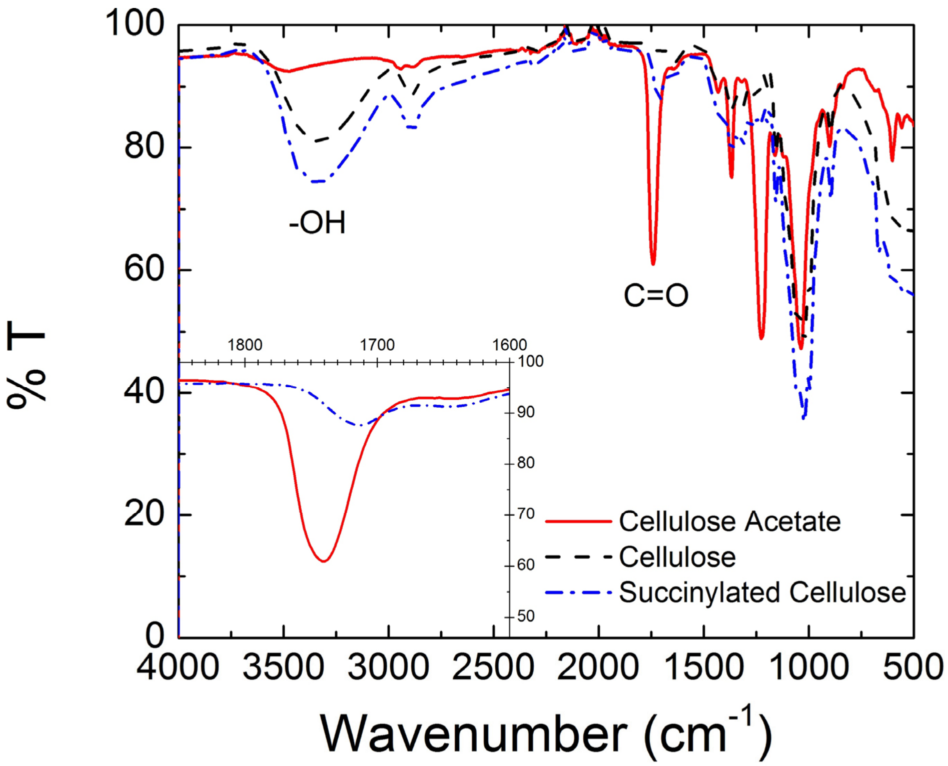

Figure 5.4. IR spectroscopy of CA fibers (red line), cellulose fibers (dashed black line), and succinylated cellulose fibers (dashed blue line).

The electrospun fibers were loaded with three different types of titania at pH=6 as described in the experimental section (Fig. 5.5). P-25 absorbs only UV light, while Kronos titania and NF-TiO_2 absorb light into the visible spectrum as well. As seen in Fig. 5.5, the fiber coverage of the loaded titania in the cellulosic fiber meshes is vastly different between the three types of titania. Kronos nanoparticles tend to form small sized clusters along the fiber (~100 nm) that are accompanied by larger spherical clusters on the 1-3 micron size scale that are typically imbedded in the pores of the fiber mat. The NF-doped titania also show smaller and larger clusters. However the larger sized clusters are much bigger than those seen in the Kronos loaded fiber samples. Furthermore, the overall amount of titania bound to the fibers appears to have decreased. Conversely, P-25 nanoparticles bind to the succinylated fibers more uniformly without the large aggregates seen in the visible light activated samples.

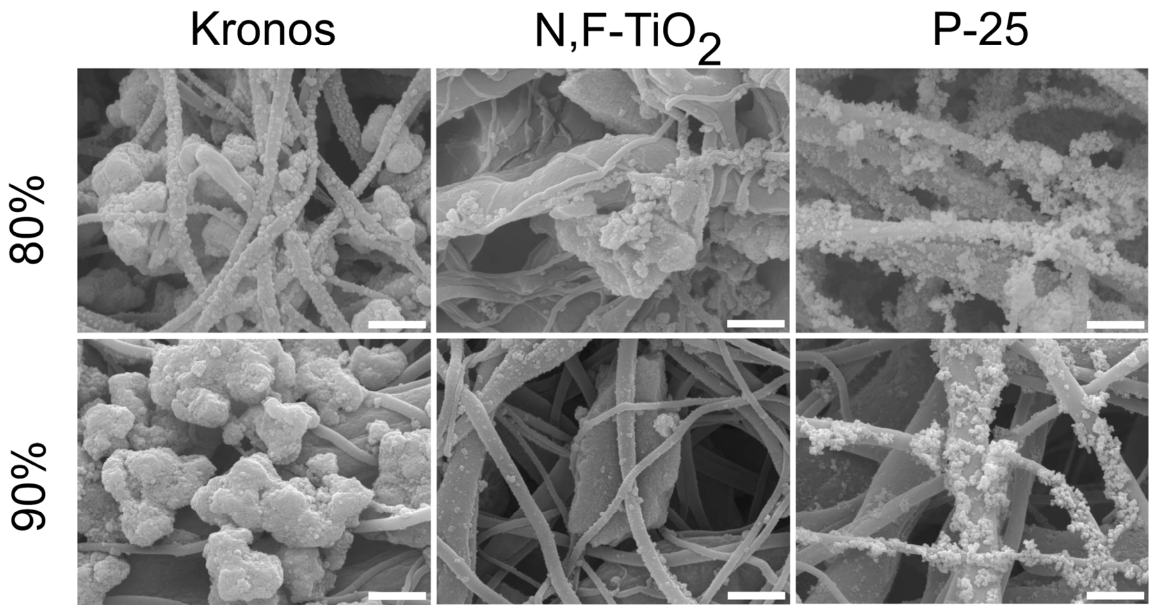

Figure 5.5. FE-SEM images of titania loaded succinylated cellulose nanofibers. Images from the top and bottom rows are fibers electrospun from 17 wt% CA solutions in 80% and 90% acetic acid (aq). Images from the left, middle, and right columns are samples loaded with Kronos, NF-TiO_2 and P-25 variants of titania respectively. All scale bars equal 1 µm.

To obtain more quantitative information on the overall amount of titania in the fiber mats as well as the extent of titania coverage on the surface of the fibers Ti assays and XPS experiments were performed, respectively (Table 5.2). An example XPS spectrum can be found in Fig 5.6. The ratio of surface titanium to carbon was calculated by the atomic percentages of each element obtained from XPS. It was found that P-25 covers the fibers more uniformly than the visible light activated titania nanoparticles, which confirms FE-SEM experiments. The NF-doped titania, in particular, has an order of magnitude lower surface Ti/C ratio than P-25 and Kronos, which is due to its comparatively lower dispersibility in water. This results in large aggregates seen throughout the fiber mat (Fig. 5.5). Fibers electrospun from an 80% acetic acid solution have the highest surface coverage of Kronos and NF-doped titania compared to fibers electrospun from 90% acetic acid solutions. The surface coverage of P-25 from the fiber samples is similar, which is due to the ability for P-25 to disperse better in aqueous media. In terms of the total amount of titania loaded into the fiber mats, the NF-TiO_2 generally have the higher titania percentages when compared to P-25 and Kronos. Although the surface coverage is poor, large aggregates of titania can be seen within the fibers (Fig. 5.5), which significantly attributes to the larger overall titania percentages found in these fibers. The fibers electrospun from 90% acetic acid tend to have larger overall amounts of titania, although surface coverage is generally poor.

Table 5.2. Surface Ti/C ratio (as determined using XPS) and percentage of titania in the fibers mats (as determined using a Ti-assay) for fibers electrospun at different acetic acid concentrations and loaded with different titania variants.

	P-25		**Kronos**		**NF-TiO_2**	
	80%	**90%**	**80%**	**90%**	**80%**	**90%**
Surface Ti/C ratio	0.5 ± 0.4	0.4 ± 0.1	0.30 ± 0.05	0.10 ± 0.05	0.03 ± 0.01	0.012 ± 0.006
TiO_2 %	10 ± 2 %	16 ± 10 %	6 ± 1 %	19 ± 5 %	20 ± 8 %	11 ± 2 %

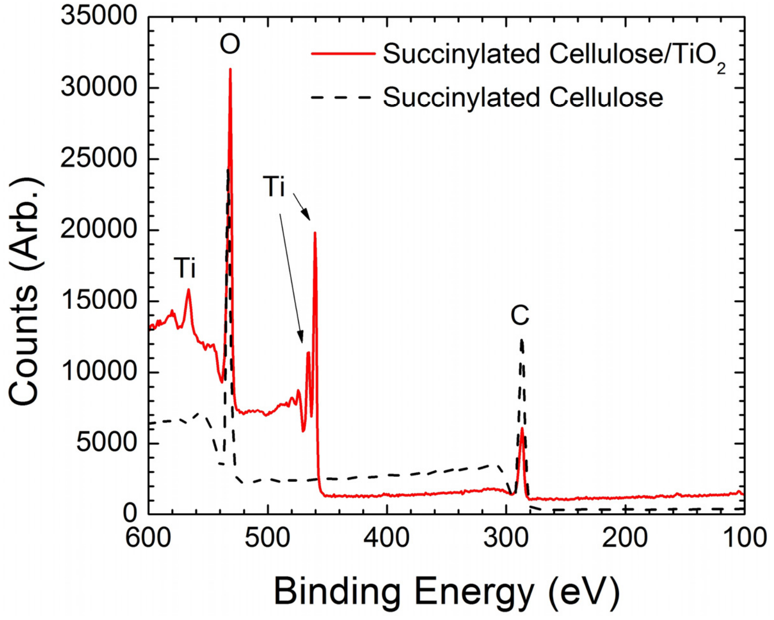

Figure 5.6. Example XPS spectra of succinylated cellulose (dashed black line) and P-25 loaded succinylated cellulose (red line).

The photocatalytic degradation of MC-LR by photocatalytic cellulosic fibers loaded with titania at pH=6 under visible and solar light are shown in Figs. 5.7 and 5.8, respectively. The extent of absorption percentage of MC-LR onto the fiber mats is shown in Table 5.3. It is worth noting that the absorption of MC-LR onto succinylated cellulose fibers without titania is much higher than fibers with titania. This is likely due to the high degree of hydrogen bonding between the succinic acid functionality on the fibers and the functional groups in the structure of MC-LR. With the addition of titania, the amount of absorbed MC-LR is reduced likely due to the decrease in free acid groups along the fiber. Under visible light irradiation (> 420 nm), only the Kronos and NF-doped titania show significant degradation of MC-LR as P-25 does not show any photocatalytic activity under these irradiation conditions. The Kronos loaded fiber samples degrade MC-LR faster than the NF doped titania loaded fibers, despite the NF-doped titania exhibiting comparable degradation rates of MC-LR as pristine nanoparticles in solution.[23] In fibers electrospun from 80% acetic acid, the Kronos loaded fibers degrade ~40% more MC-LR over a seven hour time period than the NF-TiO_2 loaded samples. This difference is reduced to ~10% in fiber electrospun from 90% acetic acid solutions. Under solar light conditions, all samples tested exhibit enhanced photocatalytic activity as the titania nanoparticles absorb more light which causes an increase the photocatalytic activity. Fiber samples loaded with P-25 and Kronos degrade MC-LR faster than samples loaded with NF-doped titania. Kronos and P-25 loaded samples completely degraded MC-LR for samples electrospun from 80% acetic acid after 7 h. Samples electrospun from 90% acetic acid solution exhibited comparatively lower MC-LR degradation due to the decreased surface coverage of titania and overall decrease in surface area.

Table 5.3. Adsorption of MC-LR onto various fiber mats as determined by taking aliquots of MC-LR from fiber samples under dark conditions.

Fiber Sample	NF-TiO_2 Loaded	Kronos Loaded	P25 Loaded	No TiO_2
80%	12.7 %	13.4%	14.3%	59.1%
90%	6.3%	6.8%	7.3%	28.7%

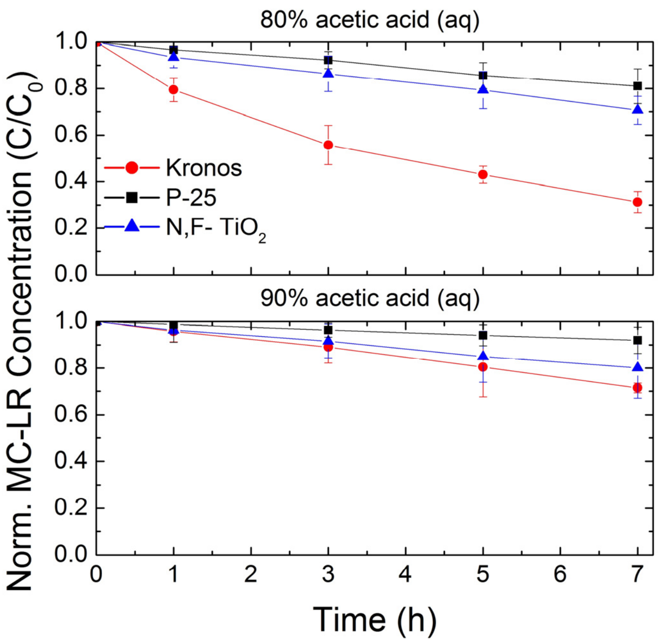

Figure 5.7. Photocatalytic degradation of MC-LR under visible light conditions (average light intensity of 25 mW/cm^2) for Kronos loaded fibers (red circles), NF-TiO$_2$ loaded fibers (blue triangles), and P-25 (black squares). The top and bottom graphs correspond to fiber electrospun from 17 wt% CA solutions in 80% and 90% acetic acid (aq).

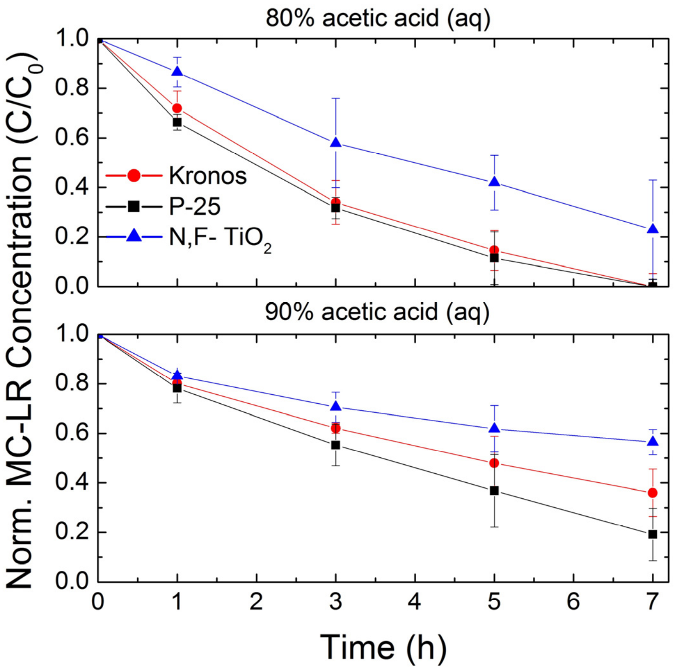

Figure 5.8. Photocatalytic degradation of MC-LR under solar light conditions (average light intensity of 47.1 mW/cm^2) for Kronos loaded fibers (red circles), NF-TiO$_2$ loaded fibers (blue triangles), and P-25 (black squares). The top and bottom graphs correspond to fiber electrospun from 17 wt% CA solutions in 80% and 90% acetic acid (aq).

While it is difficult to calculate accurate rate constants due to the heterogeneity of the samples (in terms of both chemical constituency and uniformity), certain metrics obtained from Table 5.2 can help explain MC-LR degradation behavior. Under visible light irradiation, the Kronos loaded samples degrade MC-LR faster than the NF-TiO_2 loaded fibers. This is due to the more uniform coverage of the Kronos on the fiber mats compared to the NF-TiO_2 as the total amount of titania in both samples have comparable amounts of titania. The importance of titania surface coverage is again displayed for samples tested under solar irradiation, as fibers loaded with P-25 and Kronos exhibit higher rates of MC-LR degradation compared to samples loaded with NF-TiO_2. In more general terms, fiber electrospun from 80% acetic acid degrade MC-LR faster than samples of fibers electrospun from 90% acetic acid. The surface coverage of titania on fibers electrospun from 80% acetic acid are generally higher than those fibers electrospun from 90% acetic acid despite that there is generally more titania in the 90% acetic acid samples (Table 5.2). This illustrates the importance of titania coverage over the total amount of titania, and to a lesser extent the surface area.

In order to increase the titania surface coverage in the photocatalytic electrospun fibers, titania aggregate sizes in the loading solution should be decreased. This was accomplished by loading titania onto the electrospun fibers at acidic and basic pH. This was performed as solutions used in the previously presented data have a pH of ~6. This is close to the isoelectric point (IEP) for the titania nanoparticles used in this study.[23,52] Aggregate size of titania at a pH of 2, 6, and 10 were determined using dynamic light scattering (DLS) and are given in Table 5.4. P-25 aggregate sizes are consistent with values reported in the literature,[52,53]with large aggregate size at pH = 6 (around P-25's IEP) and smaller aggregate sizes above and below the IEP. This decrease in aggregate size is due to electrostatic repulsion as titania becomes charged below (positive) and above (negative) the IEP. This trend is also exhibited in the NF-TiO_2 nanoparticles at larger sizes. Kronos nanoparticles exhibit a smaller average aggregate size at a pH of 2, while higher pH values lead to increased aggregate sizes.

Table 5.4. Average diameter of titania aggregates in aqueous solutions at different pH as determined by DLS.

Titania Type	P25			Kronos			NF-TiO$_2$		
pH	2	6	10	2	6	10	2	6	10
Diameter (nm)	127 ± 26	690 ± 97	400 ± 425	450 ± 20	1220 ± 40	1420 ± 30	930 ± 540	1400 ± 770	390 ± 90

Dispersions at varying pH values were then loaded onto succinylated cellulose fibers initially electrospun from an 80% acetic acid solution. Ti assays and XPS experiments were again used to determine the total amount of titania within the fibers mats and the TiO$_2$ surface coverage for samples loaded at different pH values (Table 5.5). The calculated Ti/C ratio from XPS data is higher at lower pH for all titania nanoparticles tested and decrease with increasing pH. The NF-TiO$_2$ loaded fibers exhibited the lowest Ti/C ratio of all the samples tested at pH = 6 and 10, but exhibit a larger comparative increase in Ti/C ratio at a loading pH = 2. The overall titania coverage in the electrospun fiber mats, as obtained by Ti assay experiments, was found to be comparable or slightly higher in samples loaded in acidic conditions compared to a pH = 6 (within standard deviation) and much smaller at higher pH. Titania aggregate size and surface coverage of titania on the fiber mats was observed using SEM (Fig. 5.9). The titania morphology within the fiber mats is consistent with data obtained from DLS and XPS.

Table 5.5. Surface Ti/C ratio (as determined using XPS) and percentage of titania in the fibers mats (as determined using a Ti-assay described in the experimental section) for fibers mats electrospun from 80% acetic acid loaded with titania at different pH values.

	P-25			**Kronos**			**NF-TiO$_2$**		
	pH=2	**pH=6**	**pH=10**	**pH=2**	**pH=6**	**pH=10**	**pH=2**	**pH=6**	**pH=10**
Surface Ti/C ratio	1.0 ± 0.2	0.5 ± 0.4	0.2 ± 0.1	0.5 ± 0.2	0.30 ± 0.05	0.21 ± 0.07	0.16 ± 0.07	0.03 ± 0.01	0.03 ± 0.01
TiO$_2$ %	15 ± 3%	10 ± 1%	7.8 ± 0.2%	13 ± 1%	6 ± 1%	9.5 ± 0.1	10 ± 0.7%	20 ± 8%	7.6 ± 0.4%

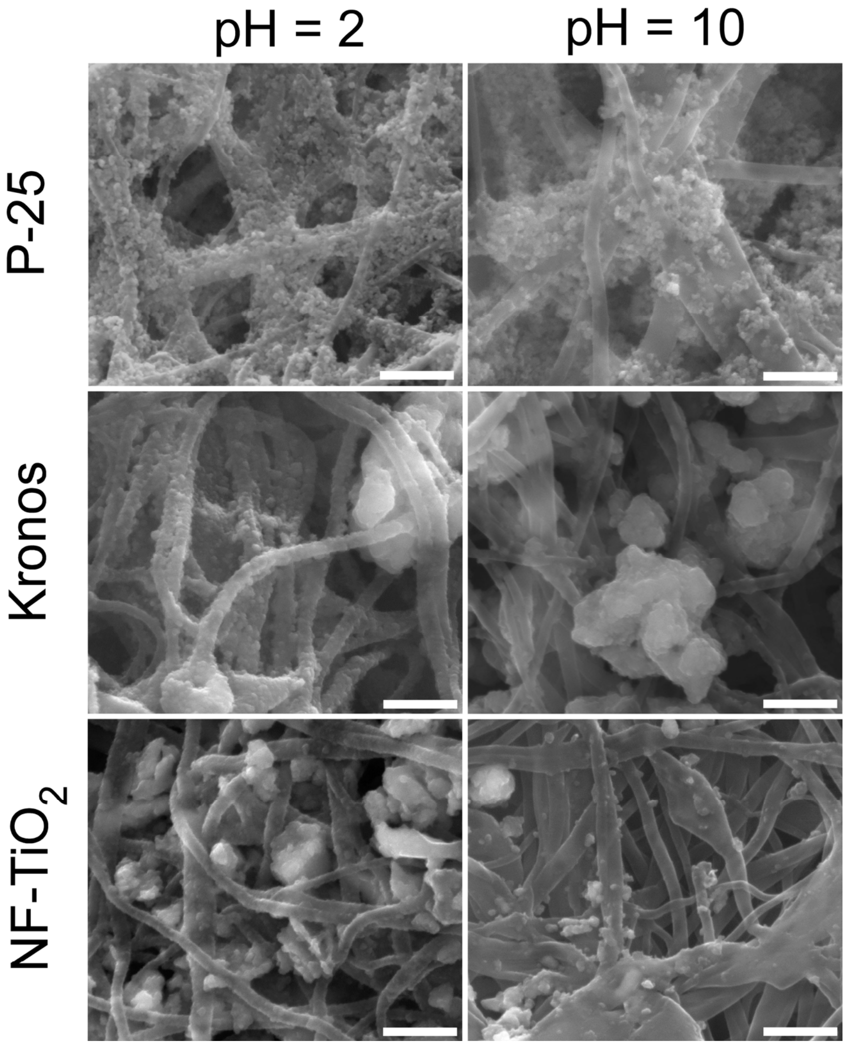

Figure 5.9. FE-SEM images of titania loaded succinylated cellulose nanofibers at different pH. Images from the top, middle and bottom rows are fibers electrospun from loaded with P-25, Kronos, and NF-TiO$_2$. Images from the left and right columns are samples loaded at pH =2 and 10 respectively. All scale bars equal 1 μm.

At basic pH, succinic acid functionality in the electrospun fibers likely displays a carboxylate anion while the dispersed titania nanoparticles bear a negative charge.[52] At pH=10 the electrospun fibers and the titania electrostatically repel each other and a decrease in the total amount and surface coverage of titania are observed. At a pH close to the IEP of titania (pH ~ 6) titania starts to agglomerate into larger aggregates due to the absence of electrostatic repulsion. The carboxylate anions are likely still present at this pH, as the isoelectric point for various succinylated biomacromolecules are in the pH = 4-

7 range.[54,55] At lower pH, titania becomes positively charged and forms smaller aggregates while the succinic acid functionality is neutral. At acidic pH more titania will bind to the fibers as protonated carboxylic acids have been found to have a higher affinity for titania than un-protonated carboxylic acids.[56,57] This enhanced binding coupled with the smaller aggregates sizes lead to increased surface coverage of titania in electrospun fiber mats loaded at acidic pH.

Electrospun fibers mats loaded at different pH were tested for MC-LR degradation. Solar light degradation is shown in Fig. 5.10 and visible light degradation shown in Fig 5.11. Under solar light, Kronos and P-25 titania degrade MC-LR completely for fibers loaded with titania at pH = 2 and 6. For fiber mats loaded at basic pH, P-25 based fiber mats still show sufficient MC-LR degradation, while Kronos loaded fiber mats at a basic loading pH show a reduced amount of MC-LR degradation compared to acidic and near neutral loading pH. Data from Table 5.4 and Fig. 5.9 show at pH=10, P-25 aggregates are ~1/3 the size of Kronos. As such, more titania surface is exposed and thus a large amount of MC-LR is degraded. For electrospun fiber mats loaded with NF-TiO_2 nanoparticles, there are notable different in MC-LR degradation vs. loading pH. At a loading pH of 2, the NF-TiO_2 loaded fibers exhibit the highest MC-LR degradation. This can be attributed to the relatively higher titania surface coverage compared to samples loaded at pH of 6 and 10 (Table 5.5). This effectively illustrates the potential importance of loading pH of titania onto fibrous substrates. Electrospun fiber mats loaded at pH = 6 show improved MC-LR degradation properties compared to fiber mats loaded at pH = 10 despite the identical titania surface coverage. However, there is a two-fold increase in the total amount of titania in the fibers loaded at pH=6 vs. pH=10. Visible light degradation of MC-LR exhibits similar trends with samples loaded at varying pH yet with an overall decrease in the amount of MC-LR degradation (with the exception of samples loaded with P-25, which is inactive at this wavelength range).

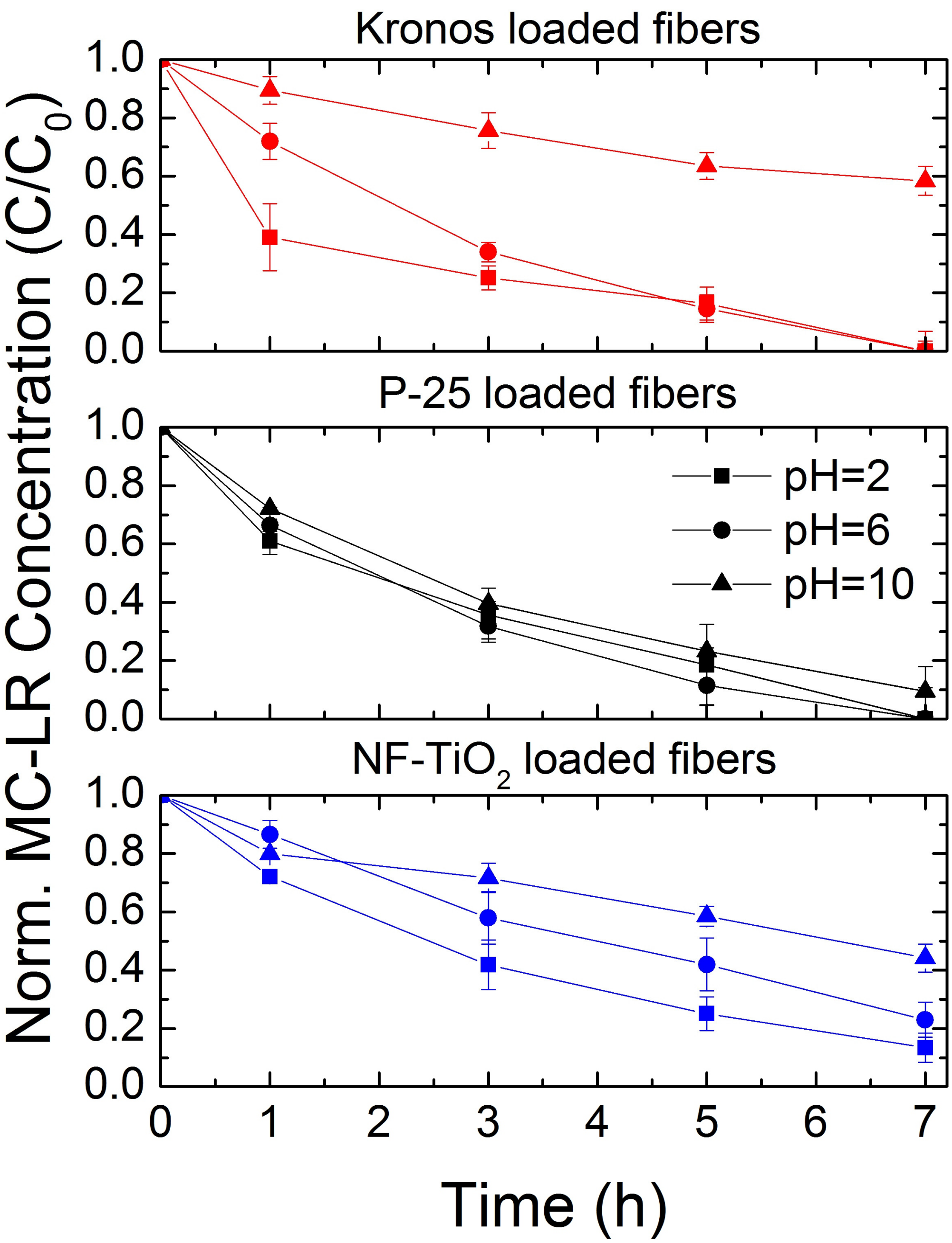

Figure 5.10. Photocatalytic degradation of MC-LR under solar light conditions (average light intensity of 47.1 mW/cm^2) for Kronos loaded fibers (red lines), NF-TiO$_2$ loaded fibers (blue lines), and P-25 (black lines) at pH = 2 (squares), pH=6 (circles), and pH= 10 (triangles).

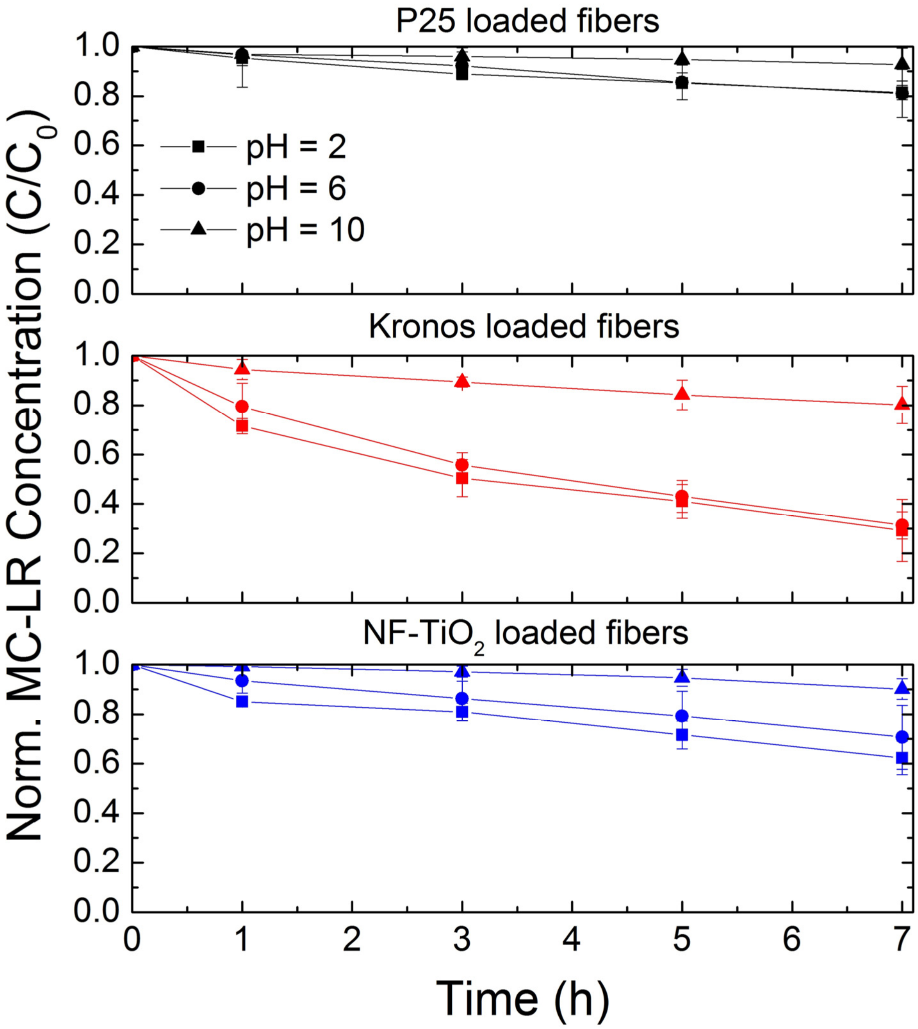

Figure 5.11. Photocatalytic degradation of MC-LR under visible light conditions (average light intensity of 25 mW/cm^2) for P-25 (black lines), Kronos loaded fibers (red lines), and NF-TiO$_2$ loaded fibers (blue lines) at pH = 2 (squares), pH=6 (circles), and pH= 10 (triangles).

Selected degradation rates of MC-LR by photocatalytic electrospun fibers with comparisons to nanoparticle slurries[23] and films[58] are shown in Table 5.6. Degradation rates of the photocatalytic fiber meshes are comparable to those of pure titania films and slurries. This is a remarkable result, considering the surface TiO$_2$ to fiber mesh ratio is 1:1 at best, the overall amount of titania is typically below 20% (see Tables 5.2 and 5.5) and the surface area of the electrospun fibers prior to loading with titania is ~3 orders of magnitude lower the surface area of the electrospun fibers prior to titania loading.[23,58] The likely reason for the high degradation rates is due to MC-LR absorption onto the surface of the cellulosic material, as can be seen in Table 5.3. The succinic acid moiety in the electrospun fibers and MC-LR inevitably form hydrogen bonds due to the number of available hydrogen bond donors can acceptors on the fibers and in the toxin. In regions between the fibers and titania, MC-LR is affixed to the fibers, which can allow for the material to be more easy degraded when compared to diffusion related MC-LR-titania interactions.

Table 5.6. MC-LR degradation rates for electrospun fibers and photocatalytic experiments from the literature.

MC-LR Degradation (µM*min^{-1}*g^{-1})	Visible Light Activated				UV Light Activated	
	Kronos		$NF-TiO_2$		eSpun Fibers[e]	Film[f]
	eSpun Fibers[a]	Nanoparticle Slurry[b]	eSpun Fibers[c]	Nanoparticle Slurry[d]		
	0.84	1.24	0.21	0.96	0.78	1.55

[a] Degradation calculated from Kronos nanoparticles loaded onto electrospun fibers from 80% acetic acid (aq) at pH = 6 under three hours of visible light exposure.
[b] Degradation calculated from reference 23, under two hours of visible light exposure.
[c] Degradation calculated from $NF-TiO_2$ nanoparticles loaded onto electrospun fibers from 80% acetic acid (aq) at pH = 2 under three hours of visible light exposure.
[d] Degradation calculated from reference 23, under two hours of visible light exposure. Nanoparticle had a surface area of 141.6 m^2/g.
[e] Degradation calculated from P-25 nanoparticles loaded onto electrospun fibers from 80% acetic acid (aq) at pH = 6 under three hours of solar light exposure.
[f] Degradation calculated from reference 58, under three hours of UV light exposure. Film made from a standard TiO_2 sol with the addition of Tween-80, with a resulting surface area of 147 m^2/g.

5.4 Conclusions

Photocatalytic cellulosic fibers were made from electrospun fibers by a simple titania surface loading technique using UV-light activated titania nanoparticles and visible light activated titania. These photocatalytically viable fiber meshes were tested for potential usage as decontamination membranes for the degradation of MC-LR, a potent cyanobacteria toxin. Surface area, titania surface coverage, and overall titania concentration for the electrospun fibers were correlated to MC-LR degradation. The surface coverage of titania and surface area are more critical to effective MC-LR degradation than the overall amount of titania in the fibers. These photocatalytic non-woven high surface area membranes could be advantageously employed for drinking water and waste water treatment applications using solar light as a renewable source of energy.

---

[1] The bulk of this chapter appears in : N. M. Bedford, M. Pelaez, C. Han, D. D. Dionysiou, A. J. Steckl, *Ener. Environ. Sci.* **2011**, *submitted*.
[2] E. B. Kujawinski, M.C. Kido Soule, D. L. Valentine, A. K. Boysen, K. Longnecker, M. C. Redmond, *Environ. Sci Technol.* **2011**, *45*, 1298.
[3] A. Wise, K. O'Brien, T. Woodruff, *Environ. Sci. Technol.* **2011**, *45*, 51.
[4] E. Hoh, L. Zhu, R. A. Hites, *Environ. Sci Technol.* **2006**, *40*, 1184.
[5] M. Wekler, C. Steinberg, *Environ. Sci. Technol.* **2000**, *34*, 3415.
[6] S. Di Pasqule, M. Paniconi, B. Aurichhio, L. Orefice, A. C. Schultz, D. De Medici, *J. Virol. Methods* **2010**, *165*, 57.
[7] K. Lemarchand, P. Lebaron, *FEMS Microbiol. Lett.* **2003**, *218*, 203.
[8] D. Bahnemann, *Sol. Engery* **2004**, *77*, 445.
[9] H. Choi, E. Stathatos, D. D. Dionysiou, *Desalination* **2007**, *202*, 199.
[10] M. R. Hoffmann, S. T. Martin, W. Choi, D. W. Behnemann, *Chem. Rev.* **1995**, *95*, 69.
[11] J. H. Braun, A. Baidins, R. E. Marganski, *Prog. Org. Coat.* **1992**, *20*, 105.
[12] M. Grätzel, *Acc. Chem. Res.* **2009**, *42*, 1788.
[13] U. I. Gaya, A. H. Abdullah, *J. Photochem. Photobio. C Photochem. Rev.* **2008**, *9*, 1.
[14] K. Schilling, B. Bradford, D. Castelli, E. Dufour, J. F. Nash, W. Pape, S. Schulte, I. Tooley, J. van den Bosch, F. Schellauf, *Photochem. Photobio. Sci.***2010**, *9*, 495.
[15] X. Zhao, Q. Zhao, J. Yu, B. Liu, *J. Non-Cryst. Solids* **2008**, *354*, 1424.
[16] T. Rajh, L. X. Chen, K. Lukas, T. Liu, M. C. Thurnauer, D. M. Tiede, *J. Phys. Chem. B* **2002**, *106*, 10543.
[17] Z. Wang, W. Mao, H. Chen, F. Zhang, X. Fan, G. Qian, *Catal. Comm.* **2006**, *7*, 518.
[18] W. Kim, T. Tachikawa, T. Majima, C. Li, H.-J. Kim, W. Choi, *Ener. Environ. Sci.* **2010**, *3*, 1789.
[19] W. Choi, A. Termin, M. R. Hoffman, *J. Phys. Chem.* **1994**, *98*, 13669.
[20] S. Klosek, D. Raftery, *J. Phys. Chem. B* **2001**, *105*, 2815.
[21] S. Kim, S.-J. Hwang, W. Choi, *J. Phys, Chem. B* **2005**, *109*, 24260.
[22] J. Zhang, Y. Wu, M. Xing, S. A. K. Leghari, S. Sajjad, *Ener. Environ. Sci.* **2010**, *3*, 715.
[23] M. Pelaez, A. A. de la Cruz, E. Stathatos, P. Falaras, D. D. Dionysiou, *Catal. Today*, **2009**, *144*, 19.
[24] R. Bacca, J. Kiwi, T. Ohno, P. Albers, V. Nadtochenko, *J. Phys. Chem. B* **2005**, *109*, 5994.
[25] X. Chen, Y. Lou, A. C. S. Samia, C. Burde, J. L. Gole, *Adv. Funct. Mater.* **2005**, *15*, 41.
[26] S. In, A. H. Kean, A. Orlov, M. S. Tikhov, R. M. Lambert, *Ener. Environ. Sci.* **2009**, *2*, 1277.
[27] Y. Choi, T. Umebayashi, M. Yoshikawa, *J. Mater. Sci.* **2004**, *39*, 1837.
[28] C. Han, M. Pelaez, V. Likodimos, A. G. Kontos, P. Falaras, K. O'Shea, D. D. Dionysiou, *Appl. Catal. B Environ.* **2011**, *107*, 77.
[29] N. Shi, X. Li, T. Fan, H. Zhou, J. Ding, D. Zhang, H. Zhu, *Ener. Environ. Sci*, **2011**, *4*, 172.
[30] D. Klemm, B. Heublein, H.-P. Fink, A. Bohn, *Angew. Chem. Int. Ed.* **2005**, *44*, 3358.
[31] T. Yuranova, D. Laub, J. Kiwi, *Catal. Today* **2007**, *122*, 109.
[32] M. J. Uddin, F. Cesano, D. Scarano, F. Bonino, G. Agostini, G. Spoto, S. Bordiga, A. Zecchina, *J. Photochem. Photobio. A: Chem.* **2008**, *199*, 64.
[33] N. Abidi, L. Cabrales, E. Hequet, *ACS Appl. Mater. Interfaces* **2009**, *1*, 2141.
[34] S. Agarwal, A. Greiner, J. H. Wendorff, *Adv. Funct. Mater.* **2009**, *19*, 2863.
[35] D. Li, Y. Xia, *Adv. Funct.* **2004**, *16*, 1151.
[36] D. Li, Y. Xia, *Nano Lett.* **2003**, *3*, 555.
[37] A. K. Alves, F. A. Berutti, F. J. Clemens, T. Graule, C. P. Bergmann, *Mater. Res. Bull.* **2009**, *44*, 312.
[38] S. Zhan, D. Chen, X. Jiao, C. Tao, *J. Phys. Chem. B* **2006**, *110*, 11199.
[39] J. A. Lee, K. C. Krogman, M. Ma, R. M. Hill, P. T. Hammond, G. C. Rutledge, *Adv. Mater.* **2009**, *21*, 1252.
[40] J. A. Lee, Y. S. Nam, G. C. Rutledge, P. T. Hammond, *Adv. Funct. Mater.* **2010**, *20*, 2424.
[41] N. M. Bedford, A. J. Steckl, *ACS Appl. Mater. Interfaces*, **2010**, *2*, 2448.

---

[42] M. G. Antoniou, A. A. de la Cruz, D. D. Dionysiou, *J. Environ. Eng.*, **2005**, *51*, 1239.

[43] I. R. Falconer, *Environ. Toxicol.*, **1999**, *14*, 5.

[44] S. O. Han, J. H. Youk, K. D. Min, Y. O. Kang, W. H. Park, *Mater. Lett.*, **2008**, *62*, 759.

[45] W. A. Daoud, S. K. Leung, W. S. Tung, J. H. Xin, K. Cheuk, K. Qi, *Chem. Mater.* **2008**, *20*, 1242.

[46] M.G. Antoniou, J.A. Shoemaker, A. A. de la Cruz, D. D. Dionysiou, *Toxicon*, **2008**, 51, 1103.

[47] H. Sedaira, K. A. Idriss, M. S. Abdel-Aziz, *Analyst*, **1996**, *121*, 1079.

[48] K. T. Meilert, D. Laub, J. Kiwi, *J. Mol. Cat. A: Chem.* **2005**, *237*, 101.

[49] S. Köhler, T. Liebert, M. Schöbitz, J. Schaller, F. Meister, W. Günther, T. Heinze, *Macrmol. Rapid Comm.* **2007**, *28*, 2311.

[50] Z. Ma, M. Kotaki, S. Ramakrishna, *J. Membr. Sci.* **2005**, *265*, 115.

[51] C. F. Liu, R. C. Sun, A. P. Zhang, J. L. Ren, X. A. Wang, M. H. Qing, Z. N. Chao, W. Luo, *Carbohy. Res.* **2007**, *342*, 919.

[52] K. Suttiponparnit, J. Jiang, M. Sahu, S. Suvachittanont, T. Charinpanitkul, P. Biswas, *Nanoscale Res. Lett.* **2001**, *6*, 27.

[53] J. Jiang, G. Oberdörster, P. Biswas, *J. Nanopart. Res.* **2009**, *11*, 77.

[54] E. K-W. Toh, H.-Y. Chen, Y.-L. Lo, S.-J. Huang, L.-F. Wang, *Nanomed. Nanotechnol. Biol. Med.* **2001**, *7*, 174.

[55] H. N. Ong, B. Arumugam, S. Tayyab, *J. Biochem.* **2009**, *146*, 895.

[56] Y.-X. Weng, L. Li, Y. Liu, L. Wang, G.-Z. Yang, *J. Phys. Chem. B* **2003**, *107*, 4356.

[57] A. Vittadini, A. Selloni, F. P. Rotzinger, M. Grätzel, *J. Phys. Chem. B* **2000**, *104*, 1300.

[58] M. G. Antoniou, P. A. Nicolaou, J. A. Shoemaker, A. A. de la Cruz, D. D. Dionysiou, *Appl. Catal. B. Environ.* **2009**, *91*, 165.

Chapter 6:
Recommendations for Future Research

6.1 Introduction

The bulk of this thesis has presented and analyzed the use of electrospun fibers in energy, electronic, and environmental applications. In this last chapter, recommendations for future research will be presented and will serve as next natural steps for two of the projects in this thesis.

6.2 Moving Away from P3HT

Although the P3HT:PCBM system is by far and away the most studied BHJ-OPV system,[1] other materials systems exist that display higher PCEs.[2,3,4,5,6,7,8,9] The PCE for P3HT:PCBM is found to be heavily reliant on the extent of phase separation and polymer/fullerene morphology. Yet with most of the "newer" polymer donor materials, the control over morphology is never examined. In Chapter 2, the use of electrospun fiber of P3HT:PCBM lead to increases in J_{sc}, FF, and PCE. The coaxial electrospinning process employed could be extended to other BHJ-OPV systems as the process is dominated by the outer sheath material. Here it is suggested to look at other BHJ-OPV donor/acceptor systems, particularly those reported to exhibit better efficiency that P3HT:PCBM. Unfortunately, most other electron donor polymers reported in the literature are not commercially available and this proposed direction of research would require either extensive polymer synthesis and characterization or collaboration with an appropriate laboratory.

6.3 Better Titania Binding with Peptides

The use of electrospun cellulosic fibers for titania immobilization has been demonstrated in this thesis (Chapter 4 and 5) for water decontamination purposes.

Electrospun cellulosic fibers serve as environmentally friendly substrates candidates for titania given these materials' low cost, biodegradable/renewable and chemical robustness.[10] In an effort to improve the titania coverage along these fibers, a cysteine modified titania binding peptide Ti-1 (RKKRTKNPTHKLGGGC) [11] can be coupled to the carboxylic acids in the electrospun fibers through a series of standard coupling reactions. The Ti-1 peptide should bind titania better than a signal carboxylic acid moieties because of the rigorous panning require to discover this peptide sequence. For example, there are no such reports of peptides found through display techniques that have a majority of aspartic acid (i.e. carboxylic acid functionalized) residues. Therefore, the high affinity of Ti-1 should improve titania coverage in the fibers compared to succinic acid functionalized fibers. In order to confirm the surface chemistry on the fibers, x-ray photoelectron spectroscopy will be used by measuring nitrogen and sulfur elements found in the crosslinking agents and peptides as the cellulosic materials do not contain these elements. Peptide binding should be achievable using visible light activated titania as well as the level of doping is typically on the single atomic percentages.

---

[1] M. T. Dang, L. Hirsch, G. Wantz, *Adv. Mater.***2011,** *23,* 3597.
[2] H.-Y. Chen, J. Hou, S. Zhang, Y. Liang, G. Yang, Y. Yang, L. Yu, G. Li, *Nat. Photonics* **2009**, *3*, 649-653.
[3] S. H. Park, A. Roy, S. Beaupré, S. Cho, N. Coates, J. S. Moon, D. Moses, M. Leclerc, K. Lee, A. J. Heeger, *Nat. Photonics* **2009**, *3*, 297-303.
[4] Y. Lang, D. Feng, Y. Wu, S.-T. Tsai, G. Li, C. Ray, L. Yu, *J. Amer. Chem. Soc.* **2009**, *131*, 7792-7799.
[5] Y. Lang, Y. Wu, D. Feng, S.-T. Tsai, H.-J. Son, G. Li, L. Yu, *J. Amer. Chem. Soc.* **2009,** *131*, 56-57.
[6] C.-P. Chen, S.-H. Chan, T.-C. Chao, C. Ting, B.-T. Ko, *J. Amer. Chem. Soc.* **2008**, *130*, 12828-12833.
[7] N. Blouin, A. Michaud, M. Leclerc, *Adv. Mater.* **2007**, *19*, 2295-2300.
[8] J. Chen, Y. Cao, *Acc. Chem. Res.* **2009**, *42*, 1709-1718.
[9] O. Inganäs, F. Zhang, M. R. Andersson, *Acc. Chem. Res.* **2009**, *42*, 1731-1739.
[10] D. Klemm et al., *Angew. Chem. Int. Ed.* **2005**, *44*, 3358.
[11] M. B. Dickerson et al., *Chem. Mater.* **2008**, *20*, 1578.